DEFORMATION STUDIES OF POLYMERS AND POLYMER/CLAY NANOCOMPOSITES

A Dissertation
Presented to
The Academic Faculty

by

Bilge Gurun

In Partial Fulfillment
of the Requirements for the Degree
Doctor of Philosophy in the
School of Polymer, Textile and Fiber Engineering

Georgia Institute of Technology
December 2010

DEFORMATION STUDIES OF POLYMERS AND POLYMER/CLAY NANOCOMPOSITES

Approved by:

Dr. David G. Bucknall, Co-advisor
School of Polymer, Textile and Fiber Engineering
Georgia Institute of Technology

Dr. Yonathan S. Thio, Co-advisor
School of Polymer, Textile and Fiber Engineering
Georgia Institute of Technology

Dr. Haskell W. Beckham
School of Polymer, Textile and Fiber Engineering
Georgia Institute of Technology

Dr. Donggang Yao
School of Polymer, Textile and Fiber Engineering
Georgia Institute of Technology

Dr. Kenneth Gall
School of Materials Science and Engineering
Georgia Institute of Technology

Date Approved: October 22, 2010

To the everlasting love and support of

my Dad, my Mom, my Sister and

my Husband…

ACKNOWLEDGEMENTS

First and foremost, I would like to express my gratitude to my advisors, David Bucknall and Yonathan Thio who gave me an opportunity to work with them as their student at GaTech. They supervised me with their knowledge and experience throughout my time at GaTech, especially when things were tough. It was a great experience to work with them.

I would like to thank - Drs. Beckham, Yao and Gall for serving on my dissertation committee and for their most valued inputs. I would like to thank all of them once more for allowing me to use their lab space and equipment whenever I needed. I am grateful to - Drs. Kumar and Minus for training me and letting me use their X-ray facility. I am also thankful to Dr. Jacob for his support and understanding throughout my time at PTFE. There is a number my colleagues who have helped me during this time. I would like to thank Ram, Yong Ho, Sehoon, Sarang and Mihir for their helpful discussions on classes and qualifier as well as different aspects of my project.

I would like to thank the administrative staff – Dan, Mike, Angie, Hope and Linda for helping me take care of other things so I could do my research more effectively.

Many thanks to my former and current group members Katie, Hannah, Xi and Deepali for making life easier and more bearable for me. I especially want to thank Katie and Rebecca for staying up all night with me during the synchrotron experiments and working as if it is their own. I appreciate their hard work, stamina and support. I have to thank many other friends, whom I do not have enough space here to list their names, for their unconditional and supporting friendship.

I would like to thank my dad, mom and sister for their constant encouragement through phone calls. I would like to thank them for believing in me and trusting all my decisions.

Last but not least, I would like to thank my beloved husband, Gokce Gurun. He is my love and my life. I feel special for having him in my life and I am grateful to him for being on my side and supporting me all the time. Without him believing in me, I could not have come to finish this work.

TABLE OF CONTENTS

LIST OF TABLES

LIST OF FIGURES

SUMMARY

Polymer clay nanocomposites have been a popular area of materials research since they were first introduced in the 1990s. The inclusion of clays into many different host polymers has been shown to improve the properties of matrix polymers in a number of ways including increased mechanical strength, thermal stability and improved barrier properties while keeping the composite light weight and transparent. Although there is a great deal of published work on the preparation and property measurements of polymer clay nanocomposites, there is no model to design a nanocomposite with a given set of properties for a specific end-use. While it is important to know the structure property relationships of materials, the understanding of how nanocomposites reach their final forms and properties is equally important. A thorough understanding of processing effects on the final structure of polymer clay nanocomposites is still missing. With this perspective, this thesis addresses building structure-processing relationships of polymer clay nanocomposites by analyzing multiaxial deformation behavior using *in-situ* x-ray scattering techniques.

This thesis can be divided into two distinct parts. The first part concerns the design of the *in-situ* multiaxial deformation device (IMDD) used to create the deformation conditions that polymers go through during processing such as blow molding and thermoforming. The device was designed to overcome several concerns with *in situ* measurement by maintaining constant sample to detector distance, minimizing the material between the incident beam and the detectors, as well as exposing the same point on the sample throughout deformation. A new design to create biaxial

deformation, termed *in-situ* biaxial deformation device (IBDD), is also introduced in this part of the thesis.. In addition, a new heating unit, attached to IBDD, is designed for higher temperature studies, up to 150℃, to imitate industrial processing conditions more closely.

The second part of the thesis addresses the effect of strain, strain rate, and temperature as well as the amount of clay on the polymer morphology evolution during multiaxial deformation.. Two different polymer/clay systems were studied: poly(ethylene)/clay and poly(propylene)/clay. It was observed that the morphological evolution of polyethylene and polypropylene is affected by the existence of clay platelets as well as the deformation temperature and the strain rate. Martensitic transformation of orthorhombic polyethylene crystals into monoclinic crystal form was observed under strain but is hindered in the presence of clay nanoplatelets. The morphology evolution of poly(propylene) crystal structure during multiaxial deformation was more subtle where the most stable α-crystalline form went through strain induced melting. This was more noticeable in the nanocomposites with clays up to 5 wt%.

It was also noted that the thickness of the interlamellar amorphous region increased with increasing strain at room temperature due to the elongation of the amorphous chains. The increase in the amorphous layer thickness is slightly higher for the poly(ethylene)/clay nanocomposites compared to neat poly(ethylene) while the increase in the lamellar long spacing is slightly higher for the neat poly(propylene) compared to poly(propylene)/clay nanocomposites. The rate of change in the characteristic repeat distance in both poly(ethylene) and poly(propylene) systems is

higher at faster strain rates, at room temperature, where it remained constant during higher temperature deformations.

Time dependent recovery after deformation studies have shown that poly(ethylene)/clay system reverts back to its initial configuration. The recovery in the amorphous chains was however observed to take longer in the clay added poly(ethylene)s. Crystalline relaxation was observed to happen almost instantly in the poly(ethylene)/clay system. On the other hand, amorphous chains in the poly(propylene)/clay system did not revert back to the initial configuration in the period of time that the recovery observations were performed while the crystalline configuration recovered back almost fully in the given time.

LIST OF SYMBOLS AND ABBREVIATIONS

1D	One dimensional
2D	Two dimensional
3D	Three dimensional
AFM	Atomic Force Microscopy
AgBe	Silver behenete
Al	Aluminum
APS	Advanced Photon Source
a.u.	Arbitrary units
Ca^+	Calcium ion
Cd	Cadmium
CTE	Coefficient of thermal expansion
d	Bragg long spacing
d_{ac}	Lamellar thickness
d_a	Amorphous layer thickness
d_c	Crystalline layer thickness
DSC	Differential scanning calorimetry
DLS	Diamond Light Source
E	Elastic modulus
f	Herman's orientation function
ESRF	European Synchrotron Radiation Facility
FWHM	Full width at half maximum

G'	Storage modulus
G"	Loss modulus
h	Hexagonal
HDPE	High density poly(ethylene)
HDT	Heat distortion temperature
I	Total integrated intensity of both crystalline and amorphous parts
I_c	Integrated intensities of the crystalline peaks
IBDD	In-situ Biaxial Deformation Device
IMDD	In-situ Multiaxial Deformation Device
K^+	Potassium ion
K(z)	Correlation function
l_i	Initial grid separation length
l_f	Final grid separation length
LDPE	Low density poly(ethylene)
m	Monoclinic
MAXS	Medium angle X-ray scattering
MMT	Montmorillonite
n	Shear thinning exponent
Na^+	Sodium ion
NIST	National Institute of Standards and Technology
NMR	Nuclear magnetic resonance
o	Orthorhombic
Pd	Palladium

PEO	Poly(ethylene oxide)
PE	Poly(ethylene)
PENC	Poly(ethylene)/clay nanocomposite
PLS	Polymer layered silicate nanocomposite
PMC	Polymer matrix composite
PNC	Polymer-matrix nanocomposite
PP	Poly(propylene)
PPNC	Poly(propylene)/clay nanocomposite
PVA	Poly(vinyl alcohol)
q	Scattering vector
Q	Scattering invariant
QUB	Queens University Belfast
rpm	Revolutions per minute
ROI	Region of interest
RT	Room temperature
s	Inverse scattering vector
SR	Synchrotron radiation
SAXS	Small angle x-ray scattering
Si	Silicon
SiO_2	Silicon oxide
SURF	Synchrotron Ultraviolet Radiation Facility
UV	Ultra-violet
T_c	Crystallization temperature

T_g	Glass transition temperature
T_m	Melting temperature
TEM	Transmission electron microscopy
TGA	Thermo-gravimetric analysis
WAXS	Wide angle x-ray scattering
x_1	Spatial point 1
x_2	Spatial point 2
X_c	WAXS crystallinity index
XRD	X-ray diffraction
α_c	Linear crystallinity
β_{hk}	Full width at half maximum
γ	Shear strain
ε_b	Breaking strain
ε_y	Yield strain
η^*	Complex viscosity
θ	Half the scattering angle
λ	Wavelength
λ	Extension/stretch ratio, strain
λ^*	Yield stretch ratio
λ^{**}	Breaking stretch ratio
μ	Attenuation coefficient
ρ	Density
$\rho(x_1)$	Local electron density profile at spatial point x_1

$\rho(x_2)$	Local electron density profile at spatial point x_2
$<\rho^2>_{av}$	Average square of the electron density fluctuations
φ	Azimuthal angle
φ_c	Volume fraction
ω	Oscillation frequency
∞	Infinity

CHAPTER I

INTRODUCTION

1.1 Motivation

A recent development in polymer science has been in the area of polymer-matrix layered silicate composites (PLS) [1, 2]. The clay inclusions in these composites can produce dramatic improvements in base material performance for small loadings (typically, less than $5 wt\%$) due to their extremely high aspect ratios and surface-to-volume ratios [3-7]. One of the first demonstrations of PLS was by researchers at Toyota who showed that the addition of $5 wt\%$ silicate nanoclay to nylon-6 resulted in 40% increase in tensile strength, 68% increase in flexural modulus and a significant increase in heat distortion temperature (HDT) as well as barrier properties [1, 2]. Subsequently, other researchers have reported substantial property improvements with a tremendous variety of host polymers, as summarized in recent review articles [8, 9]. Today, nanocomposites are beginning to find commercial applications from food packaging to automotive components with companies such as Nanocor offering a wide range of products [10].

Despite the extensive research on PNCs, there is no generic quantitative model that allows one to design a nanocomposite with any given set of properties. What is missing is the understanding of how morphology develops during processing and how it changes during deformation. The types of final morphologies formed from a large variety of starting recipes are known, as well as their effects on the nanocomposite properties.

However, relatively little is known about how the morphologies reach their characteristic forms during processing, or how these structures subsequently behave under large-scale deformation to fracture.

On the other hand, the high intensity and good collimation of modern synchrotron radiation (SR) beamlines have made it feasible to study the often rapid structural evolution of polymeric materials, when deformed or annealed, through time resolved small angle X-ray scattering (SAXS) and wide angle x-ray scattering (WAXS) measurements. The combination of SAXS and WAXS allows a wide range of sizes to be probed (approximately 0.1–500 nm). When measured simultaneously, these two scattering techniques provide a very detailed understanding of the structure of the polymers. The immense flux of SR sources provides the opportunity to measure the dynamics of the structure on time scales of 1 s (or often considerably less) per frame. Consequently, the use of combined SAXS/WAXS measurements has been shown to be a very powerful method for *in situ* measurements of polymer structures during processing operations such as stretching and fiber formation (spinning). These studies have elucidated the influence of several parameters on the polymer morphological evolution such as strain, strain rate, and temperature [11-16]. A number of studies published in the literature have concentrated on *in situ* uniaxial deformation of various polymers using SR measurements [12, 14, 16-24]. Observations of uniaxial deformation are very important to understand the fundamental behavior in a controlled system; however, under many processing conditions, the deformation is much more complex. In many industrial processing conditions such as thermo-forming and blow molding, polymer films are deformed multiaxially rather than uniaxially. In order to predict the properties of

polymers prior to and after processing, it is essential to study the morphological development of the polymers under multiaxial deformation. Moreover, it is essential to observe these changes occurring to the polymer morphology *in situ*, thereby eliminating the effects of internal relaxations. Therefore the objective of this project is to understand how morphology of polymers and PLS nanocomposites develops and changes during multiaxial deformation, so that nanocomposites can be designed with specific properties and the properties can be estimated prior to processing.

1.2 Scope of Dissertation

Chapter II introduces and reviews the relevant literature. In Chapter III, design of the *in-situ* multiaxial deformation device is discussed and the experimental set-up is explained which was summarized in a recent publication [25]. In Chapter IV, materials along with the various characterization techniques utilized, such as differential scanning calorimetry, multiaxial deformation, melt rheology and x-ray scattering are discussed. Results from different PLS systems including PE and PP are discussed in Chapter V and VI, respectively. In Chapter VII, the conclusions from this thesis are presented and possible lines of extension for future research are outlined.

CHAPTER II

LITERATURE REVIEW

2.1 Polymer composites in general

Composites make up a very broad an important class of engineering materials. By definition a composite is any material made of more than one component. Humans have been creating composite materials to build stronger and lighter objects for thousands of years. The majority of composite materials use two constituents: a binder or matrix and reinforcement or filler. The reinforcement is stronger and stiffer, forming a sort of backbone, while the matrix keeps the reinforcement in a set place. The binder also protects the reinforcement, which may be brittle or breakable, as in the case of the long glass fibers used in conjunction with plastics to make fiberglass. Generally, composite materials have excellent compressibility combined with good tensile strength, making them versatile in a wide range of situations. Engineers who design or use composite materials now generally classify them into one of four categories: (i) Polymer matrix composites (PMC), (ii) Metal matrix composites and (iii) Ceramic matrix composites. Among them polymer matrix composites form 90 % of the composites' market [26]. They are very popular due to their low cost and simple fabrication methods.

In general production and use of PMCs, reinforcement component of the composite are fibers. Glass, carbon and Kevlar are the most commonly used fiber types which are used as reinforcements to the polymers. In addition to fibers modern PMCs also include different shape of reinforcements such as woven and nonwoven structures

[27, 28], membranes [29] and particles [30, 31]. Properties of PMCs are determined by properties of the filler, orientation of the filler, concentration of the filler and properties of the matrix. Properties of PMCs are estimated by the rule of mixtures. Because the fillers and the polymers possess different functionalities, the range of applications is diverse. Some examples to these applications are secondary load-bearing aerospace structures, boat bodies, canoes, kayaks, automotive parts, radio controlled vehicles, sport goods (golf clubs, skis, tennis racquets, fishing rods), bullet-proof vests and other armor parts, brake and clutch linings [32].

High demand on strong yet light weight structural materials, easy and cost-effective processing, applicability of the end-product to wide range of end-use areas have required the development of new PMCs where smaller, micro and nano, sized fillers came into the picture. The concept consists of deriving a hybrid from two generically different constituent materials such as organic and inorganic at a molecular level dispersion. Hybridization of such organic and inorganic is an important and evolutionary route for the growth of strong polymer–filler interface. Practically, it offers economic advantage and is versatile in nature. This can be explained by the low volume (1–5%) of nanofillers required to achieve properties which are comparable or even better than those achieved by conventional loadings (15–40%) of traditional fillers. The lower loadings facilitate processing and reduce component weight. Also, this means higher strength to weight ratio which is very useful in case of automobile and aerospace industries [33].

2.2 Polymer nanocomposites in general

During the past few decades, polymeric nanocomposites (PNCs) have been an area for extensive industrial and academic research and it still keeps growing. PNCs are a new class of materials with a great deal of future promise for potential applications as high-performance materials and they are very promising type of materials to become the most versatile industrial advanced materials. It is possible to control the fundamental properties of materials, such as their melting temperature, magnetic properties, charge capacity, and even their color, without changing the materials' chemical compositions, by reducing the size of the materials from macro to nano. Such potential improvements and changes in the material properties are promising to lead to new, high-performance products and technologies that were not possible before. For decades macrocomposites such as filled polymers have been produced where the length scale of the polymer fillers is in micrometers. On the other hand the polymer coils are rougly 40 nm in diameter, and the nanoparticles are on the same order of magnitude as the polymer; as a result, molecular interaction between the polymer and the nanoparticles will give polymer nanocomposites unusual material properties that conventional polymers do not possess [34].

With a broadly accepted definition, nanocomposites are materials reinforced with particles which have at least one dimension with a size of 100 nm or less. The most attractive advantage of these materials is the amount filler loading. Compared to conventional composites with microscopic reinforcements with loadings of ~< 40 vol.%, a few volume percent of nanoparticle reinforcement provides similar material properties [35]. In addition, nanoscopic reinforcements do not significantly alter the matrix's

processability and do not add extra weight to the composite system as well as not changing the clarity [36].

Uniform dispersion of these nano-sized fillers produces very large interfacial area per volume between the nanoparticle and the matrix polymer. The huge internal interfacial area and the nanoscopic dimensions between nanoparticles fundamentally differentiate PNCs from traditional filled PMCs. These materials' characteristics simply imply that the overall performance of PNCs cannot be understood by simple scaling rules that apply to traditional polymer composites such as the rule of mixtures. Thus, new combinations of properties derived from the nanoscale structure of PNCs are necessary.

Many examples can be found in the literature demonstrating substantial improvements in physical and mechanical properties. However, the value of PNC technology is not based only on mechanical enhancements of the neat resin. Rather, its value comes from providing value-added properties not present in the neat resin, without sacrificing the inherent processibility and mechanical properties of the neat resin. Traditionally, the preparation of a blend or composite with multifunctionality requires a trade-off between desired performance, mechanical properties, cost, and processibility.

Today's nanocomposites research is mostly focused on three types of nano reinforcements (see Figure 1): three dimensional (3D) particles such as metals, organic and inorganic spheres with nanoscale diameter, two dimensional (2D) layered materials such as graphite and silicates with nanoscale thicknesses and one dimensional (1D) fiber type materials such as nanofibers and nanotubes with nanoscale diameters. The most readily cited examples of 1D nanocomposites are systems based on carbon nanotubes. Carbon nanotubes have many interesting properties, including exceptionally high

mechanical strength and remarkably versatile electronic properties. These properties make them ideal reinforcing fibers in nanocomposites. However, carbon nanotubes do not easily disperse in polymers, making filler dispersion a major issue. Nanotubes create aggregates to form bundles that are very difficult to separate. In addition, such bundles or ropes are often heavily entangled with one another. Under shear conditions, these ropes can be untangled, but dispersion at the single-tube level is difficult to achieve, since the attractive forces are very strong, and the percolation threshold is low. Similarly, high concentrations of carbon nanotubes are difficult to work with due to viscosity issues [37].

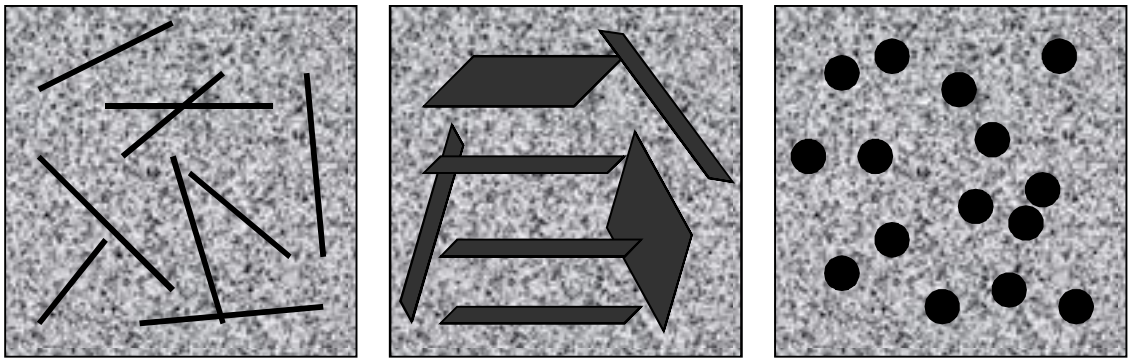

Figure 1. *Schematic of nanofillers with different volumetric shapes.*

The main characteristics of the PNCs which bring the superior properties to the matrix are their low percolation threshold (~0.1-2 vol%), particle-particle correlation arising at low volume fractions ($\phi_c < 0.001$), large number density of particles per particle volume (10^6-10^8 particles/μm^3), extensive interfacial area per volume of particles (10^3-10^4 m^2/ml), short distances between particles (10-50nm at ϕ~1 - 8 vol%); and

comparable size scales among the rigid nanoparticle inclusion, distance between particles, and the relaxation volume of polymer chains [36].

Nanocomposites produced using layered clay minerals and carbon nanotubes are the ones that have commercial significance. Among these two types, layered silicate platelet reinforced polymer nanocomposites are the most dominant commercial nanocomposites accounting for nearly 70% of the volume used with the biggest share formed by automotive and packaging applications [38]. Table 1 lists some of the supplier companies and the types of commercial nanocomposites they produce.

Table 1. *Partial Listing of Nanocomposite Suppliers*

Suppler & Tradename	**Matrix Resin**	**Nanofiller**	**Target Market**
Bayer AG (Durethan LPDU)	Nylon 6	Organo-clay	Barrier films
Clariant	PP	Organo-clay	Packaging
Creavova (Vestamid)	Nylon 12	Nano-tubes	Electrically conductive
GE Plastics (Noryl GTX)	PPO/Nylon	Nano-tubes	Automotive painted parts
Honeywell (Aegis)	Nylon6/Barrier Nylon	Organo-clay	Multi-purpose
Nanocor (Imperm)	Nylon 6/ PP	Organoclay	Multi-purpose/Molding
Polymeric Supply	Unsaturated polyester	Organo-clay	Marine, Transportation
RTP	Nylon 6, PP	Organo-clay	Multi-purpose, electrically conductive
Showa Denko (Systemer)	Nylon 6 Acetal	Clay, mica Clay, mica	Flame retardant Multi-purpose
Ube (Ecobesta)	Nylon 6, 12 Nylon 6, 66	Organo-clay Organ-clay	Multi-purpose Auto fuel systems
Unitika	Nylon 6	Organo-clay	Multi-purpose
Kabelwerk Eupen of Belgium	EVA	Organo-clay	Wire & cable
Hyperion	PETG, PBT, PPS, PC, PP	Nano-tubes	Automotive painted parts

Sources: Bins & Associates, Sheyboygan, Wis.
http://www.plasticstechnology.com/articles/199906fa4.html
http://zeus.plmsc.psu.edu/~manias/news/plastics_tech_oct_2001.pdf

2.3 Structure and Properties of Layered Silicates

Clay minerals used for polymer nanocomposites are usually classified in three groups: type 2:1, type1:1, and layered silicic acids. Type 2:1 clays consist of nanometer thick layers of aluminum octahedron sheets sandwiched between two silicon tetrahedron sheets. Van der Waals forces exist between the layers. Isomorphic substitution of Al with Mg, Fe, Li in the octahedron sheets and/or Si with Al in tetrahedron sheets gives the structure a negative charge. Montmorillonite (MMT), hectonite, saponite and laponite are some examples to 2:1 type. On the other hand type 1:1 clays consisting of alternating layers of one aluminum octahedron and one silicon tetrahedron sheet. The layers have no charge due to the absence of isomeric substitution in either of the sheets. Kaolinite and halloysite are some examples of this type. Finally, layered silicic acids consist of silicon tetrahedron sheets with different layer thicknesses. These clays have high purity and their structural properties are complementary to type 2:1 clays. Kanemite, makatite and octasilicate are some examples to layered silicic acids [39]. In Table 2 a list of commercially available clay minerals and their details can be found. Among the listed nanoclays, montmorillonite is the most commonly used.

Table 2. *Clay minerals used for polymer nanocomposites (Reproduced from [39])*

Type of clay	Formula	Origin	Substitution	Layer charge
2:1 type				
MMT	$M_x(Al_{2-x}Mg_x)Si_4O_{10}(OH)_2 \cdot nH_2O$	Nature (N)	Octahedral	Negative
Hectorite	$M_x(Mg_{3-x}Li_x)Si_4O_{10}(OH)_2 \cdot nH_2O$	N	Octahedral	Negative
Saponite	$M_xMg_3(Si_{4-x}Al_x)O_{10}(OH)_2 \cdot nH_2O$	N	Tetrahedral	Negative
Fluorohectorite	$M_x(Mg_{3-x}Li_x)Si_4O_{10}F_2 \cdot nH_2O$	Synthetic (S)	Octahedral	Negative
Laponite	$M_x(Mg_{3-x}Li_x)Si_4O_{10}(OH)_2 \cdot nH_2O$	S	Octahedral	Negative
Fluoromica (Somasif)	$NaMg_{2.5}Si_4O_{10}F_2$	S	Octahedral	Negative
1:1 type				
Kaolinite	$Al_2Si_2O_5(OH)_4$	N	--	Neutral
Halloysite	$Al_2Si_2O_5(OH)_4 \cdot 2H_2O$	N	--	Neutral
Layered silicic acid				
Kanemite	$Na_2Si_4O_9 \cdot 5H_2O$	N/S	Tetrahedral	Negative
Makatite	$NaHSi_2O_5 \cdot 7H_2O$	N/S	Tetrahedral	Negative
Octosilicate	$Na_2Si_8O_{17} \cdot 9H_2O$	S	Tetrahedral	Negative
Magadiite	$Na_2Si_{14}O_{29} \cdot 10H_2O$	N/S	Tetrahedral	Negative
Kenyaite	$Na_2Si_{20}O_4 \cdot 10H_2O$	S	Tetrahedral	Negative

Silica is the dominant constituent of the montmorillonite clays, with alumina being essential. The chemical structure of montmorillonite clays is illustrated in Figure 2 showing its sheet structure consisting of layers containing the tetrahedral silicate layer and the octahedral alumina layer. The tetrahedral silicate layer consists of SiO_4 groups linked together to form a hexagonal network of the repeating units of composition Si_4O_{10}. The alumina layer consists of two sheets of closely packed oxygens or hydroxyls, between which octahedrally coordinated aluminum atoms are imbedded in such a position that they are equidistant from six oxygens or hydroxyls. The two tetrahedral layers sandwich the octahedral layer, sharing their apex oxygens with the latter. These three layers form one clay sheet that has a thickness of 0.96 nm. The chemical formula of the montmorillonite clay is $Na_{1/3}$ $(Al_{5/3}Mg_{1/3})Si_4O_{10}(OH)_2$. In its natural state Na^+ cation resides on the MMT clay surface.

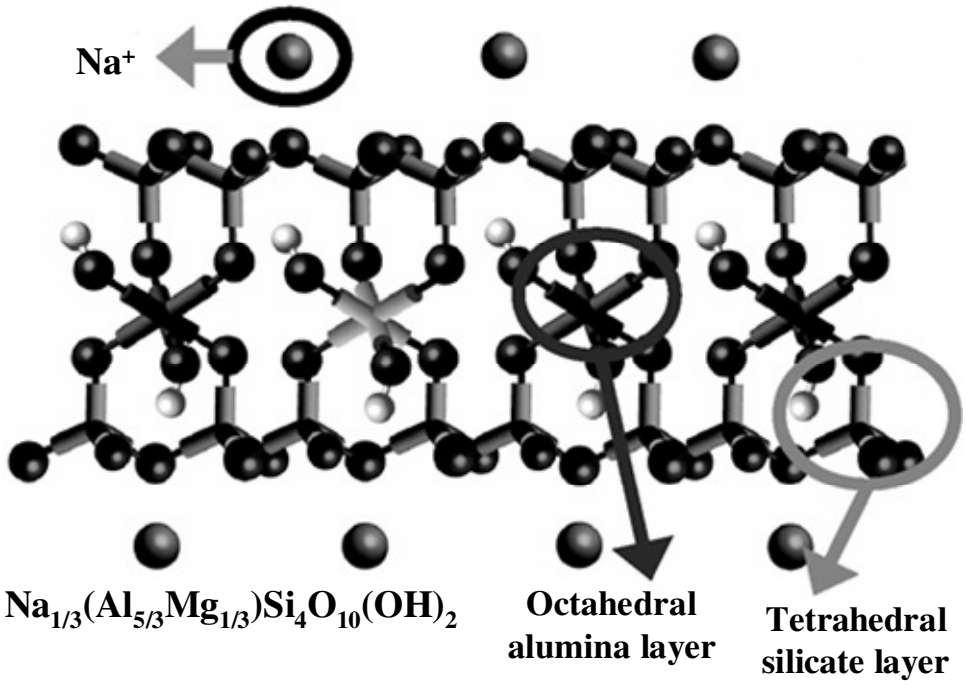

Figure 2. *Chemical structure of montmorillonite nanoclays (Reproduced from [34])*

Some important characteristics of clays relevant to the use of clays in polymer nanocomposites are their rich intercalation chemistry, high strength and stiffness, high aspect ratio of individual layers, abundance in the nature and low cost.

The mixture of a polymer-layered silicate mix may not spontaneously form a nanocomposite due to poor physical interaction between the organic and inorganic components which eventually leads to agglomeration of clays hence poor mechanical and thermal properties. If a strong interaction is achieved on the other hand, this will lead to the dispersion of silicates at nanometer scales and to improved mechanical and thermal properties. Pristine layered silicates usually contain hydrated Na^+ or K^+ ions which makes then hydrophilic and miscible with only hydrophilic polymers such as poly(ethylene oxide) (PEO) or poly(vinyl alcohol) (PVA). To make layered silicates miscible with other

polymer matrices surface modification of clay minerals is crucial. Generally this is done through various types of organic treatment such as exchanging the interlayer inorganic cations (Na^+, K^+, Ca^+, etc.) with organic ammonium cations. Another method is to swell the interlayer space and reduce the layer-layer attraction. These treatments make the clays more hydrophobic hence they become more compatible with the polymers [9, 39].

2.4 Polymer – Layered Silicate (PLS) Nanocomposites

It is well known from fiber reinforced composites that increasing the aspect ratio of the inorganic filler results in an increased modulus. As introduced recently the field of particle-reinforced polymers has given rise to another thought due to the increased specific surface area and thus, the amount of interfacial area [40]. In 2-D nanocomposites, these effects are combined. On the one hand, nano-scopic layered fillers allow for the retention of aspect ratios in excess of 1000 during normal polymer processing, something that is exceedingly difficult to achieve with conventional fillers. On the other hand, such systems also benefit from the extremely large amount of interface due to full dispersion of nanometer thick silicate layers in the polymer matrix. This combination is possible only in the nanometer regime and leads to properties not found in micro and conventional composites.

Depending on the amount of crystallinity of polymers additional changes may arise. It was reported on nylon-6/clay nanocomposites that there are changes to the crystalline structure of nylon-6 due to clays in which case, the layered silicate appeared to stabilize the metastable gamma phase, whose crystal structure is more densely packed than that of the most-favored alpha phase. Whether this is due to hydrogen bonding of the

polymer to the silicate surface or issues of confinement or local density variations, this change is of great importance, as the properties of gamma nylon-6 are not the same as those of alpha nylon-6, and the occurrence of the former will greatly affect the material properties such as mechanical and barrier [1, 2]. Other polymers may show similar behavior as long as the polymer/silicate interactions are strong enough and the polymer has multiple crystalline forms—as observed in the case of poly(vinylidene fluoride) nanocomposities, for example [41, 42]. The arrangement of the layers themselves can also be another impact such as creating a protective char layer and acting as a diffusion barrier to further combustion. Similarly, alignment of clay layers can improve barrier properties of polymers.

By mixing polymers with clays thermodynamically there are two types of layered clay nanocomposites that can be achieved: intercalated and exfoliated, depending on the organization of the clay layers as illustrated in Figure 3. If the polymer is located between the clay layers while increasing the layer spacing but not able to prevent the attractive forces between the clay layers which cause the layers to be regularly spaced stacks or tactoids, this nanocomposite is called intercalated. On the other hand, if the layer spacing is increased to the point where there is no longer attractions between the layers to cause a uniform layer spacing hence a random dispersion is achieved, the nanocomposite is called exfoliated [43]. With increasing clay loading, exfoliation of the platelets becomes more limited [35, 36, 44]. For polymer layered silicate (PLS) nanocomposites second characteristic of layered silicates is the bonding between the polymer and the silicate layers. Generally layered silicates have a thickness of ~1nm and an aspect ratio of ~1000.

Thus, compared to the conventional loadings, even a few percent of clay loading, when well dispersed, can create a high surface area for matrix-reinforcement interactions.

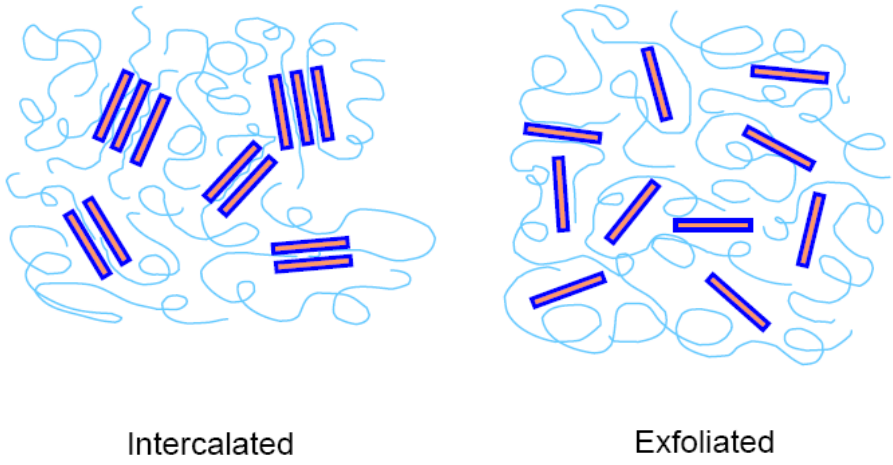

Figure 3. *Schematic illustration of thermodynamically achievable polymer/layered silicate nanocomposites*

PLS nanocomposites, formed with either modified or unmodified silicates, show a significant improvement in material properties such as increased modulus, strength, heat resistance and reduced gas permeability and flammability even at very low (≤5 wt%) clay loadings. The main reason for the improved properties is the interfacial interaction between the polymer matrix and clay nanoplatelets due to very high specific surface area (m^2/g) of platelets [9]. Several of the functions of these improvements are listed below [34]:

- *Thermal:* increased thermal resistance, higher glass transition temperature (T_g) or heat distortion temperature (HDT), reduced coefficient of thermal expansion (CTE)
- *Mechanical:* increased modulus, strength, toughness, elongation (in some cases)

- *Chemical:* improved solvent resistance, improved moisture resistance
- *Electrical:* improved thermal conductivity, lower resistivity (depends on the nanoparticles)
- *Barrier:* reduced oxygen, moisture transmission
- *Optical:* clear, transparency provided in selective systems
- *Others:* abrasion resistance, reduced shrinkage

There are quite a number of published studies on the property enhancements of PLS materials. It has been shown by many researchers that the inclusion of clay to the polymer matrix has a significant effect on the matrix mechanical strength such as tensile modulus and stiffness [45-50]. Usually, the incorporation of clay into the polymer matrix was found to enhance thermal stability by acting as a superior insulator and mass transport barrier to the volatile products generated during decomposition [45, 51-53]. Other thermal properties of polymers such as crystallization (T_c) and melting (T_m) temperatures have also been observed to be altered with clay loading [51-53]. Due to the increase in the restricted segmental mobility of the polymer chain with the clay loadings, the glass transition temperature of many polymers are also changed [45, 46, 48, 54, 55].

2.4.1 Preparation of PLS nanocomposites

Preparation of PLS nanocomposites are divided into three main groups: solvent casting, in-situ polymerization and melt blending [9, 37]. Below the details about each method is given and in Table 3 a comparative summary for each preparation method is provided.

Solvent casting is one of the simplest techniques by which nanocomposites are produced. It is based on swelling silicate layers using polymers dissolved in a solvent. Initially, the silicate layers are swollen in a solvent such as chloroform, water or toluene, and then it is mixed with the polymer solution. Upon mixing, polymer chains replace solvent molecules between the silicate layers. The solvent imparts the enhanced degree of freedom the polymer needs to intercalate between the silicate layers, while thermodynamic compatibility and physical mixing give rise to a dispersed system. A solvent should be chosen that completely dissolves the polymer and completely disperses the silicate. The solvent is then allowed to evaporate, leaving the nanocomposite behind, typically as a thin film.

In-situ polymerization is based on swelling the silicate layers in a (liquid) monomer or a monomer solution. In this method, polymerization can occur between the intercalated layers. Heat, radiation or an inorganic initiator can be used as initiators for the polymerization. For successful mixing the silicates must be compatibilized to allow the monomers to intercalate, at which point the polymerization reaction can take place in the inter-layer galleries. If the silicate surface layer or some silicate-bound functionality catalyzes the polymerization reaction and enhances its rate with respect to material outside of the interlayer galleries, dispersion may be strongly enhanced, up to the gel point at least. Such a situation can be encouraged through the use of silicate-bound monomers or initiators. Alternatively, emulsion polymerization may be performed by dispersing an unmodified silicate in a water/monomer emulsion. In any case, dispersion obtained via *in-situ* polymerization may improve the barrier and thermal properties but may or may not improve the mechanical performance, depending on the level of

polymer/silicate interactions. Without thermodynamic compatibility, the silicate layers may even collapse to form multilayer stacks if the nanocomposite is heated.

Melt blending is similar to solvent casting in the sense that the polymer is given enhanced degree of freedom polymer chains meed, combined with physical mixing, to disperse compatibilized layered silicates on the nanoscale. The enhanced degree of freedom of the polymer chains comes simply from thermal energy. Using an extruder or heated mixing chamber of some sort, the molten polymer and the compatibilized layered silicate are physically mixed, and a nanocomposite is obtained. Again, the mixing can be performed via something like stirring (i.e., the use of mixing screws in an extruder setup). Compared to in-situ intercalative polymerization and polymer solution intercalation, melt intercalation has advantages of being environmentally and economically friendly since no solvents are involved and allow the use of polymers which are not suitable for the former two methods. Besides, the lack of solvent in this technique also solves other problems associated with solvent casting such as no impurities or residues are introduced into the sample, settling is generally not an issue (due to the high viscosities of most polymer melts), and there are no concerns about complete evaporation or the retention of a small amount of a plasticizing solvent. For a given set of mixing conditions, the polymer microstructure is affected only by the composition of the nanocomposite, and pieces of highly varying geometry and size may be produced without problems.

Table 3. *Processing techniques for clay-based polymer nanocomposites (Reproduced from [39])*

Processing	Drive Force	Advantages	Disadvantages	Examples
In-situ polymerization	Interaction strength between monomer and clay surface; Enthalpic evolvement during the interlayer polymerization.	Suitable for low or non-soluble polymers; A conventional process for thermoset nanocomposites.	Clay exfoliation depends on the extent of clay swelling and diffusion rate of monomers in the gallery; Oligomer may be formed upon incompletely Polymerization.	nylon 6, epoxy, polyurethane, polystyrene, polyethylene oxide, unsaturated polyesters, polyethylene terephthalate
Solution exfoliation	Entropy gained by desorption of solvent, which compensates for the decrease in onformational entropy of intercalated polymers.	Prefer to water-soluble polymers.	Compatible polymer-clay solvent system is not always available; Use of large quantities of solvent; Co-intercalation may occur for solvent and polymer.	epoxy, polyimide, polyethylene, polymethylmethacrylate
Melt intercalation	Enthalpic contribution of the polymer-organoclay interactions.	Environmental benign approach; No solvent is required; Nanocomposites can be processed with Conventional plastic extrusion and molding technology	Slow penetration (transport) of polymer within the confined gallery.	nylon 6, polystyrene, polyethylene terephthalate

2.4.2 Existing and potential applications for PLS nanocomposites

The first commercial product of clay based polymer nanocomposites is the timing belt cover made by combination of nylon 6 with clay in Toyota Motors in early 1990s. Nylon 6 nanocomposites have also been used as engine cover, oil reservoir tank and fuel hoses in the automotive industry because of their remarkable increase in HDT and enhanced barrier properties together with their mechanical properties. Apart from nylon

6, other thermoplastic polyolefin nanocomposites were employed by General Motors for step assist on Safari and Chevrolet in 2002. It is now expected that polymer nanocomposites can be utilized as potential materials in various vehicles for external and internal parts such as mirror housings, door handles and under the hood parts. It is now predicted that widespread use of polymer nanocomposites would save 1.5 billion liters of gasoline over the life of one year production of vehicles and reduce related carbon dioxide emissions by more than 5 billion kilograms [39, 56].

Another application for clay based nanocomposites is food packaging. The excellent barrier properties of these composites would result in considerable enhancement of shelf life for many types of packaged food. Meanwhile, the optical transparency of polymer nanocomposite films is similar to their conventional counterparts. Therefore, these property enhancements would make them applicable widely in packaging industries as wrapping films and beverage containers. For example Bayer developed a new grade of plastic films for food packaging which are made from nylon 6 exfoliated clay nanocomposites.

Some other application areas for these materials are coatings and pigments, elctromaterials, drug delivery; and sensors and medical devices. Nanopigments made from clays and organic dyes are believed as potential environmentally friendly substitutes for toxic cadmium (Cd) and palladium (Pd) pigments. Materials dyed with nanopigments remain transparent as the size of these pigments is smaller than the wavelength of light. In addition, an improved oxygen, ultraviolet (UV) and temperature stability combined with high brilliance and color efficiency has been displayed which is probably due to the huge specific surface area of nanopigments. On the other hand the remarkable

electrochemical behavior of polymers associated with clay minerals attracts potential applications such as electrodes, biosensors, solid-state batteries and smart windows. Polymer clay nanocomposites are applicable to not only the above mentioned areas but also many other areas. For instance, flame retardancy of polymer materials is required in many applications, such as in automotive parts, personal computers, and building materials.

2.4.3 Characterization Techniques for PLS Nanocomposites

Characterization involves two main processes: structure analysis and property measurements. Structure analysis is carried out using a variety of microscopic and spectroscopic techniques, while property characterization is rather diverse and depends on the individual application. Various techniques have been employed to study polymer nanocomposites as summarized in Table 4. The structure of polymer nanocomposites is generally characterized by X-ray diffraction (XRD) and transmission electron microscopy (TEM). Either intercalated or exfoliated nanostructure can be studied by monitoring the position, shape and intensity of the basal reflections of XRD patterns of the materials. For instance, the extensive layer separation in an exfoliated nanocomposite is reflected in the disappearance of any coherent XRD whereas the finite layer expansion in an intercalated nanocomposite is associated with the appearance of a new basal reflection corresponding to the layer gallery distance. However, we should be cautious about data from XRD when the layer spacing in intercalated nanocomposites exceeds 6-7 nm or when the layers become relatively disordered in exfoliated nanocomposites. In that case, simultaneous use of small angle X-ray scattering (SAXS) with wide angle XRD can

yield quantitative characterization of the structure in polymer nanocomposites. Moreover, TEM can provide direct qualitative information of structure, morphology and spatial distribution of the various components as well as the defect structure while nuclear magnetic resonance (NMR) is used for probing surface chemistry and coordination in exfoliated nanocomposites to quantify the level of exfoliation. Fourier transform infrared (FTIR) and Raman spectroscopy are also used to understand structural formation of polymer nanocomposites [39].

General polymer characterization techniques are also used to measure materials properties of PLS composites. Among them, DSC is used to measure the thermal transitions such as melting, glass transition and crystallinity; TGA is used to evaluate the thermal stability at elevated temperatures. Melt rheology is another important area where the processibility of nanocomposites are studied and the effects of clays on the polymer processing examined.

Among the characterization techniques listed above, only a few of them such as SAXS, WAXS and NMR provide the opportunity for *in-situ* observation during deformation of nanocomposite films. In these techniques we have chosen simultaneous application of SAXS and WAXD as the combination of these two techniques allows a wide range of sizes to be probed (approximately 0.1 - 500 nm). When measured simultaneously, these two scattering techniques provide a very detailed understanding of the structure of crystalline and the amorphous parts of the polymer as well as the clay platelets.

Table 4. *Common characterization techniques for clay based polymer nanocomposites (Reproduced from [39])*

Techniques	Characteristics and properties
XRD (WAXD)	Degree of swelling and interlayer distance of clays Dispersion degree of clay platelets Morphology (intercalated or exfoliated) and its development Kinetics of intercalation process
SAXS	Phase behavior and structure evolution Lamellar texture and thickness Dispersion of clay platelets Morphology (intercalated or exfoliated)
SEM	Surface roughness and morphology Dispersion degree of platelets
TEM/HRTEM	Morphology and its development Microstructure Spatial distribution of clay platelets Structural heterogeneities Defect structure and atomic arrangement
AFM	Crystallization behavior of polymer Surface roughness Particle size and distribution Morphology and microstructure (exfoliated or intercalated)
FTIR	Component identification and analysis Interfacial interactions Crystallization and orientation of polymer
NMR	Local dynamics of polymer chains Morphology and dispersion of clay platelets Surface chemistry
TGA DSC	Thermal stability Melting and crystallization behavior Local dynamics of polymer chains
Cone calorimetry	Flame retardancy (heat release and carbon monoxide yield) Thermal stability
Rheometry	Nanorheology
Mechanical test	Young's modulus Tensile strength Elongation at break Viscoelastic properties

2.5 X-ray scattering from polymers

X-rays are electromagnetic radiation with a wavelength in the range of 10 to 0.01 nm, with corresponding frequencies in the range 30×10^{15} to 30×10^{18} Hz. X-rays have wavelengths that are longer than γ-rays, but shorter than UV-rays. X-ray scattering techniques are a family of non-destructive analytical techniques which reveal information about the structure, chemical composition, and physical properties (i.e. exfoliation degree, crystallinity ratio …etc) of materials. When X-rays impinge on the electrons in an atom, these electrons become secondary emitters of X-rays and atoms i.e. scattered X-rays. The scattering could happen in two ways, either coherently or incoherently, where the former takes the major part of the energy of scattering. Coherent scattering provides structural details of the material since the wavelength and phase of the X-rays are unchanged after scattering by the atoms. Whereas incoherent scattering has no relationship in phase between the scattered and incident X-rays and it has a range of wavelength after scattering. Incoherent scattering therefore appears as a background scattering intensity to the X-ray experimental measurements [57].

Polymers chains can arrange themselves into crystalline, semi-crystalline or amorphous conformations. The amount of crystallinity is an important issue in terms of the applications of polymers. Different polymers crystallize to different extents and the structure, anisotropy and orientation are critical factors to be determined by scattering. X-ray studies on polymer structures generally include small angle scattering ($2\theta<5°$) and wide angle scattering ($2\theta>5°$).

Due to the inverse relationship between dimension and scattering angle, large structures therefore are observed in the small angle regime. The scattering in this case

arises from electron density fluctuations over lengths of ~100A or larger which may originate from density differences, composition differences or both and they do not need to have any periodicity. Therefore perfect single crystals, pure phases and homogeneous substances scatter very weakly in the small angle regime. For polymers, electron density variations can originate from differences in crystalline and amorphous regions and the presence of micro-voids dispersed in polymer matrix. The intensity of small angle scattering increases with the degree of contrast between the electron densities differences between regions that produce the heterogeneity [57-59].

Wide angle scattering from semi-crystalline polymers is expected to broad diffraction peaks due to the variation in crystalline domain sizes. In these systems the fluctuations in electron density occur over lengths less than ~100A. Wide angle scattering (often referred to as diffraction) is often used to determine the crystalline structure of polymers (unit cell dimensions, etc) as well as the degree of crystallinity and the size of crystal domains [57-59].

We can consider the diffraction of X-rays by an assembly of atoms as if they were point scatterers. When a parallel beam of X-rays with a wavelength of λ fall on a row of regularly placed atoms at an angle of θ, as shown in the Figure 4 , it is seen that the scattered waves by the atoms of the matter would be in phase only when the path ($|AB| + |BC|$) equals:

$$|AB| + |BC| = n\lambda \tag{1}$$

where n is an integer. This path length is the extra distance that must be traveled by the second parallel beam.

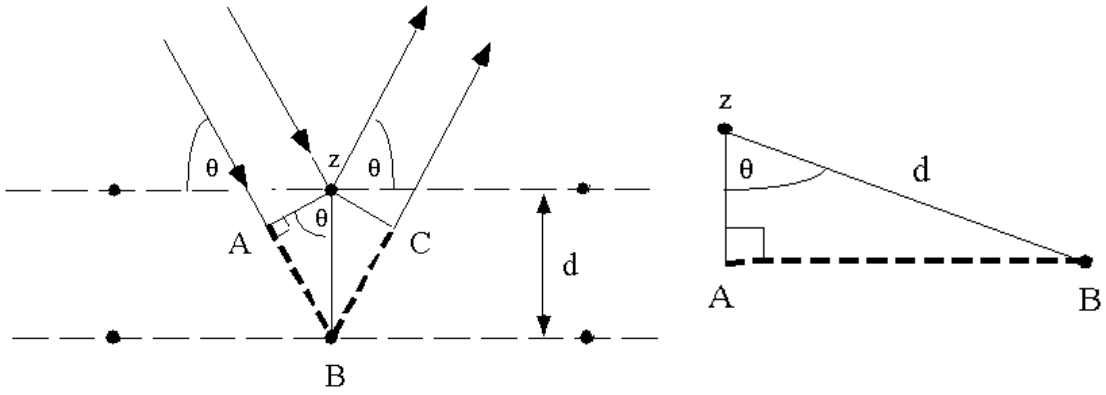

Figure 4. *Geometry of the Bragg's diffraction theory.*

Since the distance $|AB|$ is equal to the distance $|BC|$, calculating $|AB|$ by trigonometry, we see that $|AB| = dSin\theta$. By substitution, the familiar Bragg equation is obtained:

$$|AB| + |BC| = 2dSin\theta = n\lambda \Rightarrow n\lambda = 2dSin\theta \quad (2)$$

Equation 2 therefore allows us to calculate inter-planar distances, *d* [57]. The use of the equation developed by Bragg, which is considered a simplified version of Scherrer's equation, is a well-established method widely employed in polymers to calculate crystal size from X-ray patterns [58]. The equation is as follows:

$$L_{hkl} = \frac{K\lambda}{\beta_{hkl}\cos\theta} \quad (3)$$

where K is the scattering factor which is assumed to be 1 for polymers, β_{hkl} is the width of the diffraction peak measured at half the maximum intensity (FWHM), and L_{hkl} is the crystal size. As the equation indicates the broadening of a peak is related to the crystal size inversely.

In order to analyze the data to obtain the structural information, raw intensity has to undergo several corrections. The data is corrected for; background transmission due to air scattering and the effects of sample holder; possible changes in incident beam intensity during data collection; and, sample absorption effects. And the data can also be smoothed to eliminate the random noise. In addition averaging the repetitions of the same experiment is used to verify the sample behavior and eliminate "bad" data caused by equipment malfunction. Sample to detector distance must be calibrated by reference to standards which have sharp scattering patters, for instance; collagen for SAXS, silver behenate for MAXS and silicon for WAXS, in order to determine the scattering vector accurately.

The intensity is later corrected by Lorentz weighting factor dependent on the geometry of the sample. In an isotropic sample, intensity is scattered in reciprocal space over spheres of surface area $4\pi s^2$, where $s = 2\sin\theta/2 = q/2\pi$. To compare measured intensities spread over spheres of different radii, a Lorentz weighting factor of $4\pi s^2$ or q^2 is used. The choice about whether to use s or q as the scattering vector is a matter of taste. Data analysis of the Lorentz corrected intensity profile may involve application of Bragg's Law to find the spatial periodicity or calculation of the one-dimentional correlation function. In Figure 5 the scattering method as well as the intensity profile and correlation function transformation ($K(x)$) is shown [60].

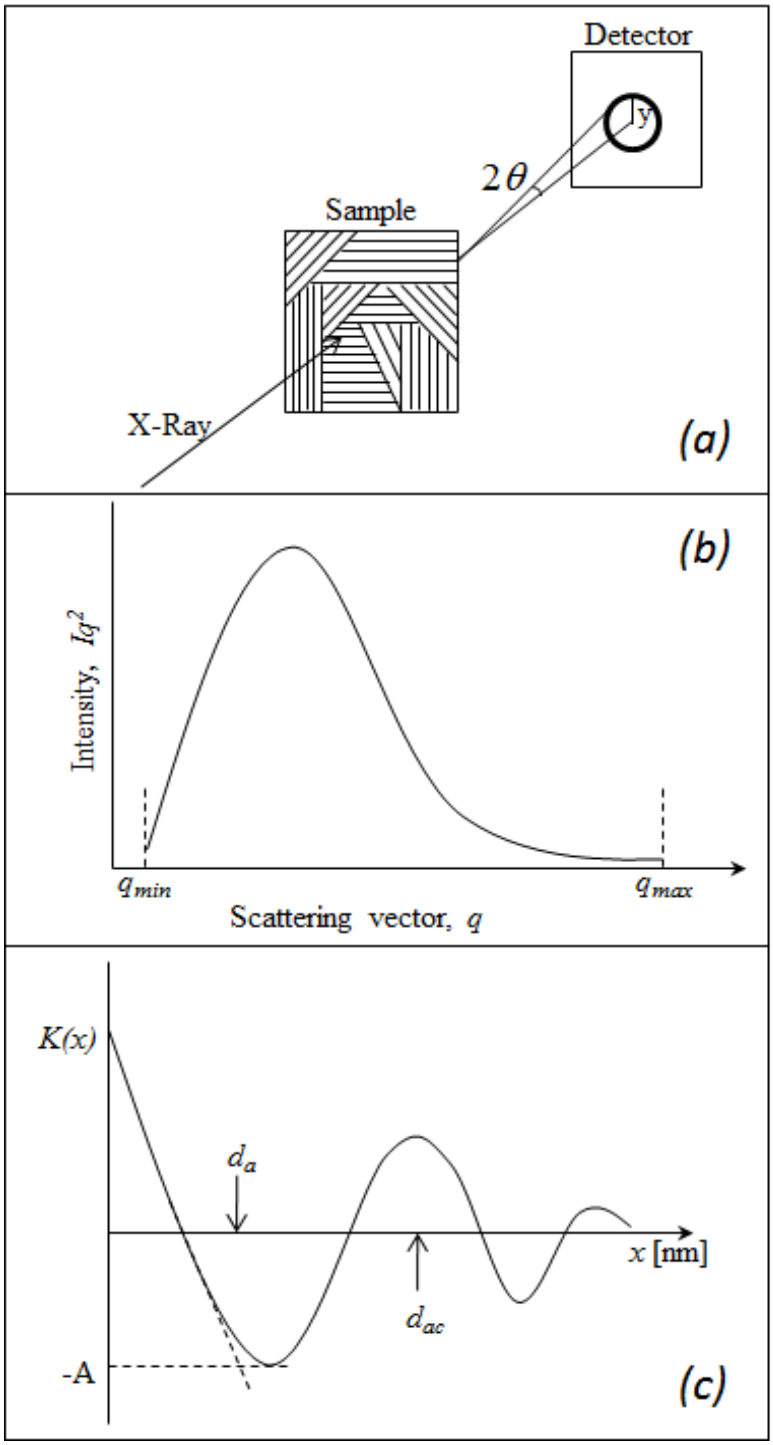

Figure 5. *(a) Experimental geometry showing incident x-rays on a sample, (b) Lorentz corrected intensity, Iq^2, vs. scattering vector (q), in the small angle range, (c) One dimensional electron density correlation function, $K(x)$ vs. x (Reproduced from [57]).*

Small-angle X-ray Scattering (SAXS) has been widely used to probe the crystalline lamellar structure in semicrystalline polymers. The correlation function is routinely used to analyze the SAXS data. It can determine several important structural parameters in semi crystalline polymers, including the most probable average long period d_{ac}, the average crystalline lamellar thickness d_c, the average interlamellar amorphous layer thickness ($d_a = d_{ac} - d_c$), linear crystallinity α_c, and more. If the absolute scattering intensity is measured, the electron density difference between the crystalline phase and the amorphous phase can also be obtained [57, 61-63]. In isotropic polymer systems, the one-dimensional (1D) correlation function can be appropriately used to probe the three-dimensional (3D) microstructure. The 1D correlation function, noted as *K(x)*, is the Fourier transformation of the Lorentz-corrected SAXS profile. *K(x)* is a spatial correlation of two electron density fluctuations at a distance r defined as [64]:

$$K(x) = \frac{< \rho(x_1)\rho(x_2) >}{< \rho^2 >_{av}} \tag{4}$$

where $\rho(x_1)$ and $\rho(x_2)$ are the local electron density profiles at spatial points x_1 and x_2, respectively, at a distance of x, and $< \rho^2 >_{av}$ represents the average square of the electron density fluctuations. The normalized correlation function *K(x)* can be related to the Lorentz-corrected scattering intensity $q^2I(q)$ through the following equation:

$$K(x) = \frac{\int_0^\infty q^2 I(q)\cos(qx)dq}{\int_0^\infty q^2 I(q)dq} \tag{5}$$

As shown in Figure 5, the intensity data cover a finite range of q. No intensity data is available below q_{min} , which is determined by the beam stop. On the other hand the width of the detector and the sample to detector distance limit q_{max}, the largest value of q obtainable. These intensity cut-offs have implications for calculation of $K(x)$, since the integration limits extend from 0 to $+\infty$. Extrapolation to low q can be performed by Guinier plot by which I is plotted vs q^2, then extended from q_{min} to $q=0$. Simple extension by linear extrapolation of the plot of I vs. q below q_{min} is also used. The extrapolation techniques change the total area under the scattering curve, but the Lorentz correction reduces the ultimate effect of low q extrapolations on curve area [60].

2.6 Synchrotron radiation – Brief history and basics

X-ray diffraction/scattering research has benefitted considerably from synchrotron radiation. The high fluxes of synchrotron x-ray radiation have opened new possibilities such as time-resolved scattering, simultaneous dynamic scattering and DSC, and mechanical experiments.

Since the first synchrotron radiation observation was performed in 1947 at General Electric Research Laboratory in Schenectady, New York, it has evolved and today fourth generation synchrotrons are being built. To simply define synchrotron radiation it can be said that it is basically eelectromagnetic radiation, given off when very high energy electrons encounter magnetic fields (see Figure 6).

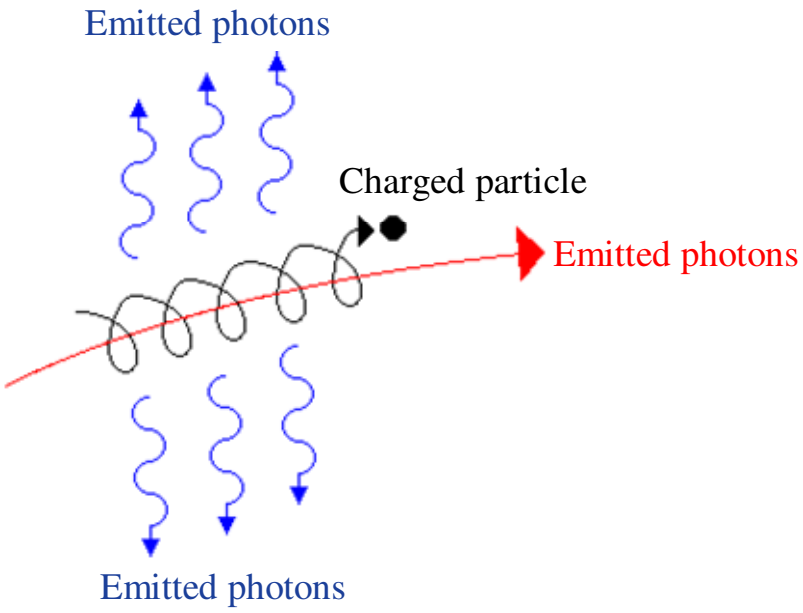

Figure 6. *Schematic of generating synchrotron radiation.*

First generation synchrotron measurements began at Synchrotron Ultraviolet Radiation Facility (SURF) to determine the potential of synchrotron radiation for standards and as a source for spectroscopy in the ultraviolet. Absorption spectra of noble gases revealed a large number of previously unobserved resonances due to inner-shell and two electron excitations, including doubly excited helium, which is still used for studying electron-electron correlations. However later SURF had outlived its usefulness for nuclear physics and was no longer used for this purpose. The next major advance in synchrotron radiation was the development of storage rings which is the basis for all of today's synchrotron sources. With the operation of first storage ring, Tantalus I, the superiority of the storage ring as a source became evident. Since about 1980, fully dedicated storage ring sources have been completed in several countries. They are called

second-generation facilities to distinguish them from the first-generation rings that were built for research in high-energy physics.

Special magnets may be inserted into the straight sections between ring bending magnets to produce beams with extended spectral range or with higher flux and brightness than is possible with the ring bending magnets. These devices, called wiggler and undulator magnets, utilize periodic transverse magnetic fields to produce transverse oscillations of the electron beam with no net deflection or displacement. They provide another order-of-magnitude or more improvement in flux and brightness over ring bending magnets, again opening up new research opportunities. However, their potential goes well beyond their performance levels, in first- and second-generation sources.

Third-generation sources are storage rings with many straight sections for wiggler and undulator insertion device sources and with a smaller transverse size and angular divergence of the circulating electron beam. The product of the transverse size and divergence is called the emittance. The lower the electron-beam emittance, the higher the photon-beam brightness and coherent power level. With smaller horizontal emittances and with straight sections that can accommodate longer undulators, third-generation rings provide two or more orders of magnitude higher brightness and coherent power level than earlier sources.

Today, there are more than fifty synchrotrons worldwide but the facilities vary in their capacity and the brightness of the light they produce. The top three world's most powerful synchrotrons are "Advanced Photon Source (APS)" in the United States of America, "European Synchrotron Radiation Facility (ESRF)" in France and the "SPring-

8" facility in Japan. The SPring-8 synchrotron is the most powerful and the biggest synchrotron in the world [65].

The synchrotron was developed by elementary particle physics in order to accelerate electrons, positrons, protons and other particles. It consists of a ring with a diameter of about a few meters up to a kilometer in which a vacuum of 10^{-7} mbar can be sustained and to which strong electric and magnetic fields can be applied (see Figure 7). A bunch of electrons and positrons is first accelerated in a linear accelerator to an energy usually lying between 40 MeV and 380MeV. Afterwards the bunch is injected into the synchrotron. At several positions where the ring is bended strong magnetic fields are applied which force the particles to move on a curved line. In the parts of the ring between the magnetic fields the particles move on straight lines, where strong electric fields are applied to accelerate the particles. In the time when they are circling the energies of the particles reach up to 7.5 GeV. The electric and magnetic fileds are not constant but alternate with high frequency. After the particles have reached the wanted energy, they are injected into the storage ring. The storage ring is built in a similar was as a synchrotron. Electrons and positrons are orbiting in opposite direction in two parallel the same properties concerning synchrotron radiation. Typical life time of a filled storage ring is of 2-20 hours. During this period an initial current of 300mA decreases to about 100 mA [59, 66, 67].

The synchrotron radiation opened new possibilities in scientific investigations because of the following reasons:

(1) The wavelength ranges continuously from about 10^{-2} mm to 0.01 nm.

(2) The intensity of the radiation as well as the brightness of the source are very high compared to the conventional sources.

(3) The beam is highly collimated.

(4) The radiation is almost completely polarized.

(5) The radiation consists of short pulses.

(6) The energy of radiation is well defined.

(7) It requires smaller specimens and provides better counting statistics.

All these properties of synchrotron radiation are also the reasons for being extremely useful for time resolved studies.

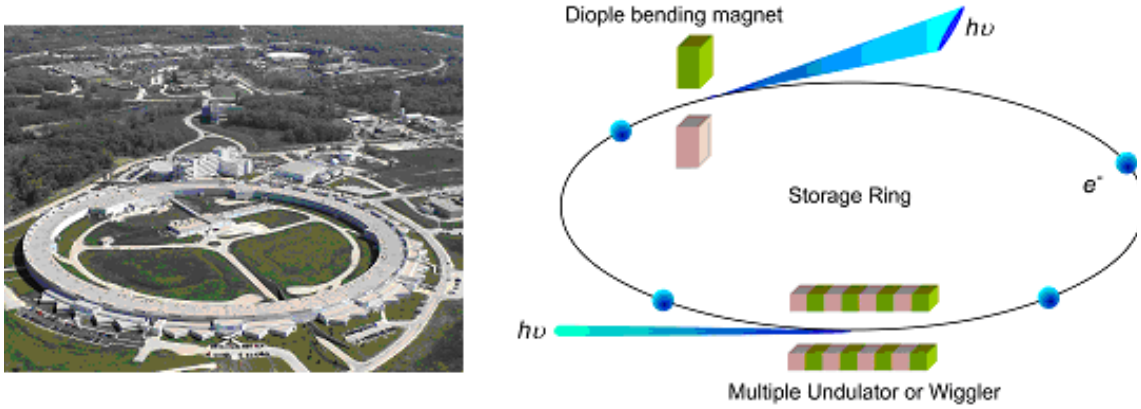

Figure 7. *A picture of Advanced Photon Source at Argonne National Laboratories, Chicago, IL on the left and the schematic of a synchrotron on the right.*

2.6.1 Synchrotron X-rays in Polymer Science

For most polymer systems the collection of a typical X-ray scattering pattern with a conventional X-ray tube or a rotating anode easily takes 30 minutes or more. With the high intensity beams now available at synchrotron sources, data can now routinely be

collected in a few seconds or even in matters of milliseconds, allowing for the time-resolved (*in-situ*) studies of rapidly changing structures as they occur such as during polymer crystallization, processing or deformation. The characterization of weakly scattering systems has become feasible in addition to the advantageous of X-ray tunability where absorption is a problem.

It has become possible to combine property related techniques with X-ray scattering experiments such as DSC [68, 69], temperature-modulated DSC [70, 71], tensile testing equipment [12, 15, 72], and rheometry [73, 74], AFM [75]; all of which allows for better elucidation of structure-property relations. In addition at synchrotron sources, in contrast to most laboratory set-ups, small angle and wide angle cameras are integrated, allowing for an accurate time correlation of structural development at different length scales.

On the other hand it is well known that the mechanical, thermal, optical, electrical and barrier properties of polymers can be significantly improved by the addition of inorganic nanofillers. As mentioned before, nanoparticles with potentially promising interactions with polymer matrices involve clay platelets and carbon-tubes and fibres. Despite the extensive research on PNCs, there is no generic quantitative model that allows one to design a nanocomposite with any given set of properties. The types of final morphologies formed from a large variety of starting recipes are known, as well as their effects on the nanocomposite properties. However, relatively little is known about how the morphologies reach their characteristic forms during processing, or how these structures subsequently behave under large-scale deformation to fracture.

The use of combined SAXS/WAXS measurements has been shown to be a very powerful method for *in-situ* measurements of polymer structures during processing operations such as uniaxial stretching and fiber formation in order to characterize the deformation behavior of semi-crystalline polymers. These studies have elucidated the influence of several parameters on the polymer morphological evolution such as strain, strain rate, and temperature [11, 15, 76, 77]. Although observations of uniaxial deformation are very important to understand the fundamental behavior in a controlled system, under many processing conditions, such as blow molding and thermo-forming, the deformation is more complex and often multiaxial. In order to predict the properties of polymers prior to and after processing, it is essential to study the morphological development of the polymers under multiaxial deformation. Moreover, it is essential to observe these changes occurring to the polymer morphology *in-situ*, thereby eliminating the effects of internal relaxations. There have been limited studies on morphological development of polymers resulting from biaxial deformation [78-81] and except for our own work [25] there has been no *in-situ* X-ray scattering studies published on multiaxial/biaxial deformations of polymers and polymer/clay nanocomposites.

In order to characterize the deformation of semi crystal polymers explicitly, it is required to record data *in-situ* during deformation. The drawback of ex-situ x-ray experiments is the relaxations happening within the sample with the removal of the stress. Due to internal relaxations, the behaviour of the polymer under stress is not screened efficiently when the x- ray experiments is performed after deformation.

In-situ type experiments provide precise details of morphological changes of polymers as well as the ordering of clays. In this respect, synchrotron x-ray

measurements have been shown to be a powerful technique for characterization of polymer crystallites. *In-situ* X-ray scattering studies have shown the influence of several parameters on the polymer morphology evolution such as strain, strain rate, and temperature [11, 12, 15, 18, 20, 79].

A brief summary on *in-situ* SR observations during deformations of polyethylene and polypropylene can be found below.

Butler and co-workers have performed SR studies on low and high density polyethylene during uniaxial tension employing simultaneous SAXS and WAXS (see Figure 8). Their studies have shown that the start of cavitations, detected by SAXS, in the HDPE coincided with the onset of a stress-induced martensitic transformation detected by WAXS at a low macroscopic strain. It was found that in the HDPE possible lamellar stack rotation occurred whereas in the LDPE interlamellar shear was active. Altering the thermal history to change the degree of crystallinity and lamellar population altered the strain at which the martensitic transformation occurred. In the annealed LDPE a higher crystallinity delayed the onset of the transformation by allowing a greater amount of deformation to occur via other deformation mechanisms. In annealed HDPE, however, the transformation was activated at lower strains since less deformation of the amorphous component was possible. They have performed further studies on the effect of deformation temperature as well as compression as opposed to tension to understand the morphology evolution of polyethylene during deformation [11, 12, 15, 17, 72, 82].

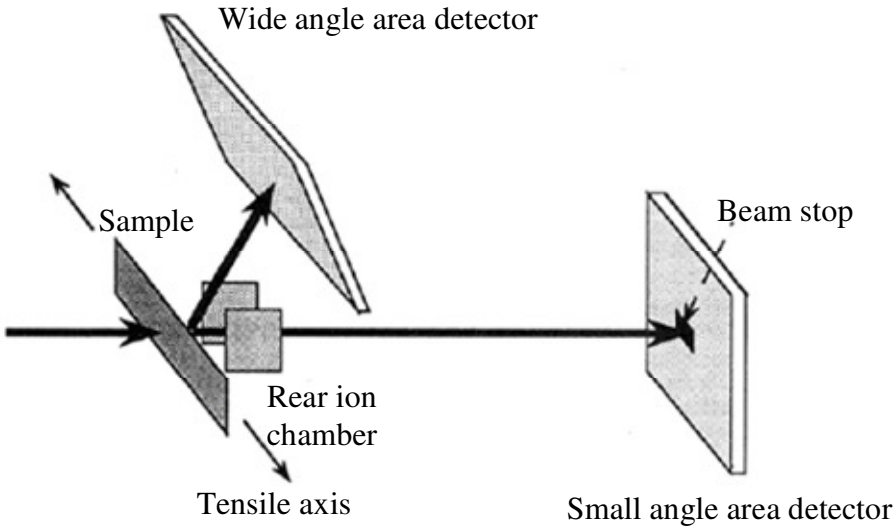

Figure 8. *Schematic diagram of the experimental setup for in-situ tensile test explained in [12].*

The effect of crystallinity and strain rate on the cavitations formation in PE during uniaxial deformations has shown that the cavitations initiate at the amorphous component of PE. Formation of cavitations were seen at higher degree of crystallinity due to the retarded deformation in crystals [83]. It was also observed that more cavitations occurred in PE when deformed at higher strain rates due to the limited degree of freedom of amorphous chains when deformed faster and at lower temperatures [11, 76]. Figure 10 explains the proposed deformation mechanism for the formation of cavities. According to their observations the increase in cavitation only during strain softening suggests that voids were formed by the release of constraints during lamellar disruption, supporting a mechanical transition for the fibrillar morphology in cold drawn samples. At low temperatures the motion of the chains is constrained by entanglements in the amorphous component and their reduced degree of freedom in the crystalline lamellae. Lamellar

fragmentation coupled with cavitations provides a mechanism for the release of these constraints.

Cavitations were seem to initiate at yield point during uniaxial deformations which also coincides with the onset of martensitic transformation from orthorhombic to monoclinic crystals in PE [84]. Butler and coworkers have also observed the that the martensitic transformation was initiated at yield point up to which the deformation was mostly happening in the amorphous region [11]. It was observed that the transformation of orthorhombic to monoclinic phase was metastable happening only under stress and mostly when the normal of the chain axis coincides with the tensile axis. In Figure 9, direct correlation between the monoclinic and orthorhombic intensities can be seen. Formation of cavities were reduced when PE was deformed at elevated temperatures as well as the amount and rate of martensitic transformation from orthorhombic to monoclinic crystallites [11, 12].

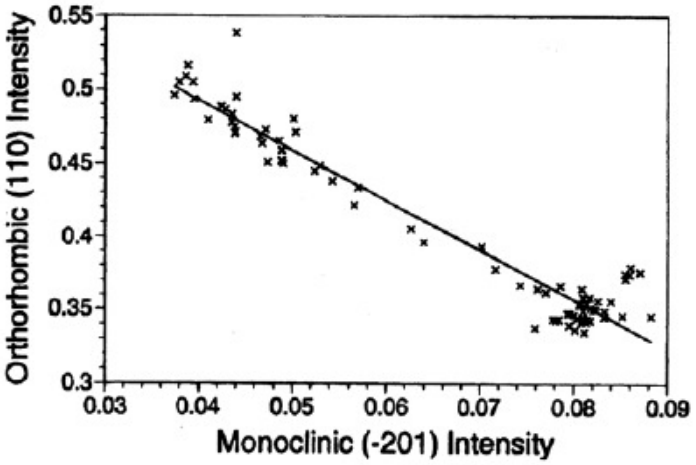

Figure 9. *Direct correlation between the deerease in the orthorhombic (110) intensity with the increase in the monoclinic (-201) intensity (in arbitrary units) (Reproduced from [12].*

In the further stages of deformation the monoclinic crystal intensity in PE was observed to reduce due to three possible reasons: (1) conversion back to orthorhombic structure due to local stress relaxations from formation of cavities, (2) partial melting of crystallites and (3) change in the molecular orientation due to deformation. Among these melting of crystallites is unlikely during deformations at room temperature [17]. Tang and coworkers have observed that there are three main stages in uniaxial deformation of PE. At the earlier stages, at smaller deformations, it was mostly the deformations in the amorphous regions which were followed by slippages occurring in micro fibrils. At the later stages non affine deformation of fibrils were observed [77].

From the limited studies published on the in-situ and ex-situ deformation behavior of PE/clay nanocomposites, the initiation of cavities were observed to start at the polymer-clay interface [85]. When strong interaction between the clays and the polymer chains is formed however, formations of cavities were reduced and toughness of polymer was improved due to polymer-clay shearing effect. Clay platelets were observed to orient the PE crystallites with respect to plane direction due to strong interactions. Figure 11 schematically explains the proposed deformation mechanism based on their observations.

In another study performed by Wang et. al. martensitic transformation was observed to start at the same strain for both the neat polymer and the nanocomposites. Tzavalas and coworkers have shown that the existence of clay platelets in PE caused less distortion on orthorhombic crystals [86, 87].

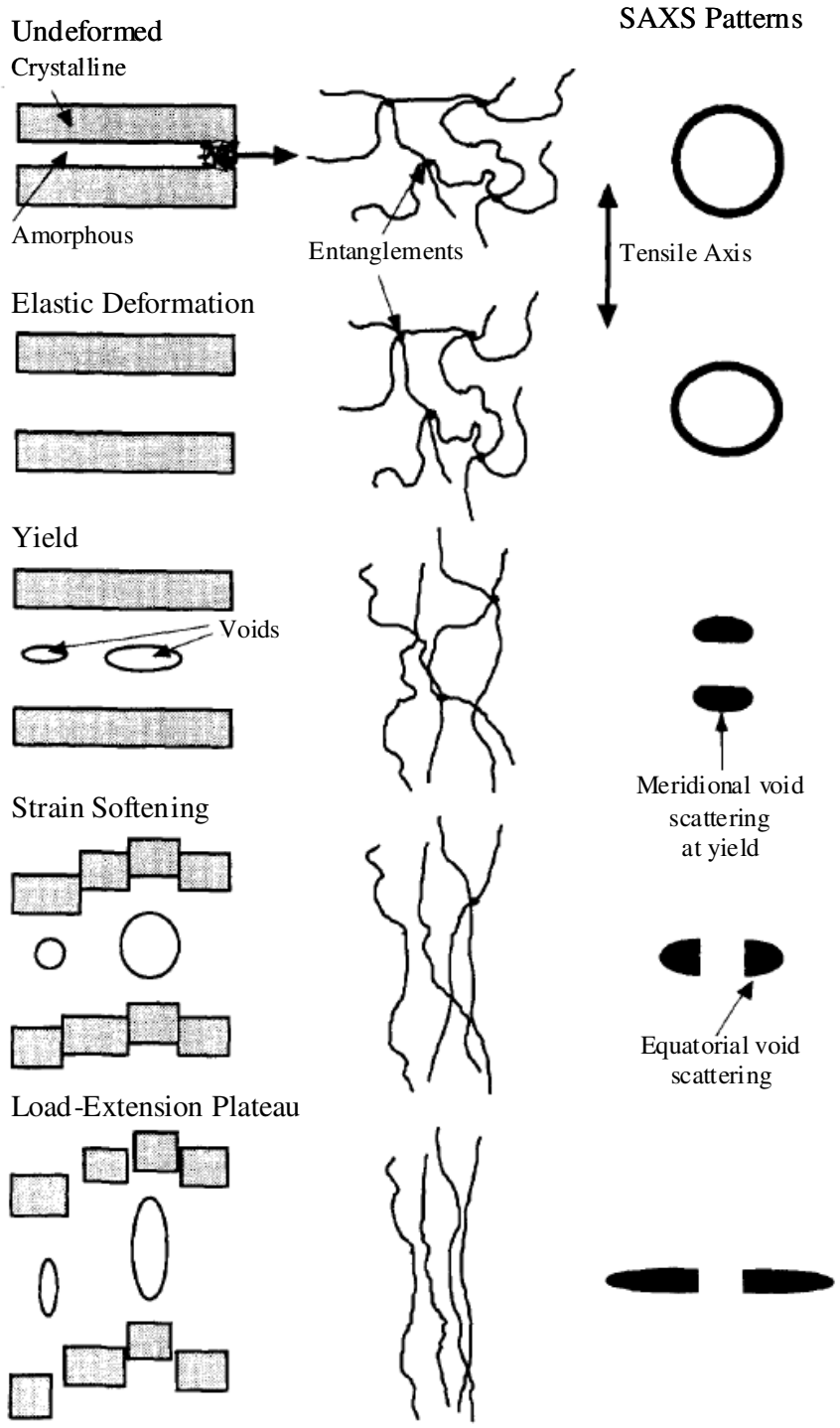

Figure 10. *Schematic illustration of the development of cavities in the interlamellar regions during deformation described by Butler et. al [11].*

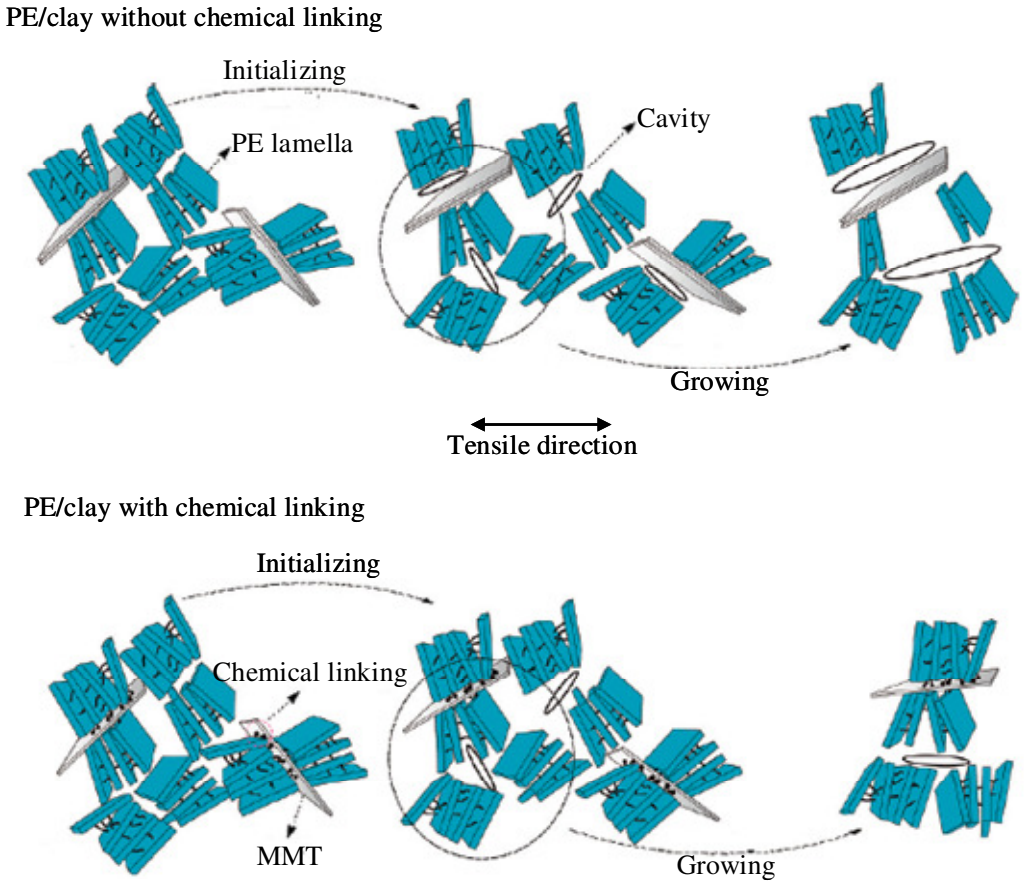

Figure 11. *Schematic representation of the morphology evolution, induced by tensile deformation at room temperature, for PE/clay nanocomposites with and without chemical linking between PE and MMT (Reproduced from [80]).*

Deformation studies of PP coupled with X-rays have shown that the in-situ observations eliminate the effect of nanostructure relaxations and allow one to determine the morphology evolution in more details [88]. 2D SAXS images from in-situ and stretch-hold experiments were shown in Figure 12 for comparison purposes. Machado and coworkers observed that under uniaxial deformation initially PP spherulites show orientation in the strain direction, which was followed by lamellar orientation. In the further stages of deformation disorder due to lamellar break-ups was seen [89]. One

common observation under uniaxial loading as well as sequential biaxial loading is the increase in long spacing due to extensions in the amorphous chains [18, 81, 90]. Being the most stable form α-PP is formed under standard crystallization conditions. However, slow crystallization of PP under high pressure results the formation of β-PP. It was observed that during uniaxial stretching, metastable β-PP converts into α-PP. Under biaxial deformation of PP, Capt et. al. have observed that the crystallite size reduces with increasing strain and spherulites converts into fibrils [91]. From the very few studies published on ex-situ PP/caly nanocomposite deformations, both shear flow and biaxial deformation were observed to induce clay orientation [92, 93].

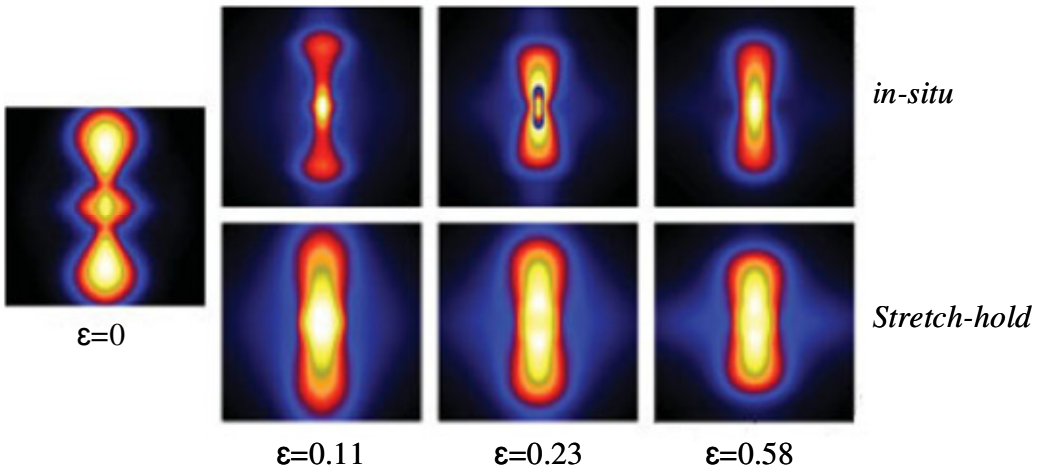

Figure 12. *Comparison between SAXS patterns recorded during a dynamic (top row, $\dot{\varepsilon} \approx 10^{-3}\ s^{-1}$) tensile test of hard-elastic PP films and results from the corresponding experiment in stretch-hold technique (bottom row) (Reproduced from [88]).*

As discussed above, whilst there have been a few attempts to determine the complex structural changes that occur during deformation of polymeric materials, these measurements are either made *in-situ* and *ex-situ* during uniaxial deformation or ex-situ

after biaxial deformation. Neither these cases are able to accurately monitor the morphological changes experienced by the polymers and their nanocomposites during processing. The literature to date has proven that more work in establishing structure-processing relationships of polymers is required to achieve an in-depth understanding of the behaviour of polymers during deformation processes. Therefore, our objective in this project is to perform *in-situ* synchrotron X-ray scattering studies of PP and PE clay nanocomposites under multi-axial loading which will mimic the processing conditions these materials go through. The effect of strain, strain rate and temperature on the morphology evolution of PLS materials will be examined.

CHAPTER III

DESIGN OF IN-SITU MULTI-AXIAL DEFORMATION DEVICE (IMDD)

As discussed in Chapter II, polymer nanocomposites offer enhanced material properties compared to their conventional counterparts as well as the pure polymer such as increased modulus and barrier properties and reduced flammability to the end user. For these reasons they appear to be a very popular focus of research for many researchers. Studies on these nanocomposites mainly focus on the preparations, characterizations and property testing of these materials. The types of final morphologies formed from a large variety of starting recipes are known, as well as their effects on the nanocomposite properties. However, relatively little is known about how the morphologies reach their characteristic forms during processing, or how these structures subsequently behave under large-scale deformation to fracture. There is still a gap in the structure-processing relationships of these materials and there is no common or known ways to predict the properties of a specific polymer clay nanocomposite prior to processing, or choosing a processing route according to requirements of a specific end-use.

With this work, we aimed to contribute to building structure-processing relationships of these nanocomposites where the outcomes will be used as baseline for further studies as this is one of very few reports on its kind. There have been earlier reports on the changes of structure of neat polymers during uniaxial stretching and fiber formation however limited number of published work on biaxial or multiaxial

deformations of polymers are quite rare, moreover this number further reduces in the case of polymer/clay nanocomposites. As we studied the reports on the in-situ observations during multiaxial deformations of polymers and polymer-clay nanocomposites, we have seen that there is no report other than our own. Observations of uniaxial deformation are very important to understand the fundamental behavior in a controlled system and the affects of strain, strain rate and temperature on the polymer morphology change; however under many processing conditions, such as thermo-forming and blow molding, the deformation is more complex and often multiaxial. In order to predict the properties of polymers prior to and after processing, it is essential to study the morphological development of the polymers under multiaxial deformation. Furthermore, it is essential to observe these changes occurring to the polymer morphology *in-situ*, thus eliminating the effects of internal relaxations.

3.1 Discussions on earlier biaxial and multiaxial deformation designs

There have been some biaxial and multiaxial deformation devices reported in the literature to study deformation behavior of polymers. Here they will be discussed and the reasons for necessity of a new and unique design to perform in-situ deformation and x-ray studies will be discussed.

One way of creating biaxial deformation is to fix the sample on two orthogonal sides and strain the sample via the two opposing sides as seen in Figure 13. This only requires use of two motors and makes the device relatively small. However, in order to follow structural changes in a polymer during deformation using a scattering measurement, the incident beam should ideally be maintained at the same position on the

sample throughout the deformation process. By measuring the scattering from the same position removes the ambiguity of variations in behavior which might exist across the sample. More importantly in the biaxial deformation shown in Figure 13 all points in the sample move relative to the initial sample position, making scattering measurements of the same sample scattering volume difficult to achieve with a fixed x-ray beam consequently this design is not suitable for in-situ x-ray measurements.

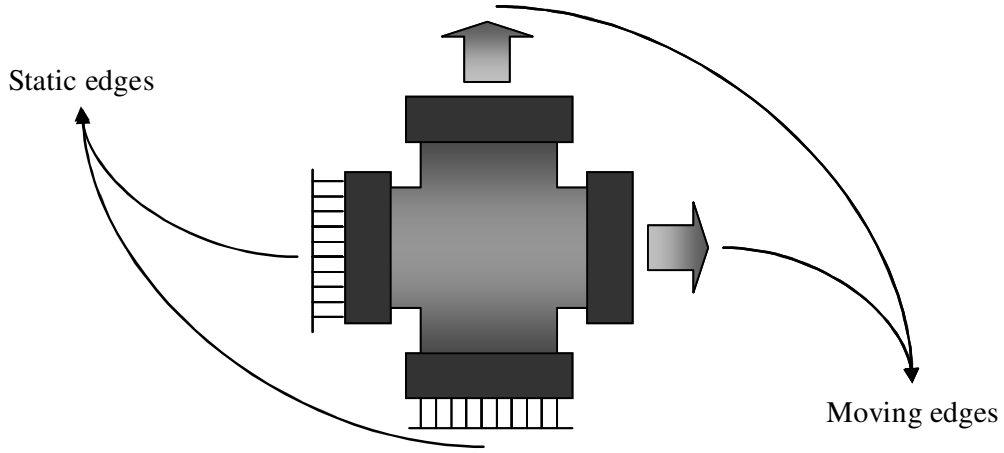

Figure 13. *Schematic of the biaxial device with two orthogonal edges kept static and two other orthogonal edges moved.*

In another approach, Doudard and coworkers have employed a biaxial deformation machine, shown in Figure 14, in order to study the fatigue behavior of metals under cyclic biaxial loading where the biaxial deformation was achieved using four motors moving in opposing directions so that the central region of the sample remains essentially static in space [94]. This device design, which was called ASTREE, is better suited for incorporation with scattering instrumentation. Although this particular group has used this device for studying metals, such a device could be employed to study the stress-strain behavior in addition to fatigue behavior of polymers as well. The design of ASTREE is quite useful to understand the effects of clays on the mechanical behavior

of polymers however, as seen from Figure 14, it is quite cumbersome and difficult to carry and ship, which is an important requirement for our in-situ experiments as different synchrotron facilities were to be used in the course of our work. The biggest problem with current designs is the bulkiness of these devices, making them impractical to fit into many sample environment areas of the x-ray spectrometers. In addition, bigger sample sizes, 15 x 15 cm^2, were used which results in using more materials for each test. Similar designs were employed by other researches to study stress-strain behavior of polymers and composites where sample sizes were reduced [79, 95, 96].

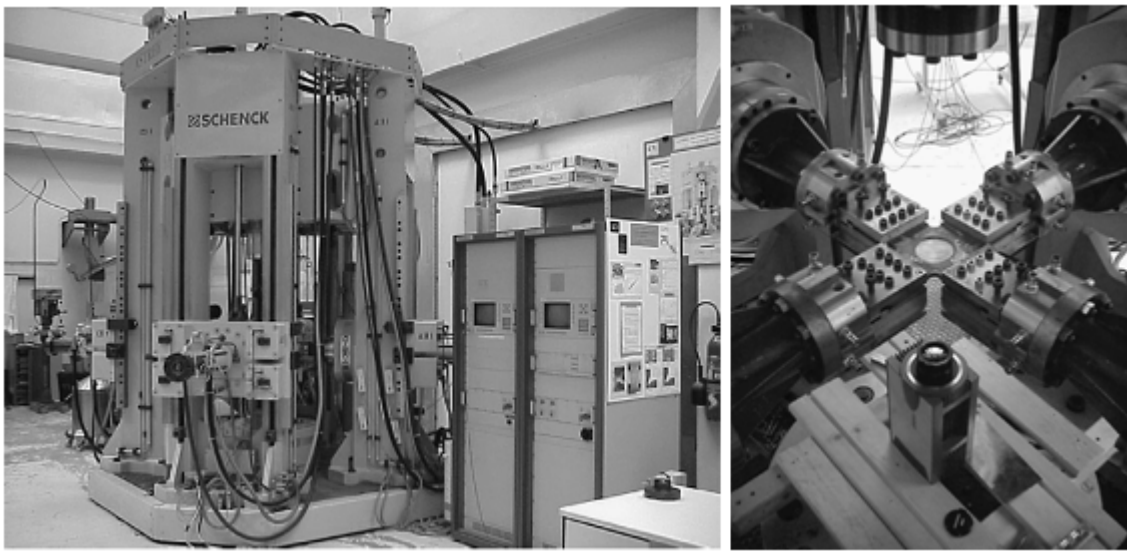

Figure 14 *a) Biaxial testing device, ASTREE and b) shape and mechanism of a deforming sample (Reproduced from [94]).*

A similar four motor approach was used by Martin et. al. [97] with some modifications where instead of a cruciform specimen a square shape specimen was used. In order to achieve uniform deformation along the whole specimen sample grips were modified so they extend laterally with strain as seen in Figure 15. However, similar issues

regarding the in-situ X-ray experiments are still a concern as this device is also cumbersome to carry and set-up with the available synchrotron beamlines. Another issue with these four motor devices is that they are set up to strain the films parallel to the X-ray beam, whereas the X-ray beam is supposed to travel perpendicular to the straining film.

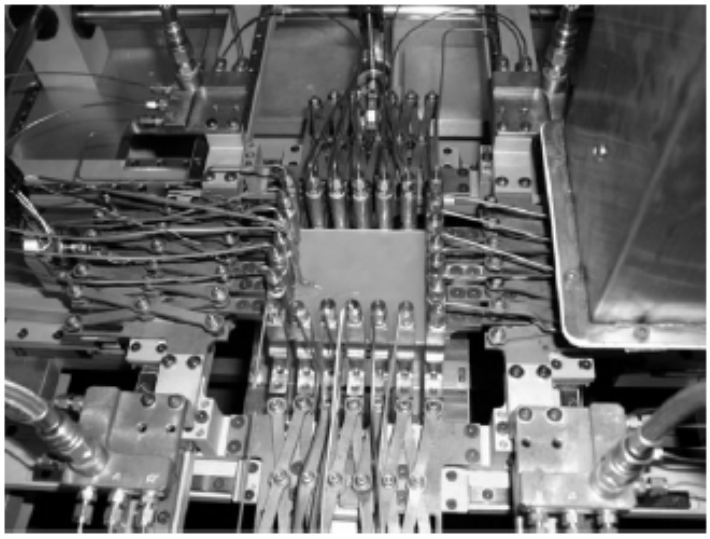

Figure 15. *Sample clamp mechanism for QUB flexible biaxial test rig (Reproduced from [97]).*

Another way of creating multiaxial/biaxial deformation is to blow a balloon out of a polymer film, a method which was described by Jeol et al. and BHR Group [98, 99]. In a related approach, it is also possible to create such multiaxial deformation by deforming the polymer using spherical or hemi-spherical shaped tools as shown in Figure 17 [78, 100].

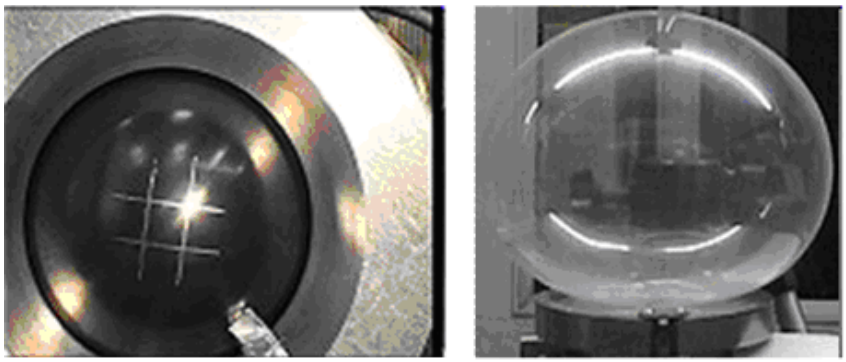

Figure 16. *Film blowing technique to create biaxial/multiaxial strain (Reproduced from [98])*

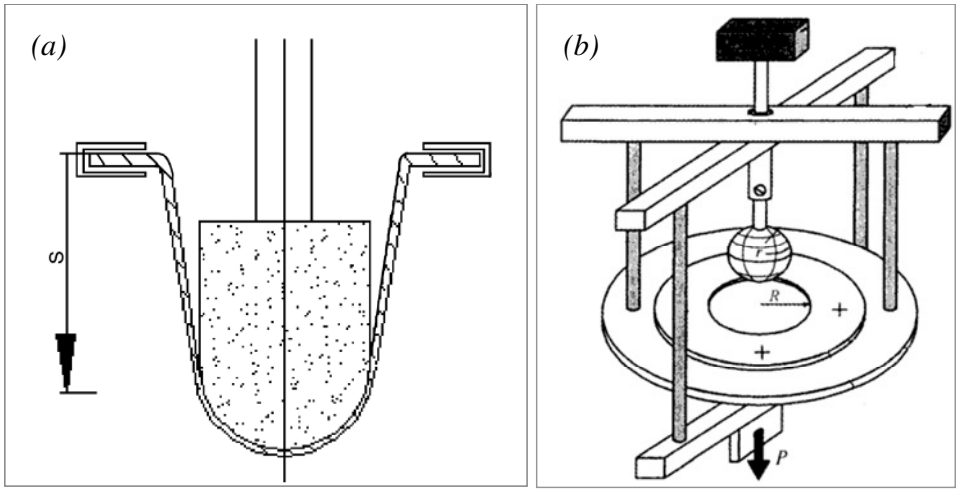

Figure 17. *Alternative ways of creating multiaxial deformation (a) by punching a hemi-spherical plug and (b) by punching a spherical plug. Figures reproduced from references [78] and, [100] respectively.*

Although both these approaches closely simulate the blow molding and thermoforming processes, they have some drawbacks when the x-ray experiments are considered. One of the constraints X-rays put on the device, in addition to observing the

same point on the sample, is that the sample to detector distance must be kept constant for calibration purposes. When a balloon is blown or the film is deformed using a shaped tool, the sample to detector distance constantly changes with increasing inflation/deformation (see Figure 16 and Figure 17) which than makes these kinds of designs unsuitable for in-situ tests.

Due to these constraints discussed above, it was necessary for a new and unique design in order to perform the in-situ scattering experiments.

3.2 Design of In-situ Multiaxial Deformation Device (IMDD)

Taking the constraints of fixed sample to detector position and measurement at the same point on the sample throughout the deformation process into consideration coupled with reduced physical dimension of the instrument, we have designed and built a multiaxial deformation device specifically for *in situ* measurements at SR X-ray WAXS/SAXS beamlines. A schematic and two pictures of the *in situ* multiaxial deformation device (IMDD) are shown in Figure 18.

Although all multiaxial deformation devices were considered during the design of the device, ultimately Jankauskaite and Hegemann [78, 100] were used as inspirations for the IMDD. The IMDD was designed specifically to mimic the blow molding and thermo-forming processes (shown in Figure 19), where polymer films are deformed multiaxially, while retaining a fixed sample to detector distance for the scattering measurements.

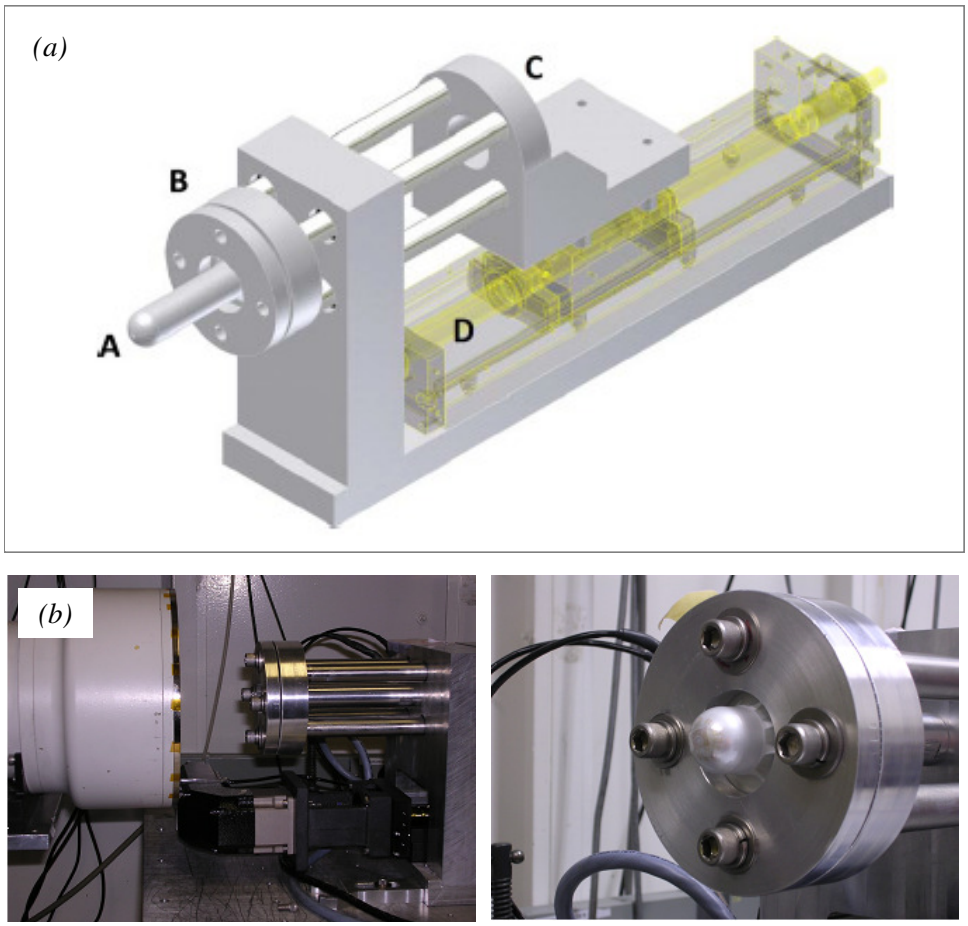

Figure 18. *(a) Schematic of the IMDD, showing the nose (A), translating sample clamp (B), translator and pull rods (C), and linear motor screw thread (D). The linear motor driving the screw thread is not shown, but is mounted at the front of the IMDD to reduce the foot print of the device, and (b) A picture of the device.*

The device has been designed to allow deformation studies even at room temperature (RT) where significant forces are required to deform the polymers. The device is made out of aluminum due to its strength-to-weight ratio, resistance to corrosion, ease of machining and relatively low X-ray absorption properties. The reduced weight makes the system portable and can therefore be easily installed and utilized on different SR beamlines.

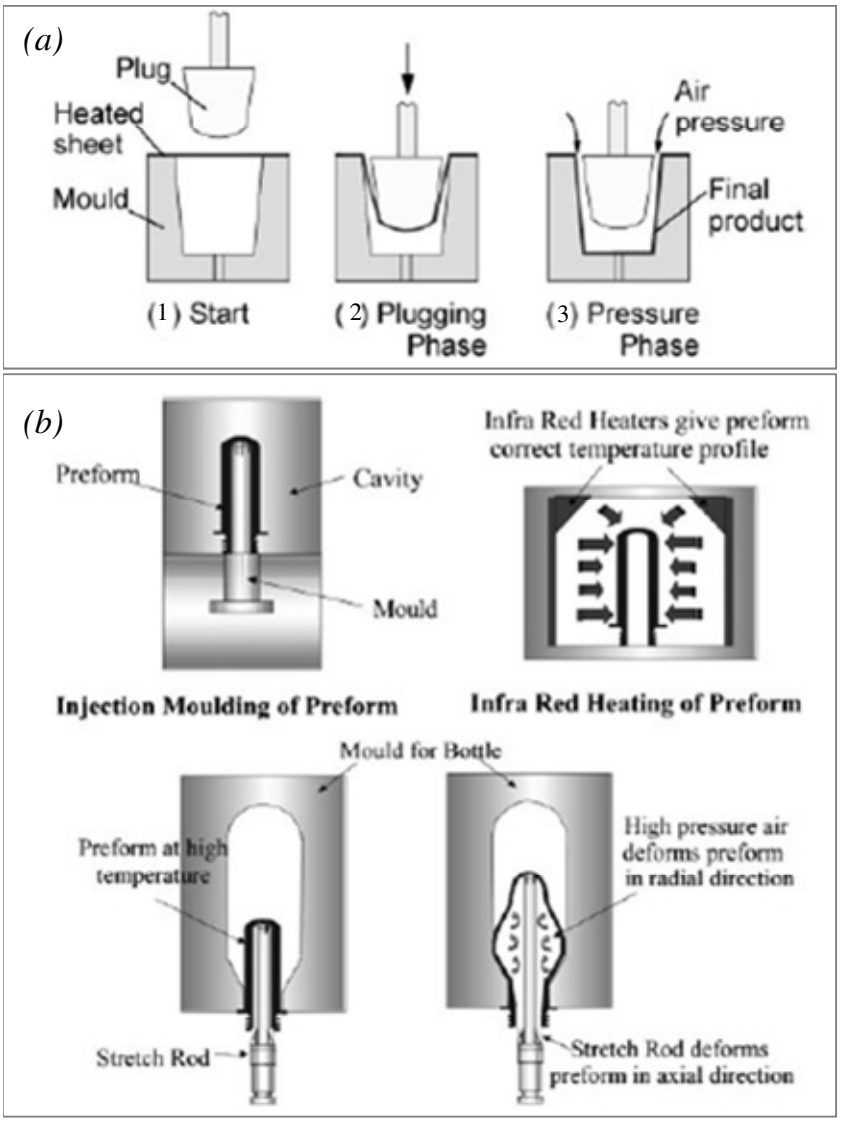

Figure 19. *Stages of deformation during (a) plug assisted thermo-forming and (b) injection blow-molding processes (Reproduced from [97]).*

The working principle of the device to create multiaxial deformation can be explained as follows: The polymer film is clamped between two retaining plates, which are mounted via extension rods and a translator block onto a linear motor stage. As the motor stage moves backward, the film is stretched around the fixed hemispherical shaped nose, generating a uniform multiaxial deformation zone at the center of the hemisphere.

In Figure 20, images of a polymer sample before and during deformation can be seen. In the figure on right hand side of the image (a) the out-of-focus object is the cone shaped aperture of the SAXS detector. The grid lines applied to the polymer film and used to determine strain are clearly observed. The dotted white vertical and horizontal lines on both images are digital overlays from the video to mark the center position of the nose.

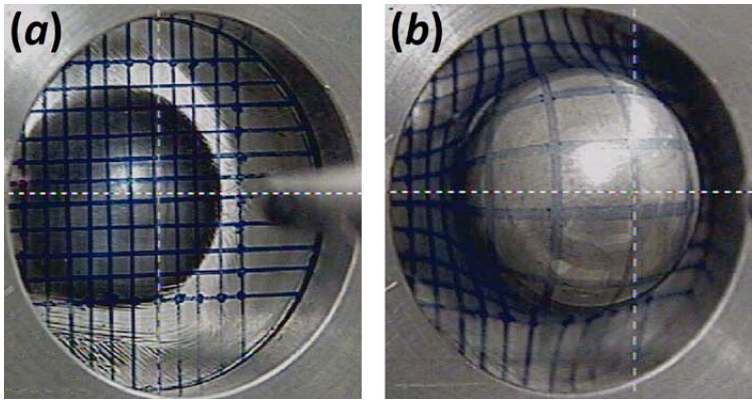

Figure 20. *Video images from a polymer sample (a) before and (b) during deformation. The images are taken from in front of the sample, looking toward the nose. (Actual size o the images 4X4 cm^2)*

The internal diameter of these sample retaining plates is 4 cm, which therefore allows the polymer to be deformed around the nose. The nose itself has an external diameter of 2.5 cm with a total length of 15 cm, allowing deformations of up to 500% to be achieved. The drive for the linear motor (Danaher Motions) that provides the strain, has a torque capacity of up to 53 Nm and a speed range of 1–600 rpm, equivalent to a strain rate range of 0.0005–0.3 s^{-1}. To quantify the strain applied to the sample we measure the deformation using video monitoring of the patterns drawn onto the sample. For all but the thin section at the hemispherical end of the nose, the rest of the nose and

its mounting block have been drilled out and are therefore hollow. The 3 mm hole allows the x-ray beam to pass through the IMDD to the polymer film relatively unimpeded.

Our initial design used a nose with a threaded hole travelling through the whole nose cone thereby allowing the X-rays to pass uninterrupted to the polymer. However this design was experienced to create non-uniform deformation at the tip of the nose cone, due to the effect of edges of the hole as described in Figure 21. Under such circumstance the polymer was deforming less where the X-ray analysis was performed. The deformation was being initiated at the edges of the X-ray passing hole which caused early failure of the polymer film.

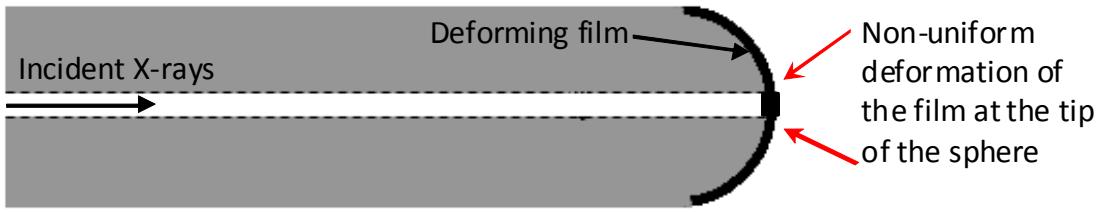

Figure 21. *Initial nose cone design with the X-ray travel path, threaded with a hole throughout the nose cone.*

One possible solution to the non-uniform deformation at the tip would be to use relatively X-ray transparent materials such as Kapton®, mica or beryllium as windows at the tip of the nose. However they were not thought to be sufficiently strong to withstand the stresses the device was designed for. In the ultimate design, the hemispherical end of the nose was bored out to leave approximately 0.5 mm thickness of aluminum at the tip of the nose. Although aluminum strongly absorbs low energy x-rays, the absorption is significantly reduced at higher energies that are only attainable at SR facilities.

Absorption and transmission percentages of Al at different energies with different thicknesses were calculated based on the x-ray mass attenuation coefficients tables provided by NIST. Based on a given energy level the transmission is calculated by [101]:

$$\frac{I}{I_0} = \exp[-\mu x] \tag{6}$$

where I_0 is the incident intensity, I is the transmitted intensity, x is the mass thickness obtained by multiplying thickness (t) with density (ρ), and μ is the attenuation coefficient of the material for a given energy level.

According to the calculations, for Al, at energies of for instance ~15 keV, the transmission remains acceptably high ~50% even at 500 μm thickness of aluminum (see Figure 22). By comparison, for Cu-anode sources used in a majority of lab-based x-ray instruments, the beam energy at 1.54 Å is 8.05 keV, so only at around 100 μm would the transmission be large enough to be acceptable for the *in situ* measurements described in this project even if the flux was sufficiently high. However, Al of only 100 μm thickness in the nose would not have sufficient mechanical resilience to withstand the forces being applied to some of the polymers. Therefore in the design of the nose we have compromised effective transmission with mechanical strength. To be able to utilize an Al thickness which can withstand the deformation stresses, we have adopted the use of a nose with an Al thickness of 0.5 mm at the nose tip. As mentioned above, these beam energies are only achievable via SR x-ray sources. Measurements of transmission through the Al window of the nose at 17 keV was found to be 44.3% from which the exact thickness of the Al was calculated using the incident and transmitted beam intensities and found to be 588μm.

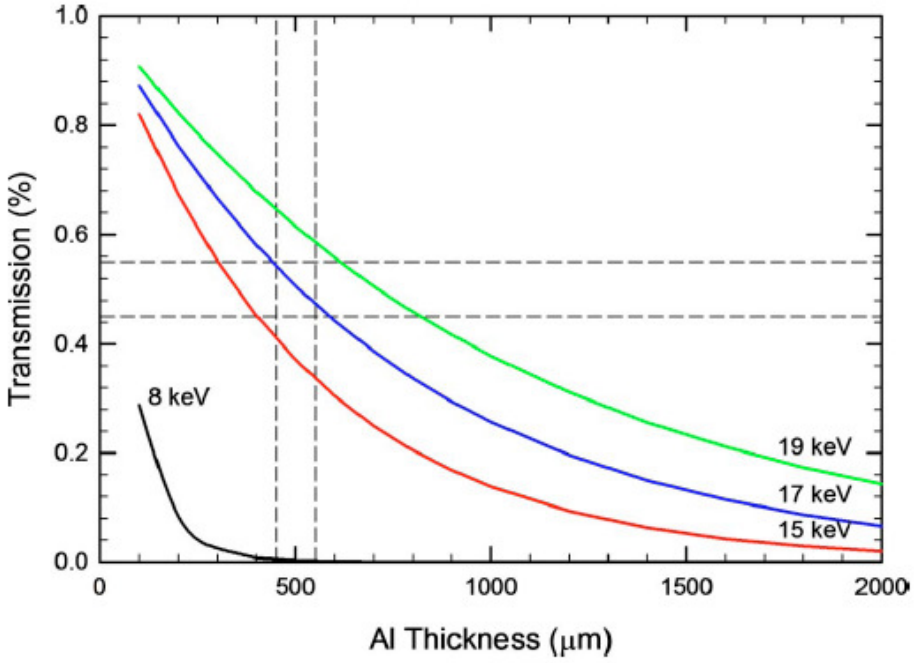

Figure 22. *Calculated X-ray transmission of aluminum as a function of its thickness for beam energies of 8, 15, 17, and 19 keV.*

During deformation the strain was measured using a grid applied to the undeformed sample. The grids were applied onto the surface of the polymer with a stamp and the lines on the stamp were separated typically by 1-2 mm. The actual distance between lines is largely irrelevant as long as the initial spacing for the undeformed sample can be measured with sufficient accuracy. Using digital video imaging taken concurrently with the deformation we were able to track the strain behavior as a function of time by measuring the variation in line separation. Measurements were made in multiple directions in order to check for any macroscopic anisotropy in the deformation and also to reduce the error in determining strain. The amount of deformation was quantified using the extension ratio, λ, which is defined by $\lambda = l_f / l_i$, where l_i and l_f are the initial and final grid separation lengths, respectively.

The IMDD linear drive motor that creates the sample deformation is controlled via a PC running commercially available software (Copley Motion Explorer (CME) 2, Copley Controls) [102]. This software allows the user to control the deformation via the system parameters, including the strain rate and target strain. The ultimate strain is determined by adjusting the number of rotations of the motor, which makes 1 full rotation per 16000 counts. Counts are the units that are input to the software. One rotation of the motor was calibrated to move the retaining plates, hence the clamped sample, 1 mm with respect to the fixed nose position. It was calculated from the changes in gridline spacing on the sample that 16000 counts corresponds to a stretch ratio of 0.115.

Similarly the strain rate is controlled by the rotation of the motor per minute (rpm). Two strain rate values were chosen in this work in order to study the effect of strain rate on the polymer morphology change during deformation. The upper limit for the strain rate was chosen to be 50 rpm, which was limited by the detectors' X-ray capturing rate. Strain rate at 50rpm was measured by video monitoring the deformation and calculated to be equal to $0.025s^{-1}$. A slower strain rate was chosen so that there was enough difference between the two strain rates and consequently there is the possibility of significant differences in the morphology changes. As a result, the slowest rate of 5 rpm was chosen. From the video imaging, this slower rate was determined to correspond to $0.0025s^{-1}$. In all cases the sample size was 65 x 65 mm^2. The samples were cut from the extruded sheets and used for multiaxial deformation, using a rotating saw.

3.2.1 Design of heating unit for higher temperature studies

High temperature studies are important to understand the behavior of the polymers under real processing conditions such as blow molding and thermo-forming. For this reason, a heating unit was also added to the IMDD to determine the temperature dependent evolution of morphology during multiaxial deformation.

However the design of the heating unit has same constraints with the device design that *in-situ* x-ray observations generate. The most important constraint is not to insert any additional windows or materials between the incident X-rays and the polymer or between the sample and the detectors. Additional materials may cause reduction in both the flux of the transmitted X-rays as well as the scattered X-rays, hence further complicate interpretation of the data obtained from the sample scattering. Secondly, it is also essential to prevent heating of the thermally sensitive detectors. Taking these constraints in to account a schematic of the final design for the heating unit which meets all the criteria is shown in Figure 23. The heating unit was to be mounted on top of IMDD and heating of the film was achieved through hot gas exhaust which was heated by passing through the insulated heating chamber and vectored onto the sample at the end of the nose cone. The heating unit allows in *situ* annealing of the sample via a specially built thermostatically controlled heater which vectors hot air onto the sample. In this approach only the polymer in the immediate area around the end of the nose is maintained at the preset temperature. A thermocouple close to, but not obscuring the scattering volume of the polymer was used to monitor the polymer temperature during the experiments.

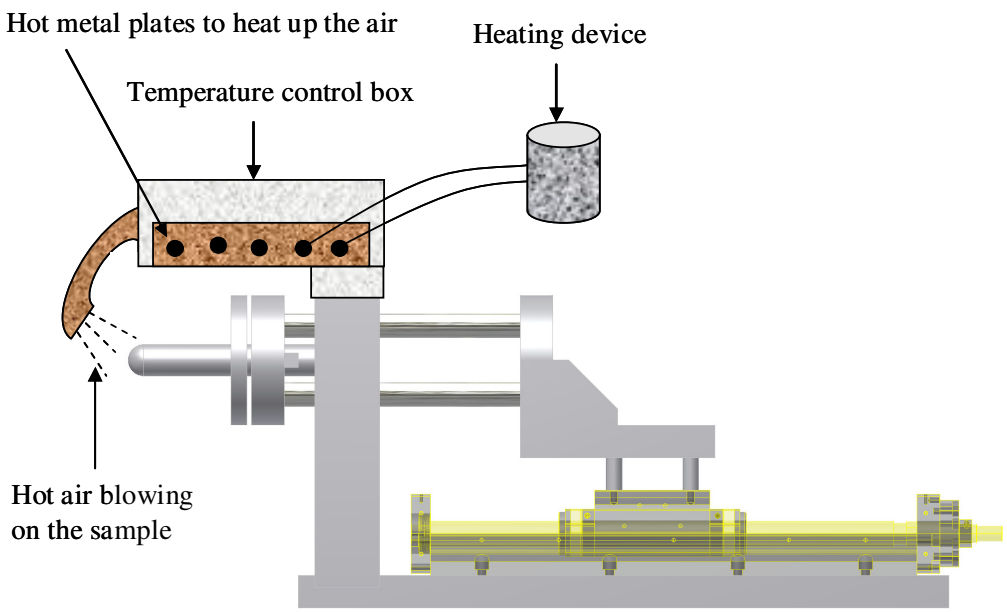

Figure 23. *Schematic of the heating unit.*

Another design, used for heating the sample, was a heating chamber covering the clamps, the sample, the nose and the extension rods. A copper block inside of the chamber attached to the walls of the chamber and the power supply was heated up to desired temperature while air circulation was achieved through hot air gun blowing in the chamber at the same desired temperature.

3.3 Design of the In-situ Biaxial Deformation Device (IBDD)

With the design of the IMDD, imitation of processing techniques such as blow molding and thermo-forming where the polymer films are deformed multiaxially is achieved. However, in other processing routes polymers undergo different strain paths such as film extrusion, biaxial deformation (simultaneous and sequential) rather than

multiaxial deformation is applied to the polymer. In order to understand such processing methods, and determine the processing route for a specific polymer and/or nanocomposite end-use, it is important to obtain an in depth knowledge of morphology evolution during all these processing conditions. With this in mind, we have designed an *in-situ* biaxial deformation device (IBDD) which allows *in-situ* uniaxial deformations as well as simultaneous and sequential biaxial deformations. Picture of the IBDD are shown below in Figure 24 where the front view shows the position of the heating unit and the sample; and top view shows the wires that are attached to the sample holders and then the linear motor stage through the pulleys.

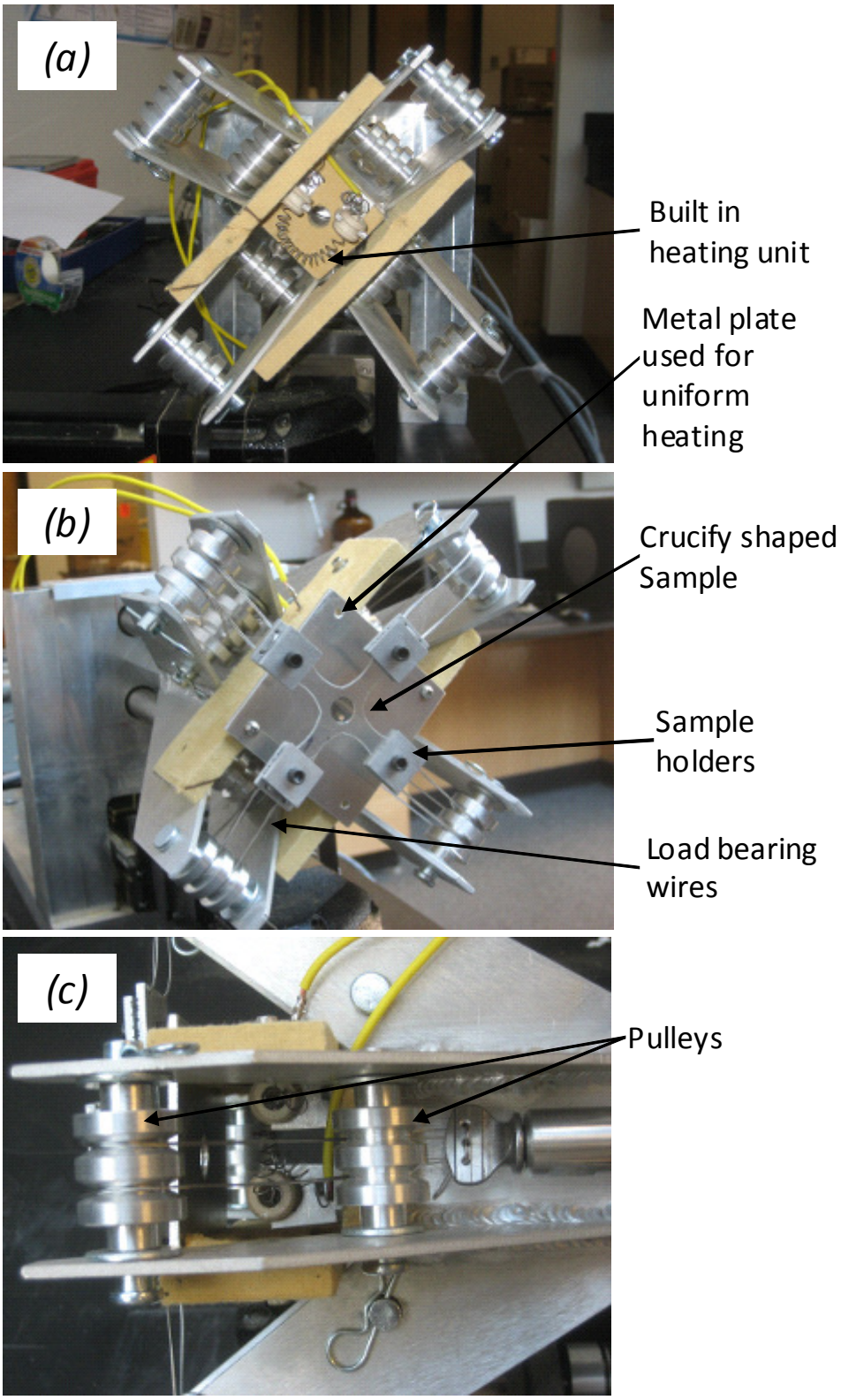

Figure 24. *Picrures of IBDD (a) Front view without sample, (b) front view with sample and (c) top view.*

This design is basically a development to our existing IMDD, where the clamping plates and the nose cone are replaced with pulleys, sample clamps and wires which transfer linear motion from the motor to biaxial deformation. When the motor stage is moved backwards, wires travelling through the pulleys and holding the sample clamps stretch the cruciform specimen biaxially. With this design it is possible to perform sequential biaxial drawing to create initial orientation in the sample to study the effects of orientation on the processing performance of polymers and nanocomposites.

A built in heating unit allows deformations at high temperatures up to 150°C. Heating of the polymer film is achieved through a resistive steel wire which is connected to a variable voltage power supply. By adjusting the voltage it is possible to heat the polymer films up to different temperatures between RT and 150°C. An Al plate placed between the heating wires and the specimen is used to obtain uniform heating of the sample. A hole drilled through the Al plate allows the passage of the X-rays unperturbed.

An important issue for a successful biaxial test is the design of the specimen itself. An optimized design for a cruciform shaped specimen which will go through biaxial deformation should fulfill the following requirements [103-105] :

(i) It should maximize the uniform strain region at the biaxially loaded zone.

(ii) It should minimize the shear strains in the biaxially loaded zone.

(iii) It should minimize the strain concentration and failure outside the test zone of interest.

(iv) Specimen should fail in the zone of interest.

(v) The tests should be repeatable.

It is difficult to overcome all the listed requirements above with a simple design of a cruciform shaped specimen. Therefore, Makris and coworkers performed numerical simulations considering the above mentioned constraints to obtain an optimized cruciform shape for the specimen which will undergo biaxial loading [106]. In their work they have used Finite Element Analysis tools to obtain the optimum geometry with optimum curvatures which will provide uniform biaxial deformation. The shape of the dog-bone sample they developed can be seen in Figure 25 (*a*). In Figure 25 (*b*) a picture of our sample that is optimized for IBDD is shown. Optimization was done by increasing the sizes of the sample at the edges of the dog-bone shape to create additional area for a better sample clamping. The dog-bone shape samples were drawn using AutoCAD software and cut by feeding the AutoCAD images to the water jet.

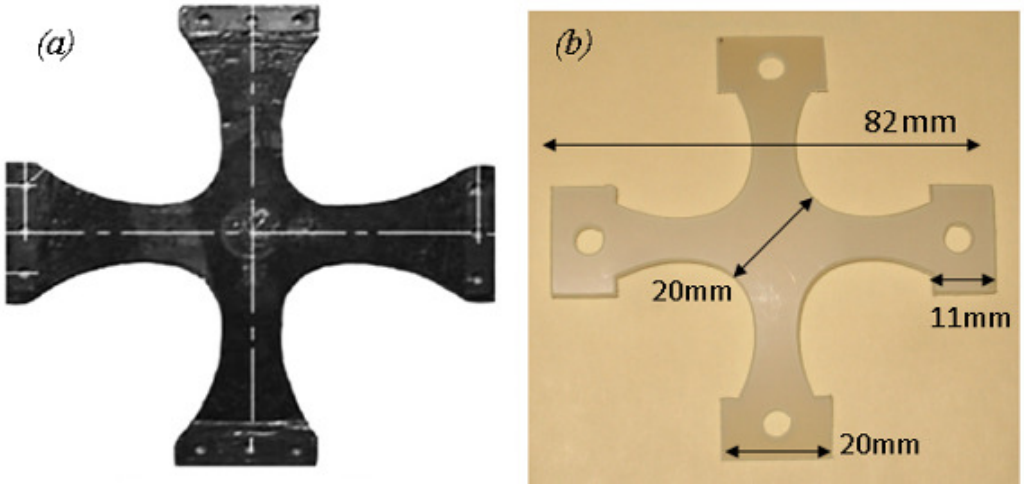

Figure 25. *(a) The shape of the specimen proposed by Markis et. al. and (b) the modified shape of the specimen for IBDD with longer arms allowing better sample clamping, with dimensions.*

CHAPTER IV

MATERIALS, METHODS AND TECHNIQUES

4.1 Materials and Sample Preparation

All the neat polymers and the polymer/clay nanocomposites used in this project were provided by our collaborators from Queen's University Belfast, School of Mechanical & Aerospace Engineering, Northern Ireland, UK. Specific material processing data is explained below:

The HDPE was purchased from Total Petrochemicals, Europe and has a melt flow index (MFI) of 0.2g/10min (at 190°C/2.16kg) and density of 0.954g/cm^3, The PP was also purchased from Total Petrochemicals, Europe has a MFI of 6g/10min (at 230°C/2.16kg) and density of 0.905g/cm^3. Fusabond compatibilizer with MFI of 46g/10min (at 190°C/1kg) was purchased form Dupont. The clay used in all the nanocomposites is Cloisite® 15A, purchased form Southern Clay Products.

Initially the PP or PE granules and Fusabond compatibilizer were ground into a powder. For PP nanocomposites 3 wt% Fusabond was added, while 6wt% compatibilizer was added to PE. The clay powder was dried at 100°C overnight. For each nanocomposite the required amount of clay and polymer-Fusabond powder were melt extruded into sheet form using a Kolin ZK25 single screw extruder with a 30:1 length-to-diameter (L/D) ratio and with a screw diameter of 25 mm. The die temperature was kept at 205°C with a die gap of 1.2mm. The extruded sheet was cooled on a pair of chilled rolls rotating at 1 m/min at 70°C for the PP nanocomposite and 60 °C for PE.

For future references neat HDPE with compatibilizer will be referred as PE while 3 and 6 wt% clay added HDPE-compatibilizer will be referred as PENC3 and PENC6, respectively. Similarly for PP; the neat PP mixed with compatibilizer will be referred as PP; while 1, 2, 5 and 10 wt% clay loaded PP-compatibilizer will be referred as PPNC1, PPNC2, PPNC5 and PPNC10 respectively. Table 5 summarizes the details of the abbreviations used for each material.

Table 5. *Details to the material abbreviations.*

Material Abbreviation	Polymer	wt% Compatibilizer	Wt% Clay
PE	HDPE	6	0
PENC3	HDPE	6	3
PENC6	HDPE	6	6
PP	PP	3	0
PPNC1	PP	3	1
PPNC2	PP	3	2
PPNC5	PP	3	5
PPNC10	PP	3	10

4.2 Thermal Analysis

Thermal properties of all materials including the melting temperature and the amount of crystallinity were determined by Differential Scanning Calorimetry (DSC) analysis. DSC experiments were performed on a TA instruments Q200 instrument under a nitrogen atmosphere using 10-11 mg of sample in the standard aluminum DSC pans. Each sample was rapidly cooled to -80°C, and heated to 220°C with a heating rate of

10°C/min. Three separate runs for each sample were performed and the results were averaged. The percentage crystallinity was calculated from the specific heat of fusion by taking the value for a fully crystalline PE to be 293 J/g and for a fully crystalline PP to be 192.6 J/g [107, 108].

4.3 Melt Rheology Experiments

Melt rheology measurements were obtained from a 25mm parallel plate, TA instruments AR-2000ex model rheometer operated at 180°C, ~20°C higher than T_m of PP and PPNCs to ensure fully melting of PP crystals under atmospheric conditions.

4.4 Laboratory Based X-ray Measurements

Wide angle X-ray scattering measurements were performed on a Rigaku Micro Max 002 X-ray generator operated at 45 kV and 0.66 mA and equipped with R-axis VI++ detector. For X-ray studies, powder samples were measured in 1 mm diameter capillaries from Hamilton Research with a wall thickness of 0.01 mm and scattering was collected over 30min in order to get the best signal to noise data. Scattering from film shaped samples were collected for 5 min and corrected with respect to film thicknesses. Scattering from empty capillary and air were also collected for an equal amount of time to the samples to correct for background. AreaMax software from Rigaku Americas Corporation was used for background subtraction and integration.

4.5 In-situ X-Ray Studies

Due to the portability of the IMDD, *in situ* WAXS and SAXS experiments described here have been performed at both the DND-CAT beamline 5ID-D at the Advanced Photon Source (APS; Argonne National Laboratory, Illinois, USA) [109], as well as the I22 beamline at the Diamond Light Source (DLS, U.K.) [110]. For the reasons described above, the beamlines were tuned to operate at a beam energy of 17 keV, giving a wavelength of 0.73 Å. The beam at the sample position for both instruments was controlled via slits to have dimensions of a few hundred microns; for instance, the beam at APS was 220x220 μm^2 and 320x320 μm^2 at DLS. In all cases, the WAXS and SAXS patterns have been measured simultaneously using two separate detectors. More details on the specifics of the beamlines can be found elsewhere [109, 110].

Measurement times were determined based on signal-to-noise ratio in the data and are a function of the flux of the X-ray beam at the different facilities. In most of the measurements we undertook at APS a data capture rate of 0.1s per frame was used, while at Diamond with a slightly lower flux data capture rates were 1s per frame. The strain rate of the measurements was limited with respect to the frame capture rate to avoid smearing of the data from very different regions in the strain curve. The WAXS detector is mounted closest to the sample position (approximately 300 mm) with the SAXS detector a few meters (approximately 6 m) further back. The precise length of the SAXS and WAXS sample-detector distances at the different beam lines were determined by considering for each detector the scattering vector (q) range of relevance that we wished to measure over. In order to obtain a wider q range *in-situ* multiaxial deformation experiments were repeated using a different sample-to-detector distance with the SAXS

detector. In which case, the SAXS detector was moved closer to the sample allowing the capture of the medium q range data in medium angle X-ray scattering (MAXS). Precise determination of the sample-to-detector distance as well as CCD pixel position to q, calibration of the SAXS, MAXS and WAXS data were achieved by measuring collagen, silver behenete (AgBe) and silicon powder, respectively, as calibrants. A sample of wet rat tail collagen is often used to calibrate the SAXS detector for lower q measurements while AgBe is used for medium q measurements; and silicon powder is used to calibrate the WAXS detector. The scattering patterns obtained from the calibrants were in the form of "Intensity versus pixel units". The SAXS patterns of collagen shows equidistant peaks with a primary spacing of around 67 nm, while the average crystallite size along the long-spacing direction of AgBe is 58.38 nm. The WAXS pattern of silicon powder has three distinct crystal peaks at d=3.138, d=1.92 and d=1.638 nm. A simple linear relationship was calculated based on the well-known crystallography of the calibrants to convert the pixels into reciprocal nanometers. In Figure 26 1D diffraction patterns for the standard calibrants can be seen. Combined SAXS, MAXS and WAXS plots of Cloisite® 15A clay is shown in Figure 27 as an indication of the total q range, hence size range, covered in the *in-situ* experiments.

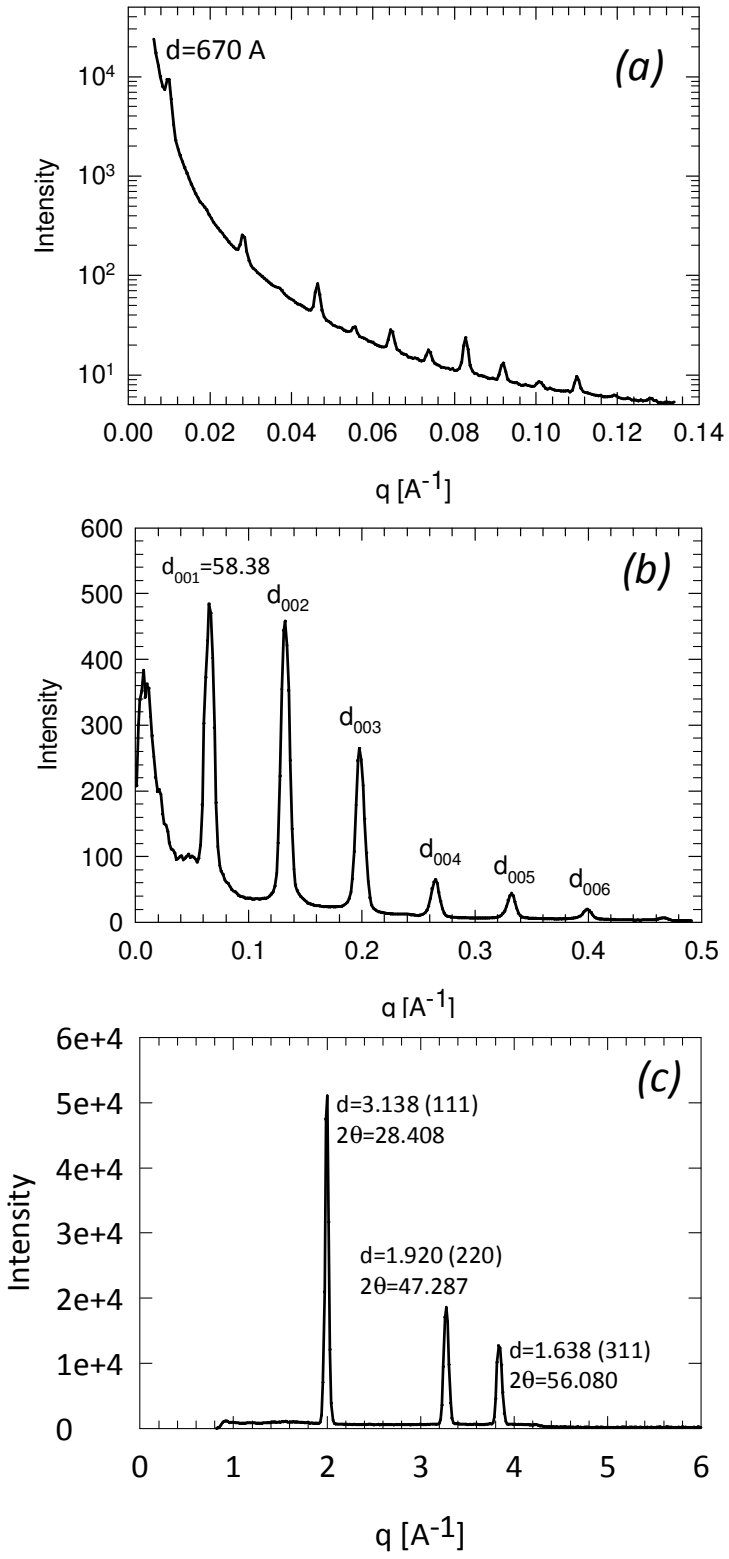

Figure 26. *1D Intensity vs. q graphs for standard calibrants (a) collagen, (b) silver behenate and (c) silicon powder.*

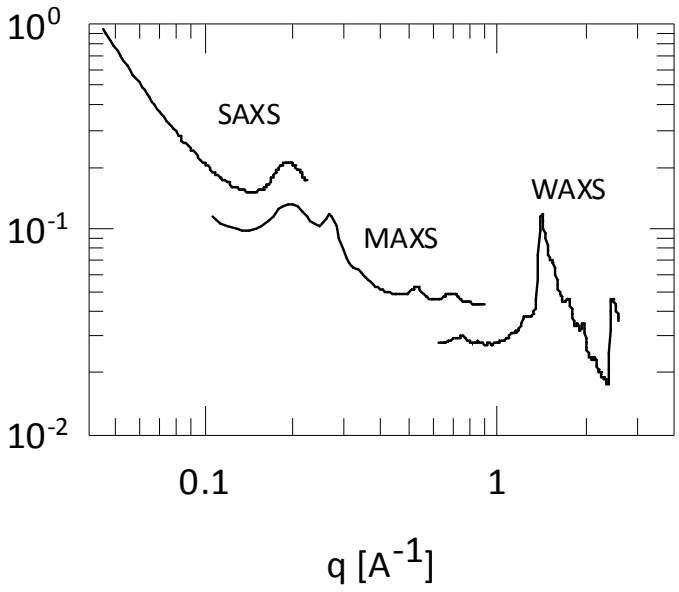

Figure 27. *Combined SAXS, MAXS and WAXS scattering from Cloisite® 15A*

The total scattering from the sample measured *in situ* is a combination of the polymer scattering plus that from the Al nose. Therefore, the scattering from the Al nose was measured in both SAXS, MAXS and WAXS regions and these data were subtracted from the total scattering data after correcting for differences in measurement times. Correction with respect to the decreasing sample thickness was also considered and the scattering collected at different times of sample deformation were normalized with respect to the initial sample thicknesses.

The intensity of scattering in the SAXS regime measured from the Al decreases monotonically with increasing q. The Al background subtraction does make a slight difference to the scattering in the low q regime (see Figure 28), but does not affect the general scattering behavior from the polymer.

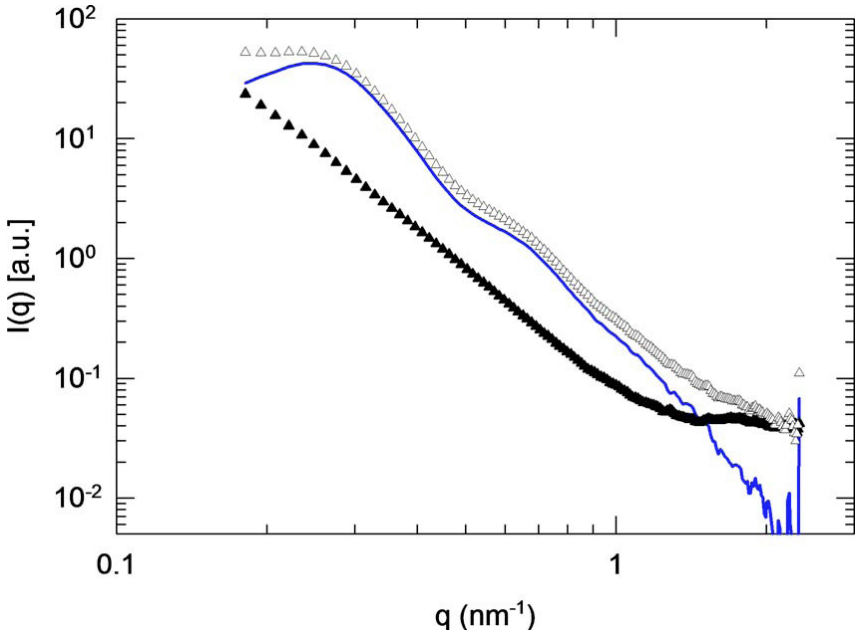

Figure 28. *Typical radially averaged 1D SAXS pattern for the total scattering for the undeformed PE sample plus the Al nose (Δ), only the Al nose (▲), and PE scattering with that of the Al subtracted (blue line).*

In the WAXS regime the Al has a number of characteristic peaks, the most intense of which occur at q values ~20 nm^{-1}. However, when measuring the total scattering from the deforming PE samples, these comparatively weak Al peaks are only detected in the polymer samples which are highly deformed and have consequently substantially thinned. In these cases, the subtraction of the Al WAXS pattern becomes important to distinguish the polymer diffraction from that of the Al. In all other cases where the Al peaks are by comparison very weak, the Al only contributes to the background and does not affect the polymers' WAXS scattering.

Due to the configuration of the instrument, isotropic (equiaxial) deformation was observed in all samples, except in a few cases where local failure caused anisotropic deformation. In these instances, data analysis can be undertaken following the approaches

exploited widely for uniaxial deformation of polymers. However since these anisotropic events were uncontrolled, we could not quantify these data, but rather we used the observation of anisotropy in the scattering to determine those samples where premature failure occurred. For the samples majority of the samples which deformed isotropically, our measurements showed that, as expected, the same strain was achieved for a given translational motor displacement as long as the same thickness of film was used, as was the case for our samples. The video camera for these measurements was fitted with telescopic lens and was placed off-axis, thereby avoiding the possibility of parasitic x-ray scattering. Video images from a typical *in situ* deformation experiment were shown in Figure 20.

Data was obtained in both .tiff and .chi format at APS and in .dat format in DLS. Data processing, including background subtraction, obtaining azimuthal intensity profiles and radial averaging of the data, was performed using *Fit2D* and *Dream* softwares available from European Synchrotron Radiation Facility [111] (ESRF) and Diamond Light source [110], respectively.

4.6 Ex-situ Biaxial and Tensile Mechanical Measurements

Mechanical characterization of the PE, PP and the nanocomposites were performed on Insight 2 tensile tester at room temperature at a strain rate of 5mm/min. Correlation of the strains to the force applied were achieved by comparison to *ex situ* measurements using exactly the same sample configuration in an adapted mechanical test instrument (Insight 2), where the standard sample grips were replaced with the circular clamping unit and nose from the in situ device (see Figure 29).

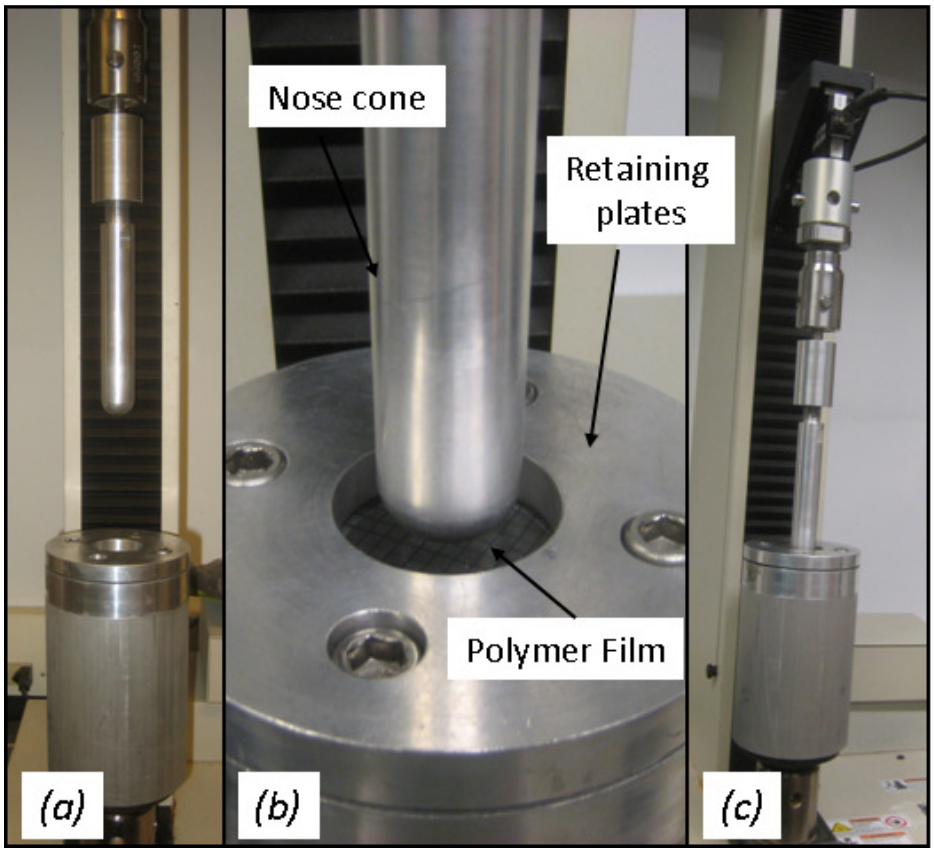

Figure 29. *Ex-situ multiaxial deformation set-up (a) before deformation, (b) during initial contact of nose cone with polymer film and (c) during deformation.*

The load was recorded as the samples were deformed by translating the nose to push against the clamped sample with the same displacement rates as in the *in situ* experiments. A typical load-extension ratio curve for this multiaxial deformation process is shown in Figure 30.

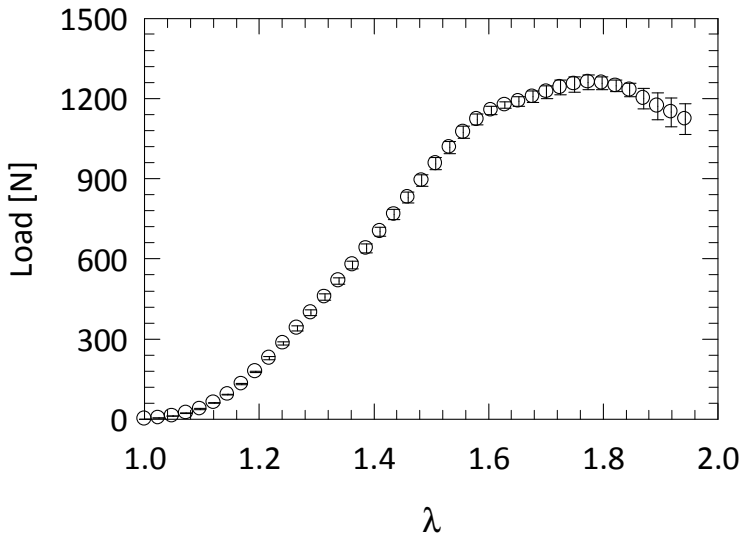

Figure 30. *Representative multiaxial load-strain curve for PE obtained ex situ using Insight 2 mechanical test instrument with the same geometry and strain rates as the in situ scattering experiments.*

From these types of stress-strain curves, we can estimate the applied load for any strain applied during the *in situ X*-ray deformation measurements determined from the video capture measurements. Although the load was measured indirectly in this fashion, we estimate that the error in this method of determining strain and stress is of order 5–10 %, and well within the accuracy for typical mechanical measurements of polymers. The load-strain data were collected at the same strain rates and temperature environments as those used in the *in-situ* measurements.

CHAPTER V

RESULTS AND DISCUSSIONS ON PE AND PE/CLAY NANOCOMPOSITES

This chapter describes the results from in-situ multiaxial deformation studies of PE and PENCs. Additionally it includes mechanical and thermal characterizations of PE and PENCs as well as ex-situ uniaxial observations and the effects of time dependent recovery on the polymer morphology. The effects of strain, strain rate and temperature on the polymer morphology changes in addition to these produced by the presence of the clays are discussed.

5.1 Mechanical Properties

As described earlier the materials used in this dissertation work were prepared by our collaborators from Queens University Belfast (QUB). In order to gain better knowledge about the material properties, thermal and mechanical analysis on the materials were performed and results are summarized in Table 6. Earlier studies performed on PE clay nanocomposites reported that there is a significant increase in mechanical properties of PE with the addition of clays and especially with increasing clay content [112, 113]. Consistent with the earlier reports, the mechanical properties of PE was observed to improve with the addition of 3 and 6 wt% clay for the case of our materials.

An increase of 6 and 22% in the elastic modulus of PE was observed with the addition of 3 and 6 wt% clay, respectively. Although a decrease of the yield point of

PENCs during uniaxial loading was detected, the overall toughness of the nanocomposites was significantly higher compared to the neat polymer. The increase in the toughness of PE was reported before with the addition of clays [114] and believed to originate from the strong interaction between the clays and the polymer. The shearing of clay layers with respect to each other during deformation hence absorbing additional energy was suggested as the form of deformation which increased the strain at failure. Table 6 summarizes the uniaxial mechanical properties of PE and PENCs.

Table 6. *Tensile mechanical properties of PE and PENCs.*

Materials	E **[GPa]**	ε_y **[%]**	ε_b **[%]**
PE	8.99±0.95	16.34±2.15	585±11
PENC3	9.52±0.75	7.08±0.53	710±14
PENC6	11.00±0.55	6.47±0.8	795±16

Figure 31 shows representative multiaxial deformation data of PE and PENCs while Table 7 summarizes the multiaxial deformation test results. Under multiaxial deformation yield point of PE was observed to remain almost unchanged with the addition of clays. This observation is different from what we have seen during uniaxial tests. On the other hand the toughness of PE was observed to improve with the addition of clays similar to uniaxial deformation behavior. The reason for the improved toughness is believed to originate form the strong interaction of clays with the polymer and as a consequence contributing to the toughness of polymer by shearing as explained earlier. In addition the particle-induced cavitation formation process is suggested to release plastic

constraints and encouraged plastic deformation of the matrix [115]. This improvement effect on the toughness however was observed to decrease when the amount of clays in PE reached 6 wt %. This is probably caused by the reduced clay-polymer interactions and increased clay-clay interactions due to the increased amount of clays in the polymer which reduced the effect of clays load bearing capacity. Due to the unique nature of the multiaxial tests, it is not possible to make comparisons with other reports. However the different behavior of PE with the addition of clays under multiaxial deformation compared to the uniaxial deformation underscores the importance of studying such nanocomposites under more complex deformations to understand what is happening during processing conditions.

The maximum values of stretch ratios attained were higher when the deformations were performed ex-situ compared to the in-situ values. This could be a result of pushing the nose cone through the retained film instead of the other way around, which is the case during *in-situ* experiments. For comparison purposes in the in-situ X-ray measurements a constant stretch ratio was picked for the neat polymer and the nanocomposites. The maximum stretch ratio measured at room temperature for these samples during *in-situ* X-ray measurements was 1.38, and 1.56 at 55°C.

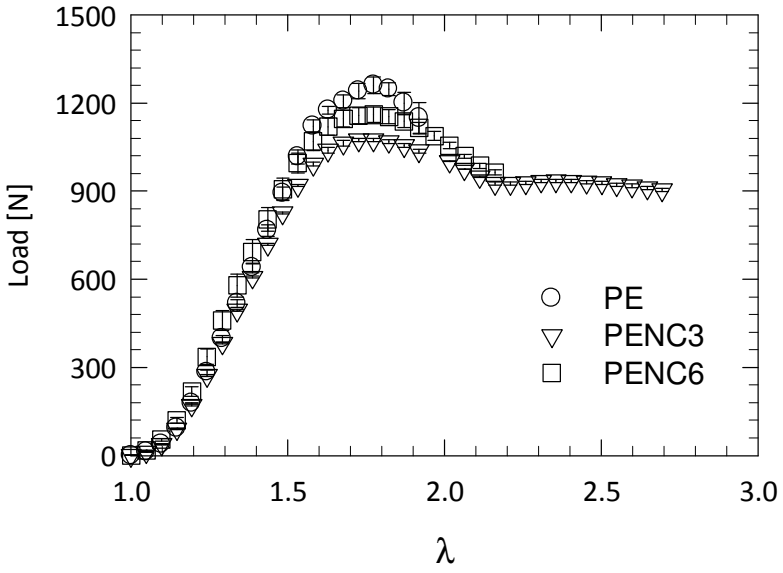

Figure 31. *Average load vs. stretch ratio curves obtained at RT at 0.0025s^{-1} strain rate.*

Table 7. *Yield stretch ratio, λ^{*}, and break point stretch ratio, λ^{**}, for PE and PENCs under multiaxial deformation at two different strain rates at room temperature.*

Material	**0.0025s^{-1}**		**0.025s^{-1}**	
	λ*	**λ****	**λ***	**λ****
PE	1.78±0.07	1.91±0.2	1.46±0.1	1.57±0.21
PENC3	1.74±0.02	2.69±0.13	1.51±0.02	1.94±0.27
PENC6	1.76±0.04	2.16±0.15	1.53±0.03	1.78±0.29

5.2 Thermal Properties

Table 8 summarizes the thermal properties of PE and PENCs. In the literature thermal properties of PE was observed to change slightly with the addition of clays where with a small decrease in both the melting point (T_m) and the overall crystallinity (X_c) of the polymer [114]. In the case of our materials, by comparison, there were no significant

difference, within the experimental error, observed between the neat polymer and the nanocomposites of T_m or X_c. Such observations were also reported before [116] in the literature and explained by the degree of exfoliation of clays in the PE matrix. If a well exfoliation degree is achieved thermal properties were observed to remain relatively unchanged [116]. However other researchers report a different observation suggesting the increased clay exfoliation slightly decrease the crystallinity due to the higher interfacial area and adhesion between the PE matrix and exfoliated clay, which than acts to reduce the degree of freedom of the crystallizable chain segments [113]. The fact that there are controversial reports on the thermal properties of PE nanocomposites suggests that there is still more work required to be done on the fundamental understanding of crystallization behavior of polymer/clay nanocomposites. On the other hand the unaltered thermal properties of PE with the addition of clays there is a good sign in terms of the processibility of the nanocomposites as that is required no change in the processing temperature window of PE with the addition of clays.

Table 8. *Thermal properties of PE and PENCs.*

Materials	T_m [℃]	X_c [%]
PE	117.6±3.5	68.2±2.0
PENC3	118.1±3.7	70.6±2.7
PENC6	117.9±3.9	68.6±2.1

5.3 General in-situ X-ray Observations

A typical example of evolutions of 2D SAXS and WAXS patterns during multiaxial deformation, for PE and PENCs at RT, at a strain rate of 0.0025 s^{-1}, are shown in Figure 32. The 2D SAXS patterns for the as made samples are anisotropic due to the preferred orientation in the samples resulting from the sheet extrusion process used in the sample preparation. Unlike the scattering behavior observed during uniaxial deformation of PE where the 2D scattering patterns become increasingly more anisotropic with increasing strain [11, 72, 83], the SAXS patterns obtained from multiaxially deformed PE and PENCs become increasingly more isotropic. The loss in the anisotropy is as observed more easily from the nanocomposites proportional with increasing clay in PE in the SAXS data. In the WAXS data of PE and PENCs on the other hand, we observe the growth of an additional crystal ring in the expense of the already existing crystal rings.

In Figure 33 azimuthal scans of the peak at q=0.24nm^{-1} is shown for PE and PENCs with the azimuthal angle indicated in the inset of Figure 32. Any changes in the peak intensity can be used as an indication of changes in orientation such as a stronger peak indicates a better ordering while a weaker peak indicated reduction in the orientation of the lamellae. In order to evaluate the decrease in the preferential ordering, the decreases in the peak intensity values were calculated for PE and PENCs. A drop in the peak intensity of azimuthal profiles of 26, 38 and 46 % for PE, PENC3 and PENC6, respectively, was found. This suggests that the clays contribute to the change on the anisotropy of the polymer by changing orientation in the plane strain direction. Similar decreases in the azimuthal intensities in the WAXS region was observed with increasing strain towards becoming more isotropic. Figure 34 shows azimuthal scans of the WAXS

(110) orthorhombic peak with increasing deformation for PE and PENCs. A better preferred orientation was observed in the as made samples of PENCs compared to PE, which is believed to originate from the contribution of clays to the orientation of polymer crystallites origination from the film extrusion process.

The scattering patterns for these multiaxial deformation conditions were observed to revert back to their original oriented state once the imposed stress was fully removed and the sample was allowed to relax. This time dependent recovery could well result from the fact that the achieved strain levels were lower than the yield points of PE and PENCs under multiaxial deformations. The rates of the time dependent recovery were however, dependent on the clay content in the system and the temperature. This recovery in the morphology underscores the importance of *in-situ* scattering, as opposed to *ex-situ* measurements of the sample before and after deformation where the transient nature of the structure is not observed.

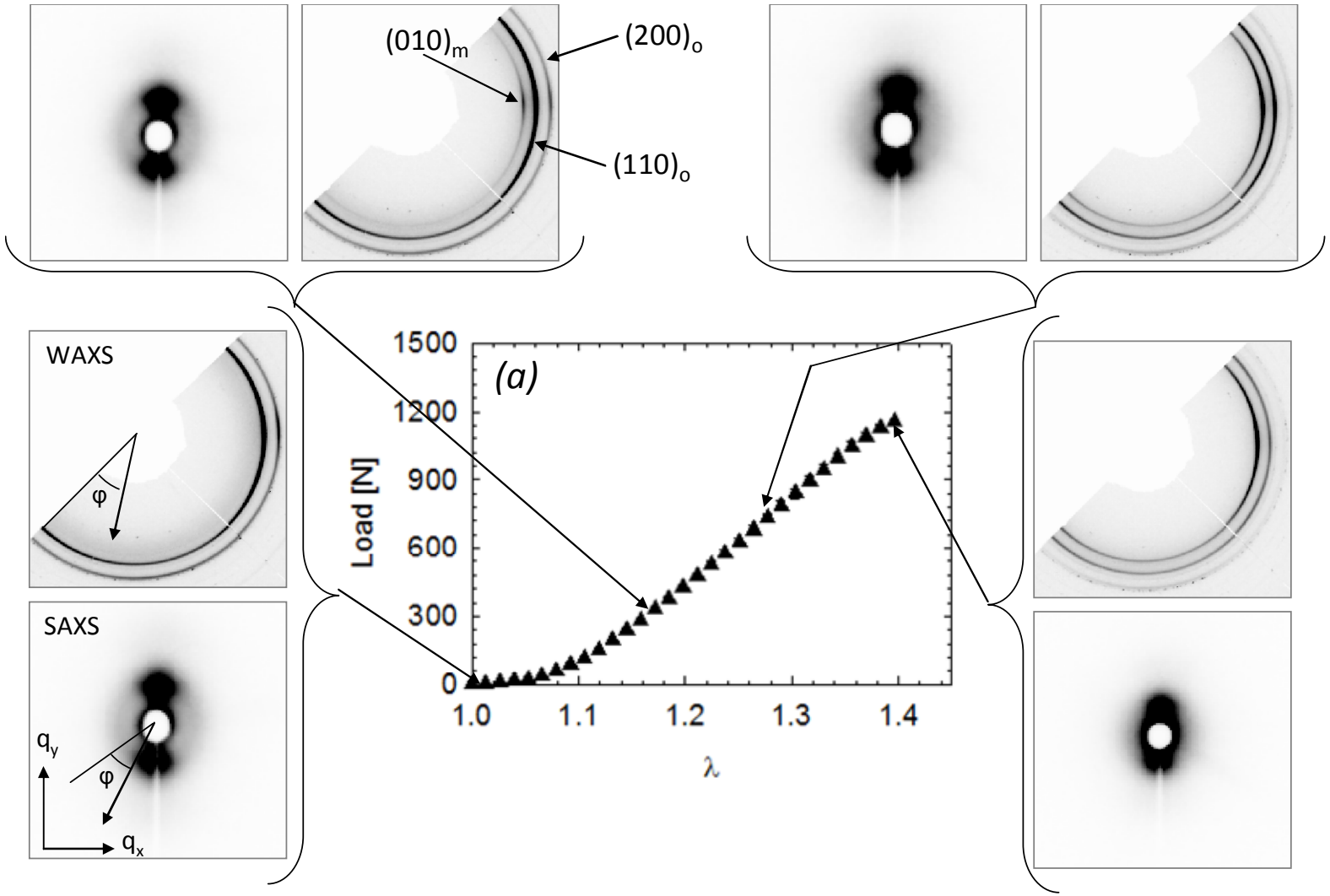

Figure 32. *2D in-situ collected SAXS/WAXS patterns with ex-situ collected Load vs. λ curves for (a) PE, (b) PENC3, and (c) PENC6*

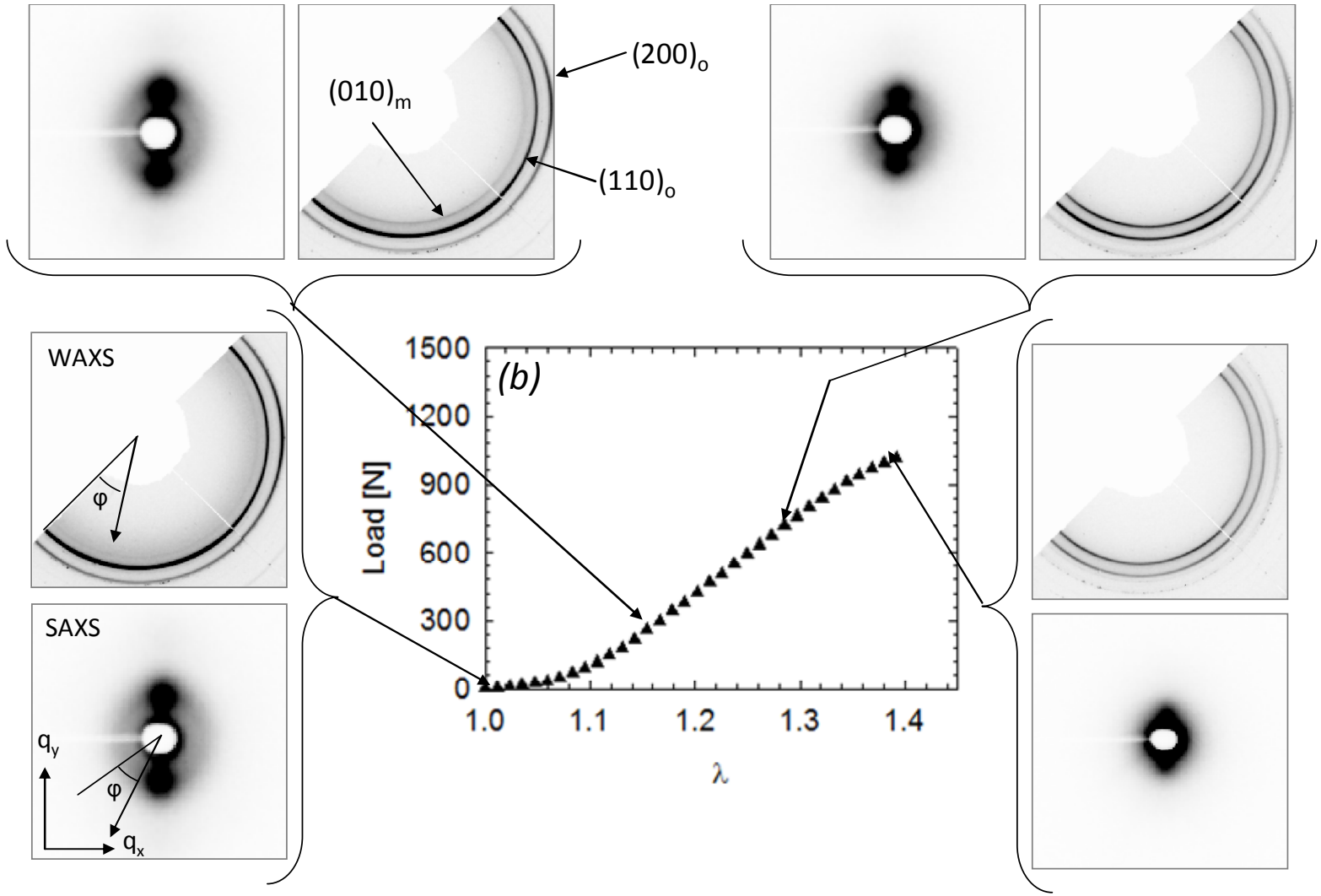

Figure 32 continued

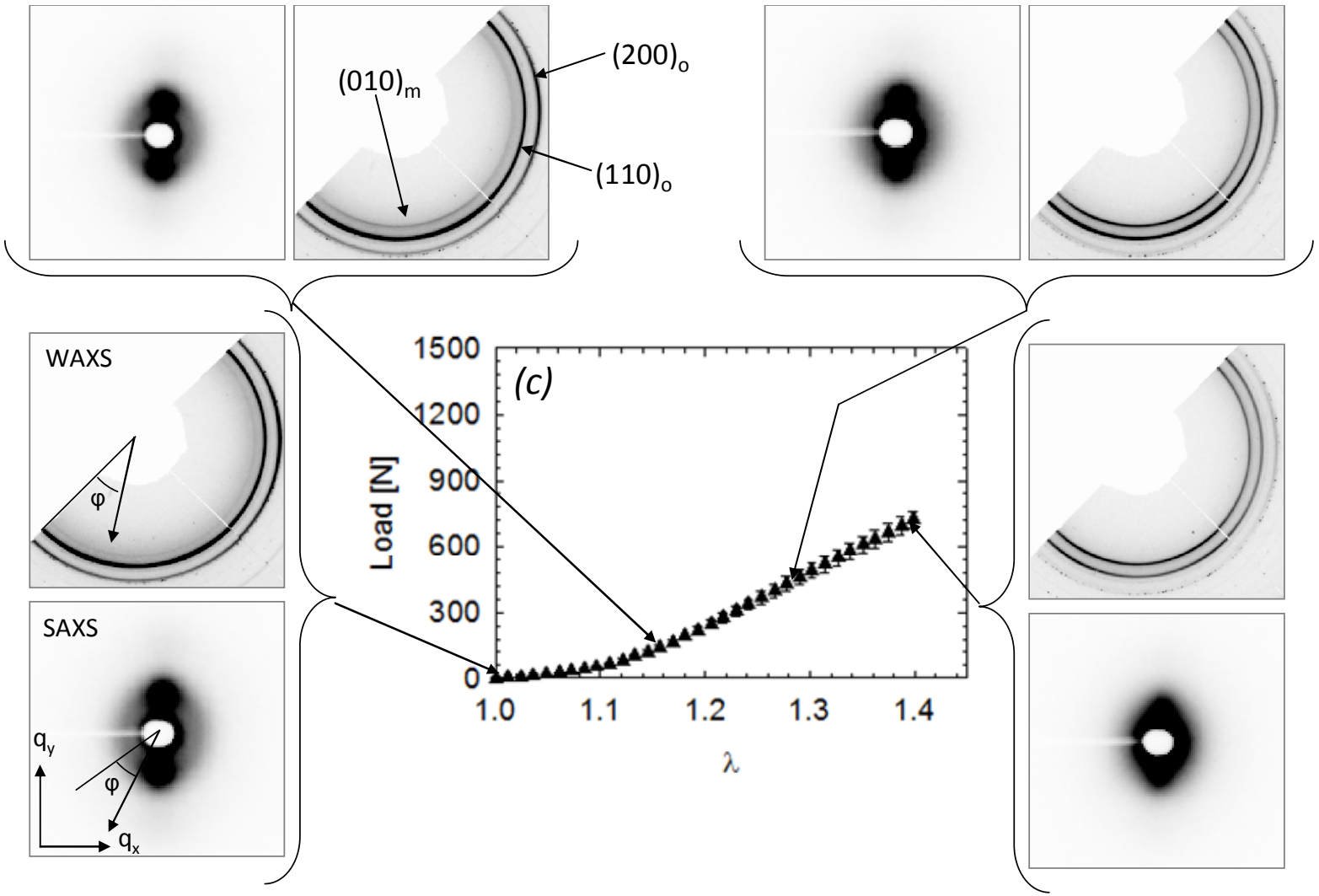

Figure 32. continued

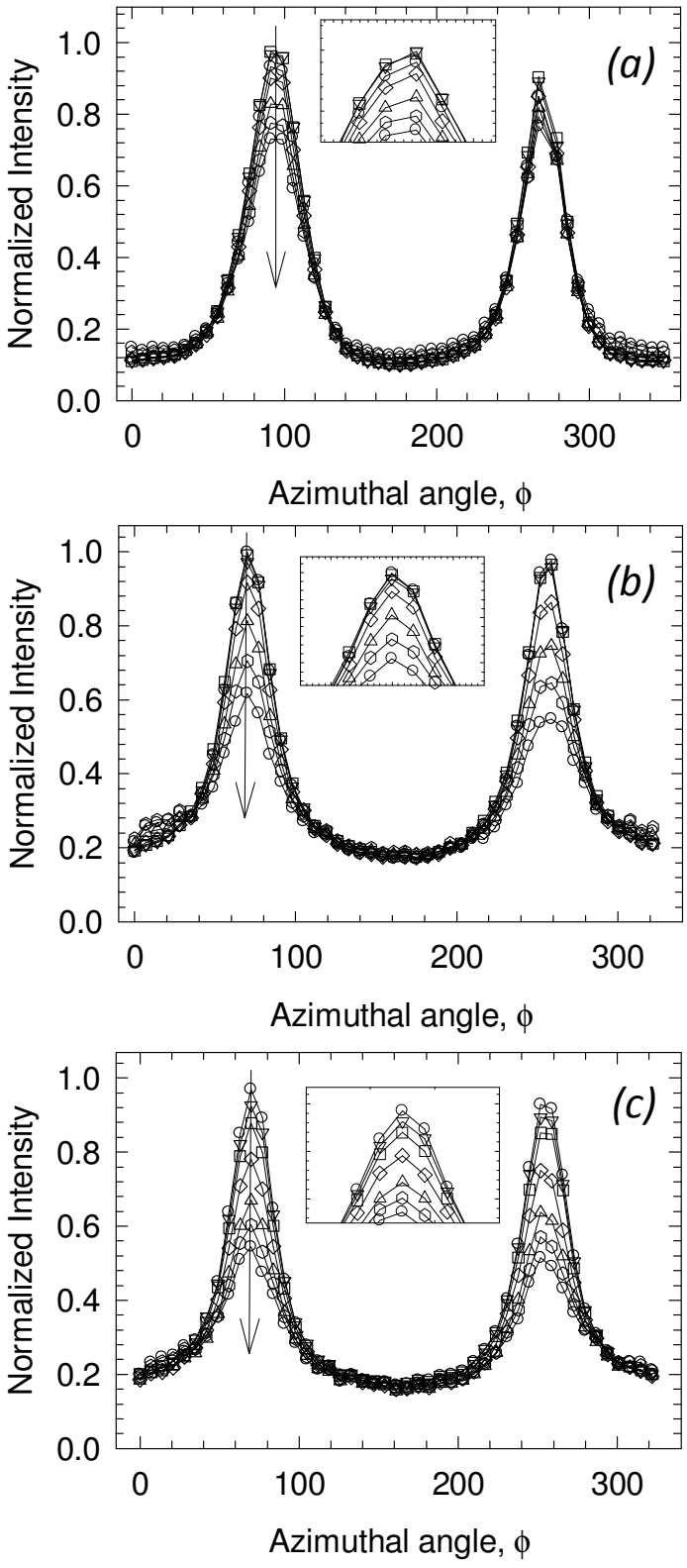

Figure 33. *Azimuthal scans over the SAXS peak position q=0.24 A^{-1} with increasing deformation (arrow direction) for (a) PE, (b) PENC3 and (c) PENC6*

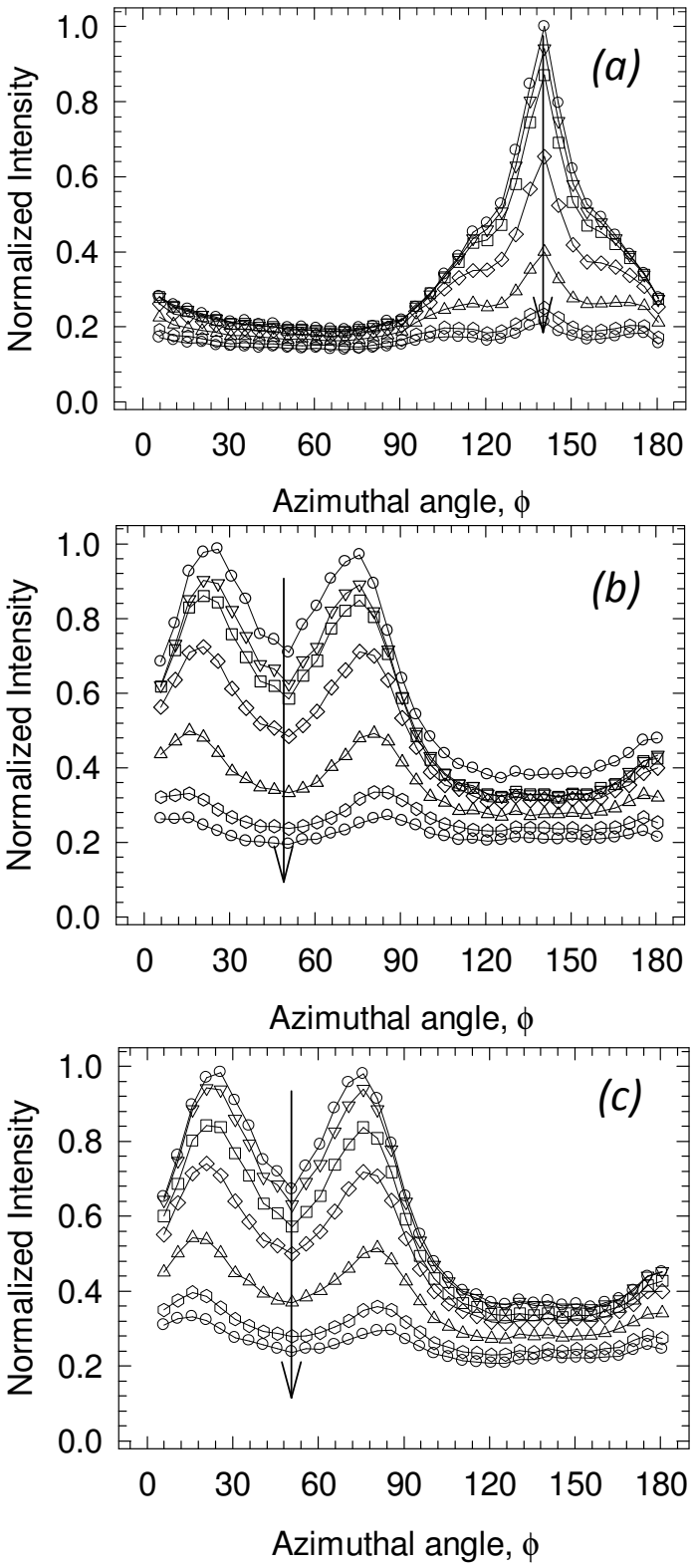

Figure 34. *Azimuthal scans for (110) orthorhombic crystal of PE in WAXS data with increasing deformation (arrow direction) for (a) PE, (b) PENC3 and (c) PENC6*

Scattering from clay platelets were not present neither in the small nor in the medium and wide angle ranges indicating that a good degree of exfoliation was achieved in the sample preparation process during mixing and extrusion.

As discussed in Chapter II, the value of the characteristic semi-crystalline lamella repeat dimensions, d_{ac}, can be obtained from the position of the maxima in the momentum transfer (q) observed in the 1D SAXS data using the relationship, $d_{ac} = 2\pi / q$, and the details about the thicknesses of the amorphous (d_a) and crystalline (d_c) regions can be determined by calculating the one-dimensional correlation function *K(z) [64, 77, 117]*. The correlation function was determined using the CORFUNC analysis software [118], with typical results shown in Figure 35 for PE at different strains. Individual curves at different strains have been shifted vertically for clarity, with strain increasing upwards. Since the samples have a typical crystallinity of 65 wt% or greater, the smallest dimension can be assigned to be the amorphous layer thickness (d_a) as shown in the inset to Figure 35. The schematic of the ideal lamellar morphology proposed for the correlation function calculations is shown in Figure 36 indicating d_a and d_c as well as d_{ac}.

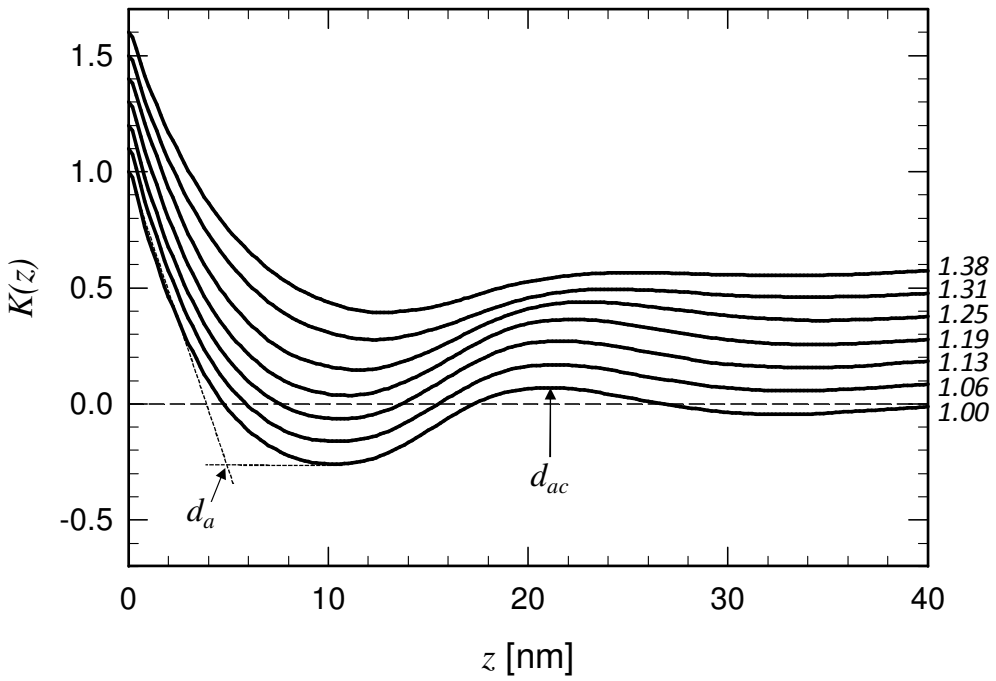

Figure 35. *A typical set of correlation functions obtained from 1D SAXS spectra for PE at room temperature at various strains. The length scales of definitions of d_{ac} and d_a are defined as indicated on the $\lambda = 1.00$ curve. Corresponding strain values to each curve is as indicated on the right side.*

For samples measured at RT, the SAXS data also shows increased scattering at low q (< ~ 0.09 nm^{-1}) with increasing deformation. This scattering results from structures with dimensions of >70 nm and could result from void formation [12, 77, 82, 119]. The total amount of scattering can be quantified by determining the scattering invariant; $Q \propto \int_0^\infty I(q)dq$.

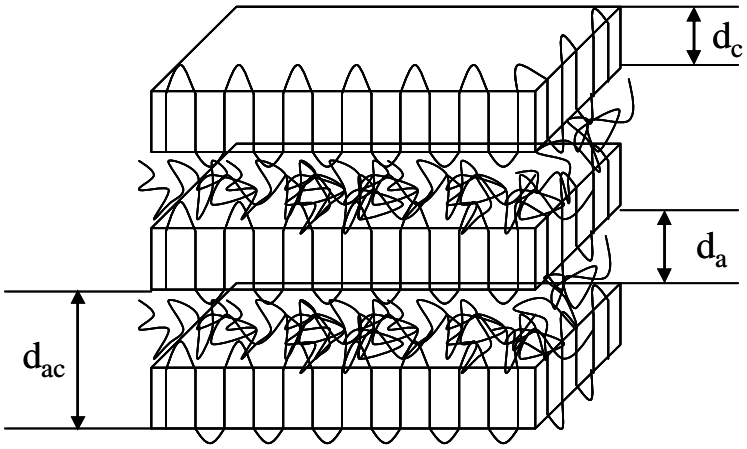

Figure 36. *Schematic of ideal lamellar morphology of polyethylene*

A representative example of a selected region of the 1D WAXS profiles as a function of increasing deformation in this case of PE is shown in Figure 37. In all the WAXS patterns of PE, and also the PENCs, three prominent and characteristic peaks were observed in the q range of 12 to 18 nm^{-1}. These peaks represent the crystallographic orthorhombic and monoclinic forms, of polyethylene. These crystal forms of orthorhombic and monoclinic unit cells are shown in Figure 38 with the related dimensions. Under atmospheric conditions the orthorhombic structure is preferentially formed which than may transform into the meta-stable monoclinic form by stress applied perpendicular to the molecular axis [120, 121].

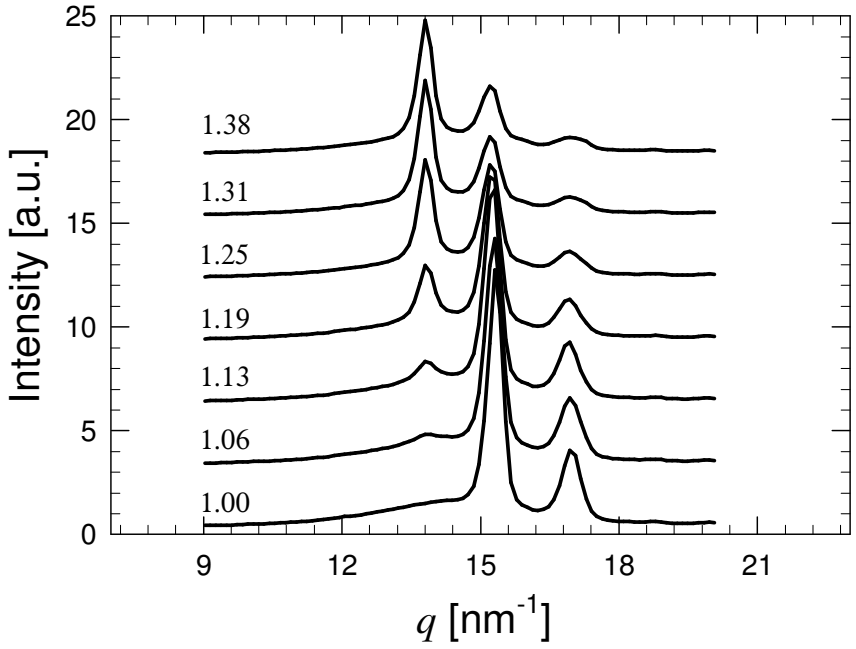

Figure 37. *Selected 1D WAXS data of PE under multiaxial deformation measured at room temperature as a function of strain (as indicated) measured at 0.0025s^{-1}. Data have been translated vertically for clarity.*

The WAXS data shows that with increasing deformation the peak at q = 13.8 nm^{-1} associated with the monoclinic $(010)_m$ HDPE grows in intensity. Over the same deformation range, the peaks at q = 15.3 and 16.9 nm^{-1} associated with orthorhombic $(110)_o$ and $(200)_o$ HDPE, respectively, both decrease. The areas under the crystal peaks can be used as an indicator of the crystal composition; and the increase in the monoclinic crystal peak intensity in the expense of the decrease in the orthorhombic crystal peak intensities show that there is a change in the crystal composition of PE. The q positions of the crystalline peaks do not change, indicating that the crystal unit cell dimensions do not change with deformation as has been seen in uniaxial deformation of HDPE and HDPE/clay nanocomposites [122]. These WAXS results are consistent with a stress

induced martensitic transformation where the orthorhombic structure of undeformed PE is converted to the monoclinic structure in the deformed HDPE [11, 12, 15, 72, 123, 124]. Under uniaxial loading the onset of martensitic transformation, however, is observed to coincide with the yield point [11, 15, 72], whereas in the current systems under multiaxial deformation the martensitic transformation starts soon after the strain is applied at RT and well before the yield points measured for the polymers (see Table 7). In addition, we do not observe the formation of hexagonal $(100)_h$ peaks that have been observed by Tzavalas *et al* [87, 122] in uniaxially deformed HDPE samples, which suggests that although similar phase transformation behavior is observed both for uniaxial and multiaxial deformation, the mechanisms are different. For all PE and both PENC samples at both deformation rates and temperatures, the relative amount of crystallinity estimated by the total area under the three orthorhombic and monoclinic crystalline peaks decreases with increasing strain. The relative total amount of crystallinity at maximum stretch ratio was seen to reduce to only ~20-40% of its initial value, depending on strain rate and temperature.

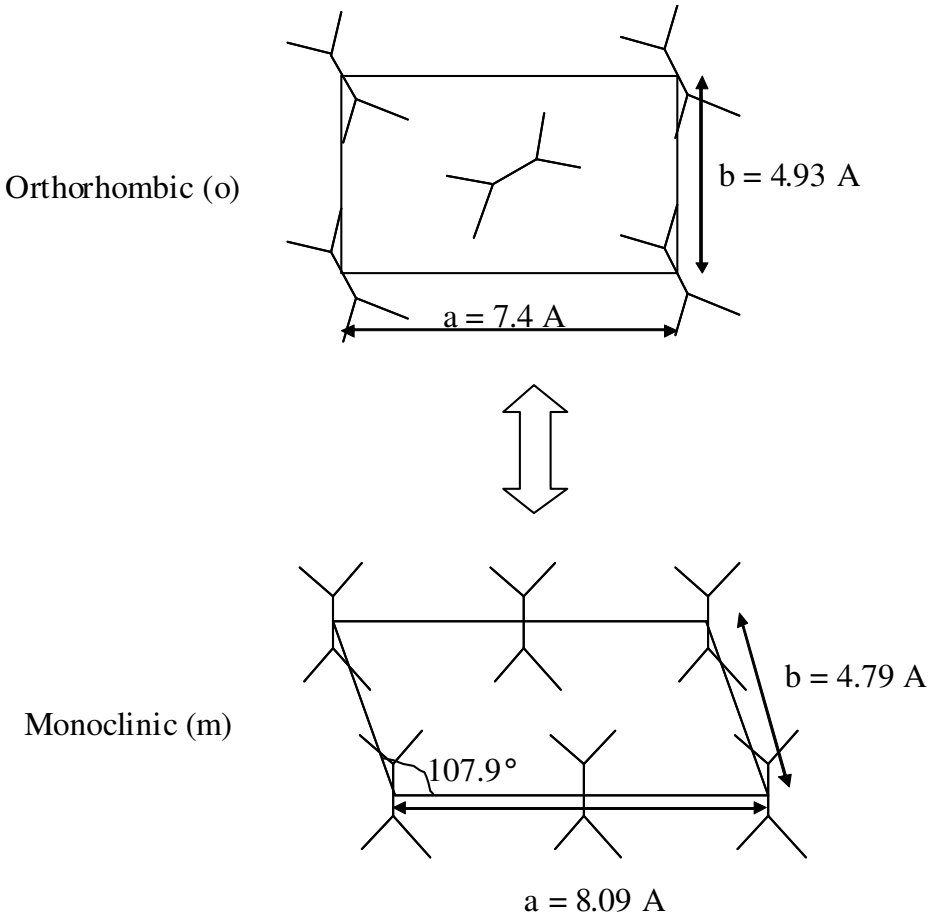

Figure 38. *Crystal structures of orthorhombic and monoclinic forms of polyethylene.*

5.3.1 Influence of Temperature

1D SAXS data as a function of strain measured at a strain rate of 0.0025 s^{-1} at both room temperature (RT) and 55°C initially show two broad maxima centered at q positions of ~0.24 nm^{-1} and ~0.66 nm^{-1} (see

Figure 39). These maxima are consistent with two different average lamella characteristic repeat thicknesses, d_{ac}, of 26.1 and 9.5 nm, respectively. The observation of two different length scales could well result from the sheet forming process of the polymer samples, in which the polymer was chilled from the melt on one face only by the

chill rolls. Under these circumstances it is very likely that the cooling of the sheet created a temperature gradient through the thickness of the polymer sheet which resulted with two different average lamellae thicknesses. With increasing deformation, at RT the dominant peak at q = 0.24 nm^{-1} shifts to lower q values, reflecting an increase in d_{ac} reaching 32.2 nm at $\lambda = 1.38$. By contrast, no change in this peak position and therefore d_{ac} is observed at 55°C, suggesting the amorphous chains have more degree of freedom at this temperature and are able to distribute the stress without any global chain extension.

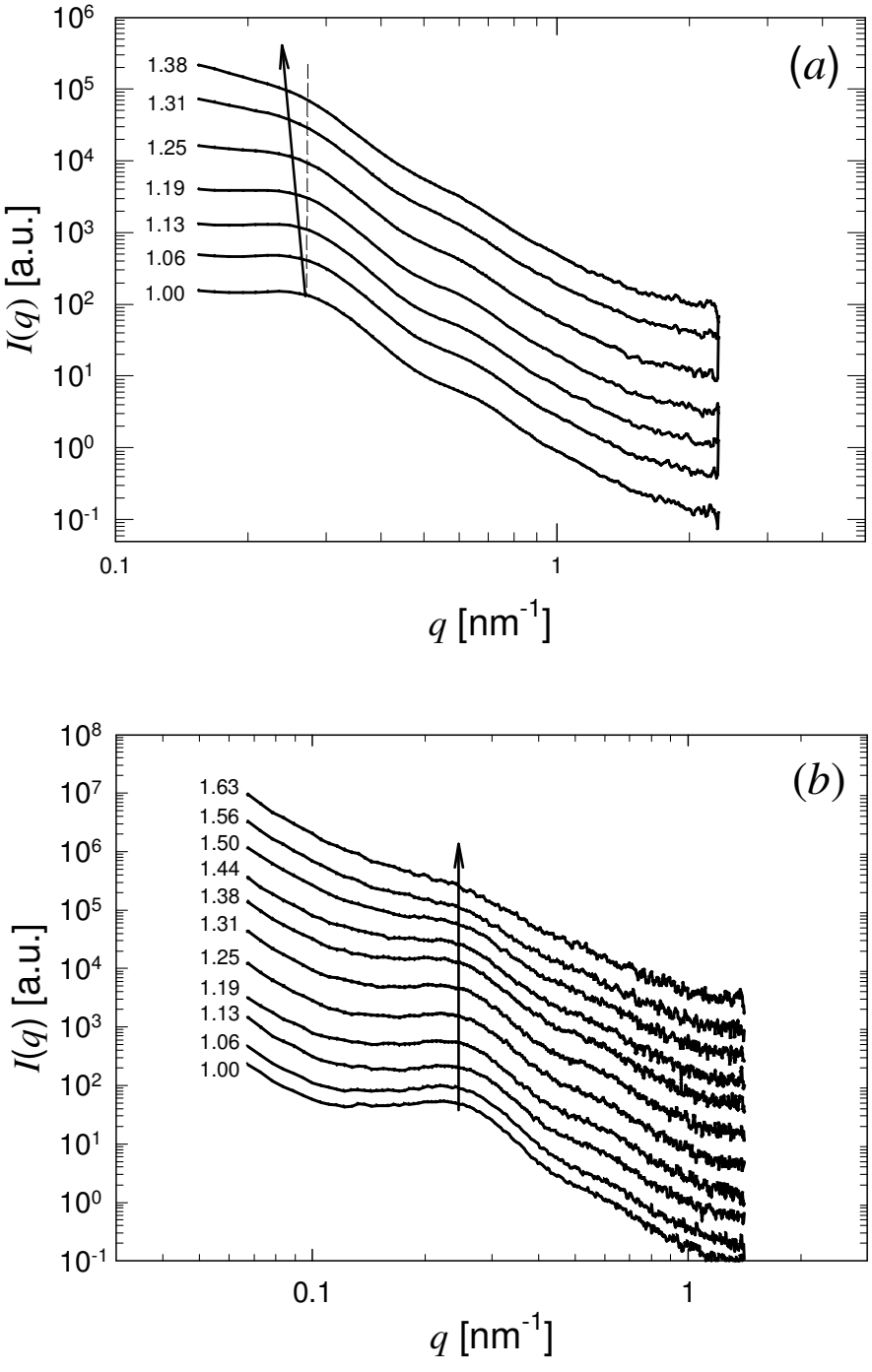

Figure 39. *1D SAXS data of HDPE at a rate of 0.0025s^{-1} at a) room temperature and b) 55^{o}C. The solid arrows indicate direction of increasing strain, with the numbers indicating the strains.. The vertical dashed line in (a) is a guide to the eye showing a constant q = 0.24nm^{-1}. The strains have been translated vertically for clarity.*

The calculated characteristic dimensions, d_{ac} and d_a, as a function of strain for the polymer and the nanocomposites at room temperature, obtained from the 1D-correlation function analysis of the SAXS data are shown in Figure 40. The data indicates that the observed increase of d_{ac} is almost entirely due to the increase in d_a. As anticipated at $55^{\circ}C$, since the peak at $q = 0.24nm^{-1}$ did not change position and therefore d_{ac} was constant with increasing strain, the 1D-correlation function analysis confirmed that there was no change in either d_c or d_a. This is possibly due to the increased degree of freedom of the amorphous chains at this increased temperature allowing relaxation. It is important to note that there is no significant difference in d_{ac} of PE and PENCs. Although the clay layers are expected to disperse in the amorphous component of polyethylene, they were not observed to contribute to the amorphous layer thickness at RT at this rate of deformation. This could result from the well degree of exfoliation achieved in the nanocomposites hence the degree of freedom of the amorphous chains is not greatly effected by clays.

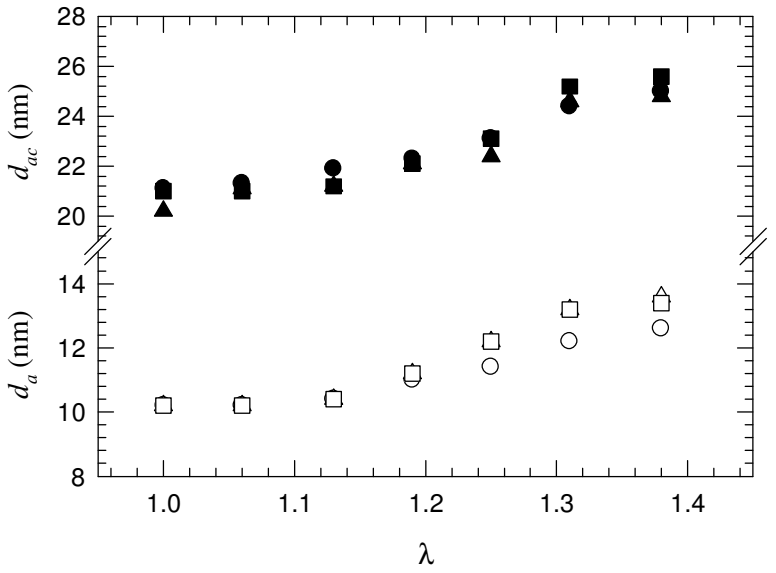

Figure 40. *Characteristic repeat spacing (d_{ac}), and amorphous layer thickness (d_a) as a function of strain at room temperature and rate of 0.0025s^{-1} for PE (circles), PENC3 (triangles) and PENC6 (squares). Data for 55°C is not plotted since there is essential no change in d_{ac} or d_a (or d_c) with strain.*

From the 1D correlation analysis it is also possible to determine the crystallinity, $\alpha_c = d_c / d_{ac}$, which is defined as the linear crystallinity [77]. Since α_c is evaluated from the SAXS data, it is a measure of the crystallinity determined over large dimensions. Our SAXS data yields initial values of α_c from 78 to 83% for the three samples at RT, which is consistent with the percent crystallinity of 73±2% obtained from DSC measured (ex-situ) after removal of applied strain. As seen from Figure 41 (*a*), the values of α_c essentially remain constant with increasing deformation for all of the materials, indicating that there is no change in crystallinity with the applied strain. A decrease in the total amount of crystallinity in the WAXS data is observed with increasing strain which is a result of the limited *q* range used to determine the WAXS

crystallinity as well as the reduced contribution to the crystal scattering as a result of the reduced sample thickness.

At both RT and 55°C, the peak amplitudes in the SAXS profile both decrease with increasing strain, with the most significant loss in amplitude observed at the higher temperature. The loss in peak amplitude at 55°C could result from either the lamellar stacks rotating into the strain direction and are therefore becoming increasingly perpendicular to the X-ray beam, or more likely from spherulite breaking up, causing a reduction in their average lateral dimensions. Another reason would be the excess amount of void scattering overcoming the lamella scattering to be observed at room temperature. As shown in Figure 41 *(b),* with increasing strain there is also an increase in the amount of small angle scattering in the low q region for systems measured at room temperature as a results of formation of voids [11, 83]. This is consistent with the observed whitening of the sample during deformation.

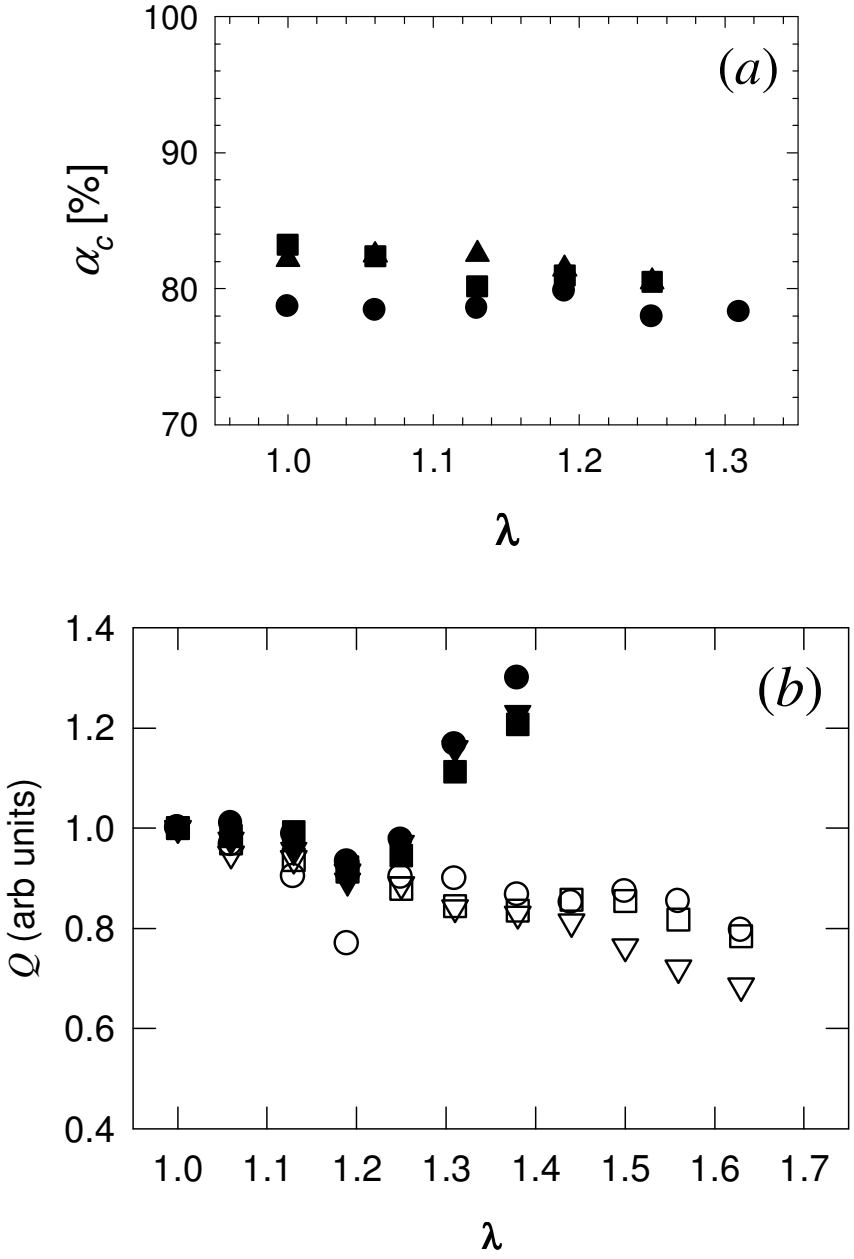

Figure 41. *(a) Change in the local crystallinity of PE (circles), PENC3 (triangles) and PENC6 (squares) with respect to increasing multiaxial deformation at room temperature and 0.0025 s^{-1} strain rate. (b) Excess scattering determined via the invariant (Q) as a function of strain at RT (filled symbols) and 55°C (open symbols).*

The integrated intensities of the peaks at WAXS region can be used as indicators of crystallinity (For further information on obtaining the integrated intensities of the crystal peaks, please see Appendix D). Figure 42 shows the change in the integrated intensities of monoclinic and orthorhombic peaks during stretching at room temperature and 55 °C. At the higher temperature, higher strains were achieved due to a decrease in the brittleness of the polymer. The decreases observed in the orthorhombic crystal intensities were similar at both temperatures up to a stretch point of 1.38. However, compared to room temperature measurements, at 55°C the onset of the stress induced martensitic transformation from orthorhombic to monoclinic phase occurs at higher strains. This is believed to be due to a hindered formation of the monoclinic phases as the crystallite melting is more favored at that higher temperature. In other words the monoclinic phase is formed more readily at lower temperatures [12, 125], as evidenced by the greater amounts of monoclinic crystals formed at room temperature. Unlike the room temperature behavior, the initial growth rates of monoclinic crystals are approximately constant at 55°C for both the neat polymer and the nanocomposites.

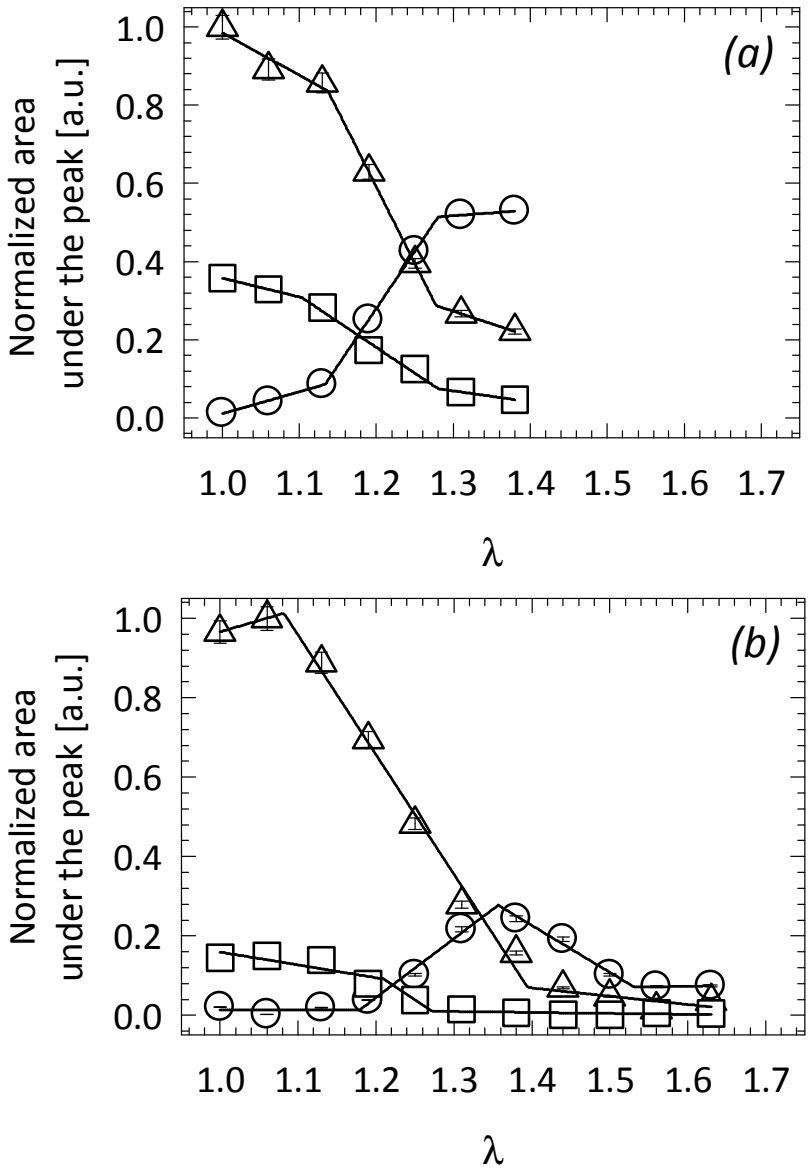

Figure 42. *Relative changes of peak intensities of (010) monoclinic (circles) and orthorhombic ($(110)_o$ - triangles, $(220)_o$ –squares) crystals of PE under multiaxial deformation as a function of strain measured at (a) room temperature and (b) 55°C. Lines are guides to the eye only.*

A number of factors have been postulated to explain the loss of monoclinic crystals in PE as seen in our case for $\lambda > \sim 1.38$ at 55ºC [11, 12, 17]. Of these, the most likely explanations are either local stress relaxations following formation of cavitations or

molecular orientation and the reduction in overall crystallinity. No increase in the orthorhombic crystal peak intensities is observed when the monoclinic intensity decreases. It is unlikely that monoclinic phases are re-crystallizing due to the lower temperature of the deformation. DSC measurements of samples before and after deformation have shown that there was no significant change in the crystallinity of the samples due to deformation. Therefore, the decrease in the $(010)_m$ intensity at 55ºC at higher strains is associated with cavitations (or void formation) allowing stress relaxation, since monoclinic phases are observed in PE under stress conditions.

Within the error of the measurements, at room temperature the relative percentages of the monoclinic and orthorhombic phases determined by area under the relevant WAXS peaks, were found to vary approximately linearly with each other (see Figure 43*(a))*. The rate of change in the formation of monoclinic crystals as opposed to reduction in orthorhombic crystals for both the PENC3 and PENC6 nanocomposites at $0.0025s^{-1}$ at RT, is slower than that for the neat polymer, indicating a hindered transformation mechanism in the presence of clay. Within the error of these experiments, there is no difference in the effect observed between the samples containing 3 or 6 wt% clay. Similar effects of clay platelets on PE have been observed under uniaxial deformation where the presence of clay platelets yielded slower rates of martensitic transformation [83, 87]. At 55°C, the initial rate of martensitic transformation is approximately the same in the PE and the PENCs with loss of orthorhombic phases is approximately linear with monoclinic growth (see Figure 43 *(a)*). At this temperature the polymer – clay platelet interactions are probably reduced compared to lower temperatures due to the increased degree of freedom of the chains. This is probably also the reason for

the reduced enhancement of the yield strains with increasing clay loading seen with increasing strain (Table 6). As can be seen in Figure 43*(b)* above a stretch ratio of ~1.38 the amount of orthorhombic and monoclinic phases decrease, leading to the non-linearity in monoclinic versus orthorhombic growth.

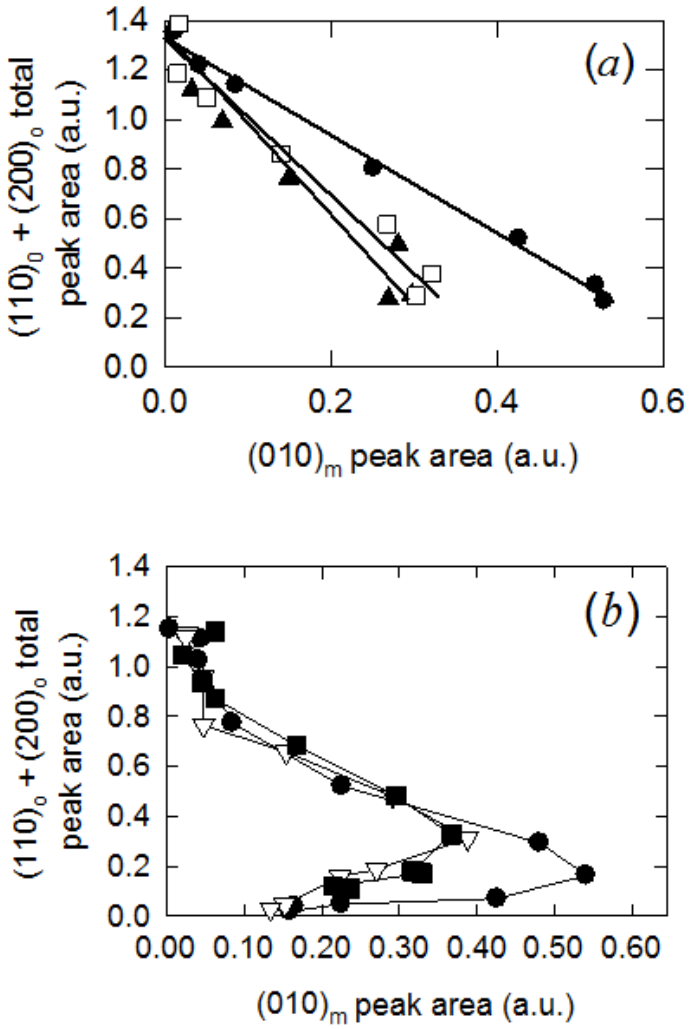

Figure 43. *Correlation between the decrease in the orthorhombic peak intensity with the increase in the monoclinic crystal intensity for PE (circles), PENC3 (triangles) and PENC6 (squares) deformed at (a) room temperature and (b) 55℃ at a strain rate of 0.0025s^{-1}.*

5.3.2 Influence of Strain Rate

Figure 44 shows the values of the amorphous layer thickness (d_a) at RT for PE, PENC3 and PENC6 with increasing strain at two different strain rates. For all systems, it is clear that d_a depends both on the strain and the strain rate. At the slower strain rate, d_a remains nearly constant up to a strain of 1.1 before increasing. By contrast, at the higher strain rate, the onset of d_a increase occurs at slightly lower strains. The results are in agreement with an earlier observation by Addiego et al. where the volume dilatation of HDPE was studied at different strain rates under uniaxial tension and an increased volume dilatation observed with increasing strain [76]. In addition there is a subtle difference in d_a values between the neat polymer and the nanocomposites where d_a is slightly larger for nanocomposites. This may be associated with clay-polymer interfacial de-bonding [126, 127] where the reduced interaction of clays at the interface of clay and polymer adds up to d_a and this is observed as a bigger increase in d_a with increasing strain.

With increasing strain, greater than 1.2, there is excess scattering (as determined via the scattering invariant, Q) at low q in the SAXS data (see Figure 45). The excess scattering is most significant for the higher strain rate deformation, which is consistent with the void formation. The increase is the same for both the PE and PENCs at both strain rates, and is clearly related to the polymer and is unaffected by the presence of the clay. The increased void formation, as seen by the larger amount of excess scattering, is probably due to the reduced ductility with increased strain as indicated by the lower yield strains (see Table 6).

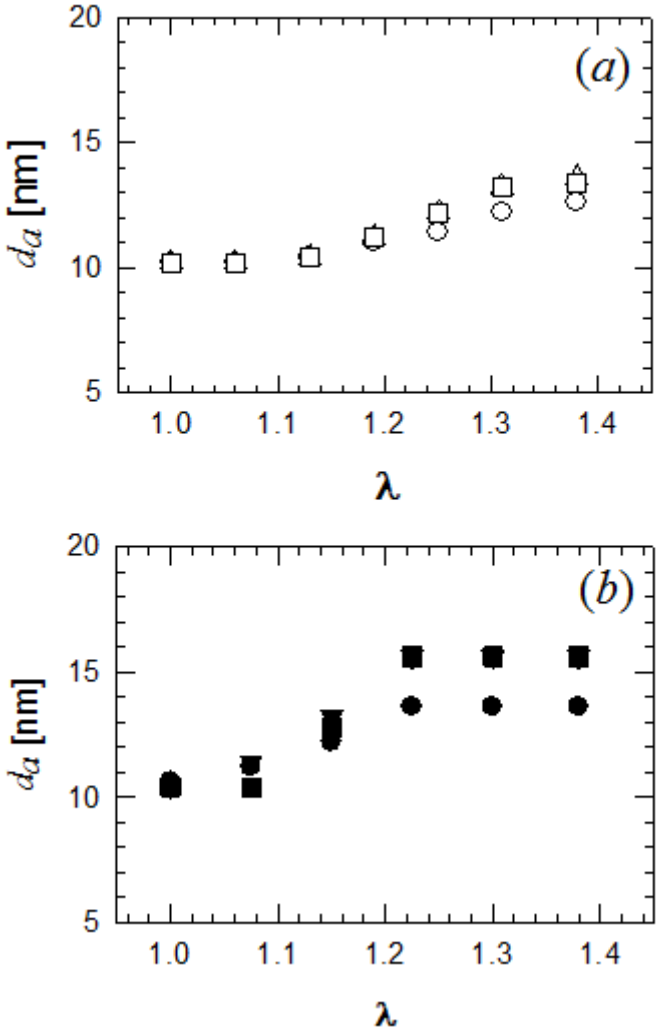

Figure 44. *The amorphous layer thickness (d_a) as a function of strain for PE (circles), PENC3 (triangles) and PENC6 (squares) at (a) 0.0025s^{-1} (open symbols) and (b) 0.025s^{-1} (closed symbols) at RT.*

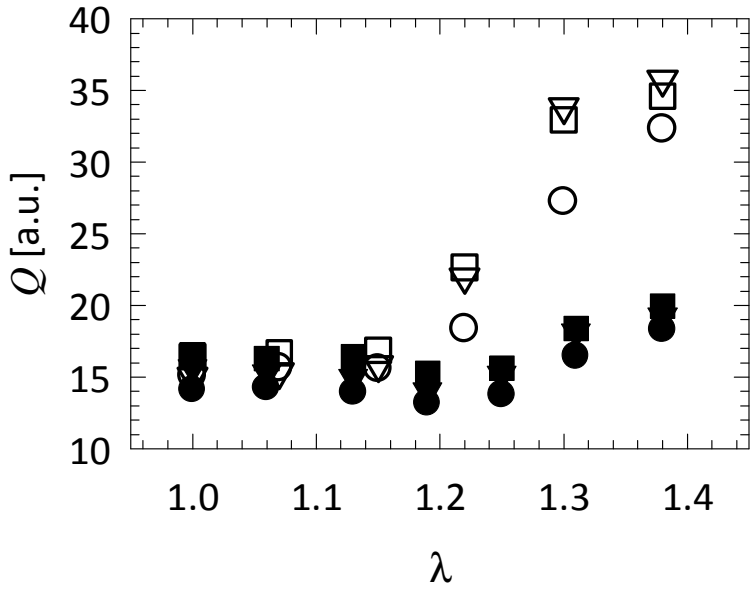

Figure 45. *Scattering invariant (Q) as a function of extension ratio at RT for PE (circles), PENC3 (triangles) and PENC6 (squares) at 0.0025 s^{-1} (closed symbols) and 0.025 s^{-1}(open symbols).*

The change in monoclinic and orthorhombic intensities during stretching at two different strain rates is compared in Figure 46. At $\dot{\gamma}$ = 0.025s^{-1} the growth of the monoclinic phase reached a plateau at a smaller strain (~λ=1.2) than the lower rate of 0.0025 s^{-1} (~λ =1.3). Over the same strain region, both orthorhombic peaks decrease and attain an approximately constant value at lower strain values. The drop in the monoclinic phase content is believed to be due to the local stress relaxations caused by chain slip and cavitations as discussed before [12, 15, 82, 86]. Although not shown here the nanocomposites exhibit similar trends to the neat PE with decrease of orthorhombic peak intensity with increasing strain at 0.0025s^{-1}. However, the relative amount of the monoclinic phase formed in the nanocomposites with increasing strain is less than PE at both strain rates as seen in Figure 47. This suggests that the nucleation of monoclinic

phase is inhibited by the existence of nanoclay, possibly because the clay platelets create a confined environment for the orthorhombic PE crystals to convert into monoclinic crystals.

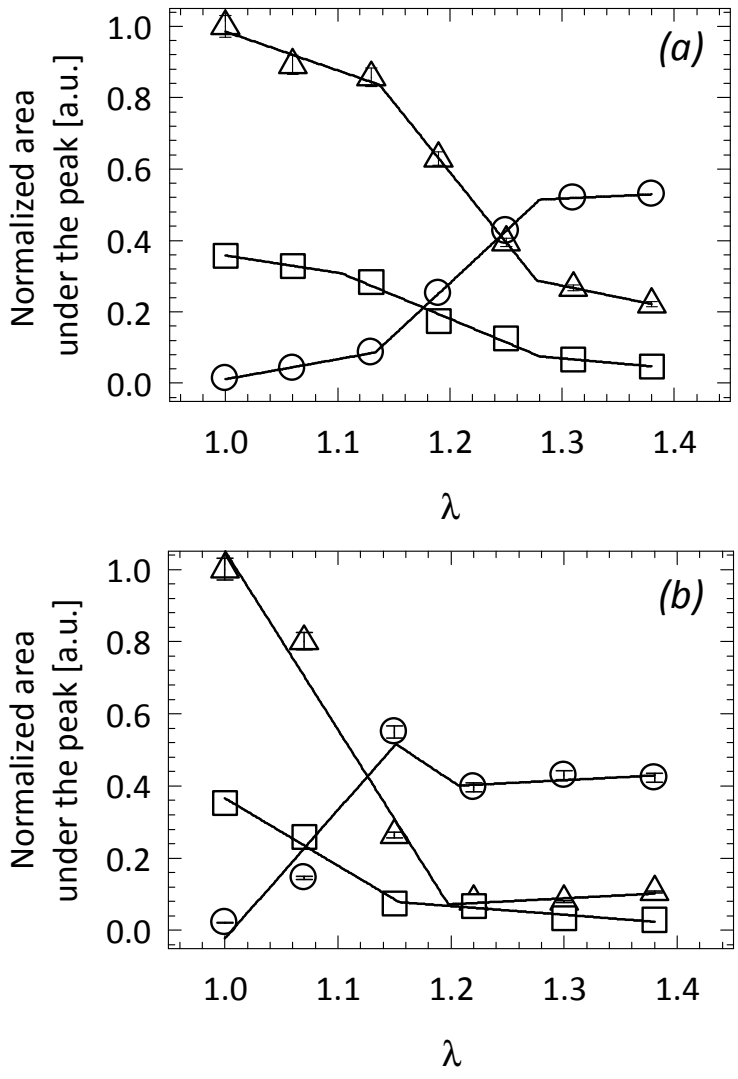

Figure 46. *Relative changes of peak intensities of monoclinic (circles) and orthorhombic (110_o - triangles and 200_o - squares) crystals of PE during multiaxial deformation as a function of strain measured at (a) $0.0025s^{-1}$ and (b) $0.025s^{-1}$. Lines are guides to the eye only.*

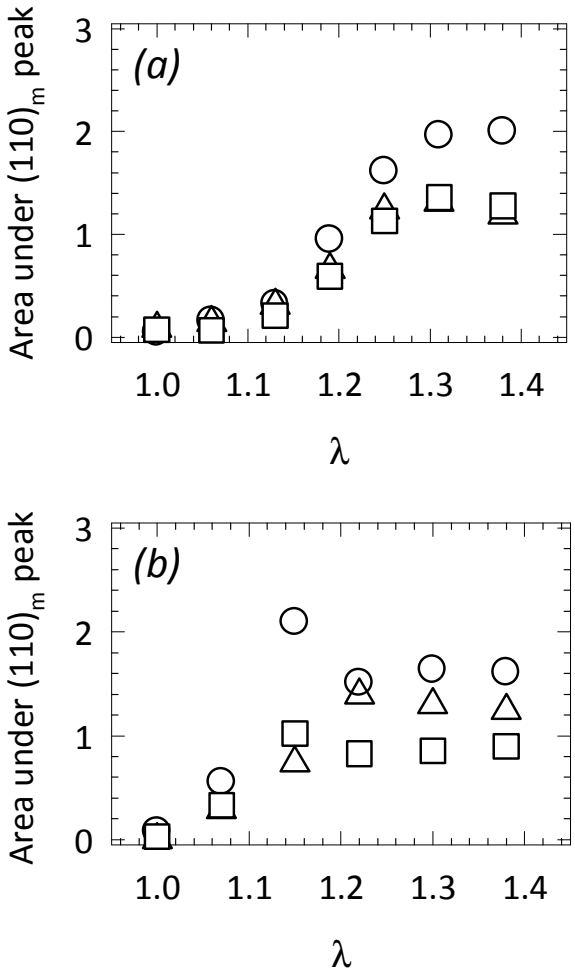

Figure 47. *Relative changes in the amounts of monoclinic crystals of PE and PENCs under multiaxial deformation as a function of strain measured at (a) 0.0025 s^{-1} and (b) 0.025 s^{-1}. Symbols correspond to PE (circles), PENC3 (triangles) and PENC6 (squares).*

5.4 Time dependent recovery after multiaxial deformation

As indicated above, internal relaxations take place in the sample morphology when measured after deformation; hence it would not be possible to see what is happening to the polymer morphology during deformations with ex-situ observations.

To study the structural changes during recovery after cessation of deformation the PE and PENC samples were stretched up to a stretch ratio of 1.38 and then the applied stress was fully removed by removing the sample from IMDD and allowing them to relax various periods up to several weeks. Figure 48 and Figure 49 show 1D SAXS and WAXS plots, respectively, of PE and PENCs before deformation, immediately after cessation of deformation, in addition to the data collected after 3, 4 and 5 weeks of recovery. The data from the undeformed sample and immediately after cessation of deformation were collected at APS, whereas the data from the relaxed samples were collected from DLS, hence there is an obvious intensity difference between the in-situ and ex-situ plots.

1D SAXS plots suggest that the amorphous chains in neat PE shows a faster recovery compared to the amorphous chains in PENCs; as the peak at $q=0.24\ nm^{-1}$ has almost fully recovered in 3 weeks while it is still not full recover in PENCs even after 5 weeks of recovery time. A detailed analysis of the peak recovery was performed by calculating the area under the peak at $q=0.24\ nm^{-1}$, associated with the average dimension of polyethylene lamellae. The change under the peak area with respect to increasing recovery time for PE and PENCs are shown in Figure 50. The figure suggests that the amorphous chains in PE have shown a greater recovery as seen from the greater area under the curve compared to PENCs. However this recovery was not completed fully in 3 weeks, as the area kept growing as recovery time increased up to 5 weeks. On the other hand the recovered area under the peak for PENC3 and PENC6 were smaller compared to PE. Although we see a slight increase with time, when comparing PENC3 with PENC6, it is also seen that the recovered area is smaller in PENC6, the highest clay content nanocomposite. This implies that the clays platelets create a restrained environment by

surrounding the amorphous chains hence reducing the chain's degree of freedom during recovery period. This delayed recovery effect is observed to be intensified with increasing clay amount. In addition the peak positions were observed to remain constant with respect to the position in the as made sample indication that the lamellae dimension was fully recovered.

From the WAXS data, the monoclinic crystallites were observed to revert back to their initial orthorhombic crystal forms in 3 weeks for all materials. Figure 49. shows the in-situ collected WAXS plots together with the data from relaxed samples. The transformation from metastable monoclinic crystal phase back to stable orthorhombic crystal phase was expected to occur immediately once the stress was removed as the metastable phase is only observed under stress [11, 125]. As a result, it was not expected to track any changes between the recovery times of 3, 4 and 5 weeks. In order to track the effect of time, if any, the area under the $(010)_m$ crystal peak was calculated and used as an indication of the amount remaining monoclinic form in PE and PENCs. Figure 51 summarizes the changes in the monoclinic peak area with respect to increasing recovery time. The figure suggests that the transformation back to orthorhombic phase have occurred immediately in PE and PENC3 as the increasing recovery time did not change the amount of monoclinic phase. On the other hand in PENC6 we see that the transformation from the monoclinic phase is still occurring as seen from the reducing amount of monoclinic phase with increasing recovery time. This suggests that the transformation of the monoclinic polyethylene crystals are effected by the existence of clays due to the confinement of the clays. Even if they are expected to disperse in the

amorphous phase, clay platelets are able to restrict the crystal movement once they reach to a critical amount.

From both SAXS and WAXS data we have seen that the time dependent recovery of both the amorphous and the crystalline phase of polyethylene lamellae occur faster in neat PE compared to the nanocomposites. Once the clays are added to PE system, they induce some restrictions to both amorphous and crystalline domains of lamella and cause delay in chain movement. This delay is observed as the reduced rate in the lamella orientation recovery, calculated from the area under the oriented lamella peak, in the PENCs compared to PE. While, from the WAXD data, it is monitored as the increased transformation time of monoclinic crystal peaks hnece reduced rate in the decrease of monoclinic crystal amount in PENC6.

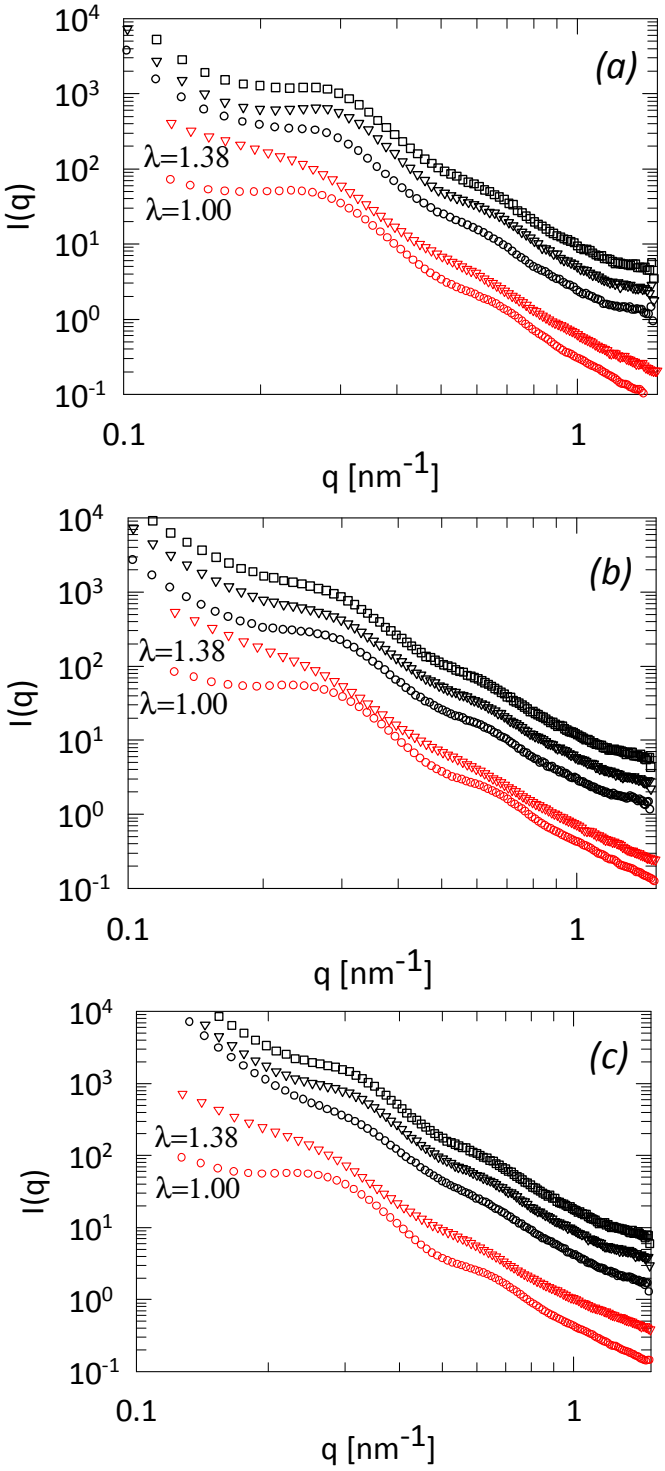

Figure 48. *1D SAXS plots for (a) PE, (b) PENC3 and (c) PENC6 at stages of right when deformation starts (○), right when deformation stops (∇), 3 weeks of relaxation (○), 4 weeks of relaxation (∇), and 5 weeks of relaxation (□). Plots are shifted upwards for clarity.*

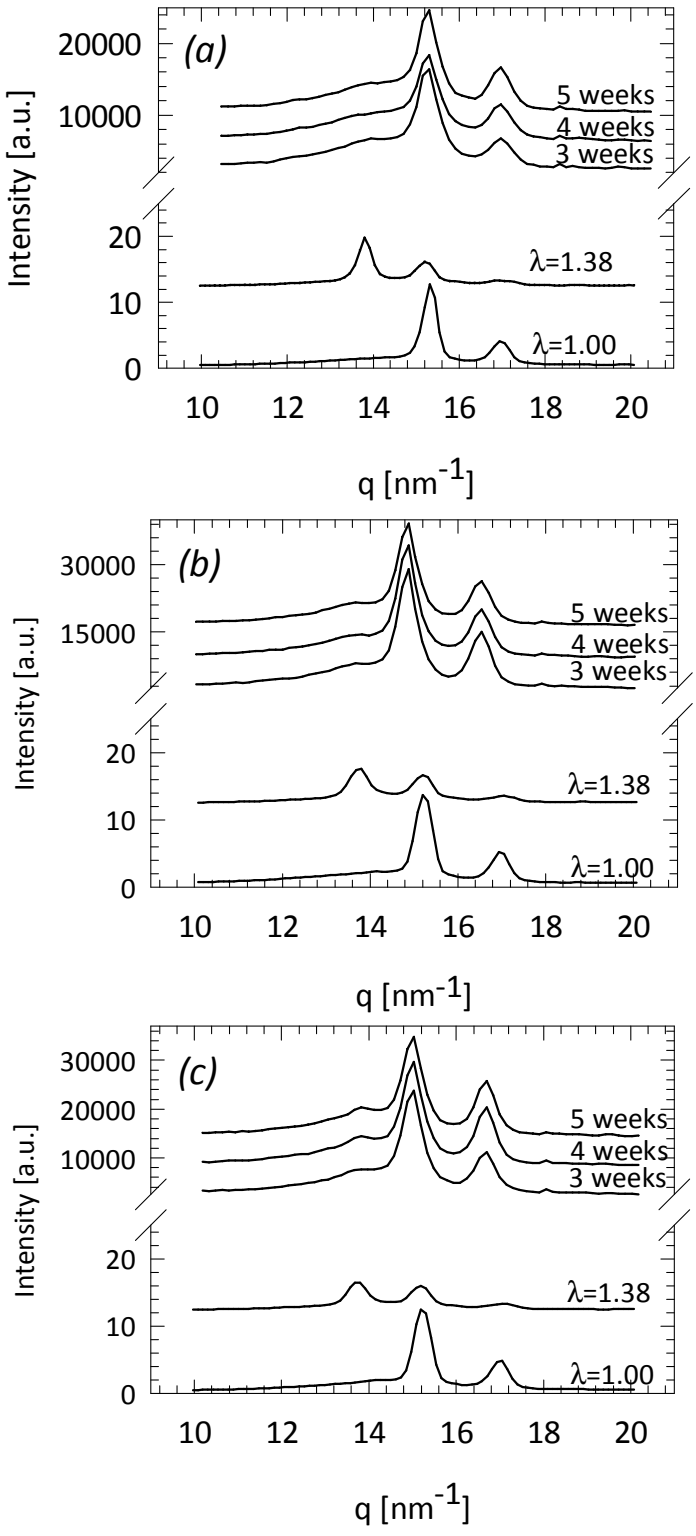

Figure 49. *In-situ and ex-situ 1D WAXS plots for (a) PE, (b) PENC3 and (c) PENC6 as indicated. Plots are shifted upwards for clarity.*

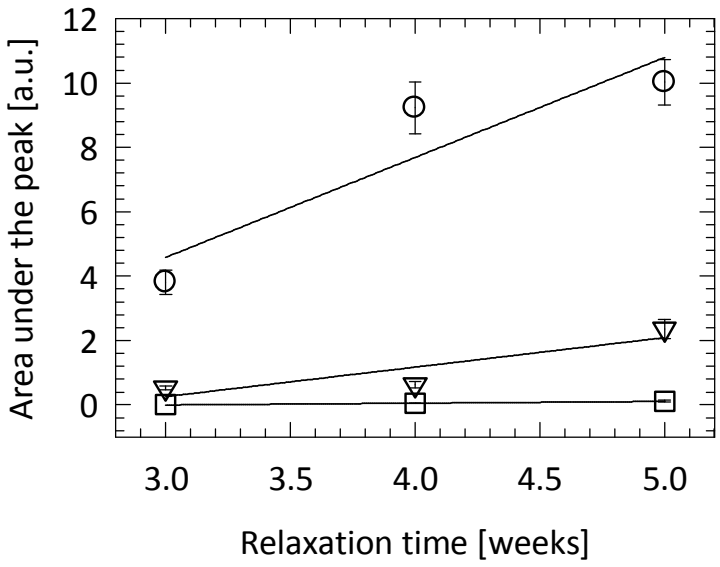

Figure 50. *Change in the area under the peak position $q=0.24nm^{-1}$ in the SAXS data with respect to increasing relaxation time for PE (circles), PENC3 (triangles), and PENC6 (squares). Lines are guides to the eye only.*

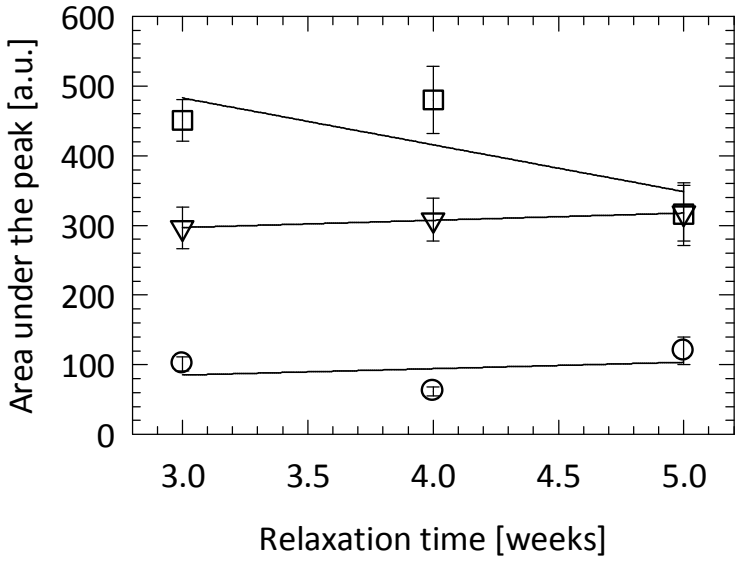

Figure 51. *Change in the area under the $(010)_m$ peak in the WAXS data with respect to increasing relaxation time for PE (circles), PENC3 (triangles), and PENC6 (squares). Lines are guides to the eye only.*

CHAPTER VI

RESULTS AND DISCUSSIONS ON PP AND PP/CLAY NANOCOMPOSITES

This chapter describes the results from *in-situ* multiaxial deformation studies of PP and PPNCs. Additionally it includes mechanical and thermal characterizations of PP and PPNCs as well as the effects of stress relaxations after multiaxial deformation on the polymer morphology. The effects of strain, strain rate and temperature on the polymer morphology changes in addition to these produced by the presence of the clays are discussed. Additionally the effect of shear on the melt behavior of PP and PPNCs are also presented and the effect of clays in the melt rheology is discussed.

6.1 Mechanical Properties

Mechanical property characterization was performed on PP and PPNCs the results of which are summarized in Table 9. Results suggest that the elastic modulus, hence the strength of PP, has increased with the addition of clays proportional with the amount of clays in PP. Table 9 also shows that it is possible to improve mechanical strength of PP up to 2.5 times with addition of >5wt% clay. In addition the toughness of PP was increased significantly with clay inclusions up to 5 wt% which shows that it is possible to improve mechanical strength of PP without sacrificing the ductility. However once the clay amount reached 10 wt% the toughness dropped significantly which shows reinforcements above 10 wt% require a sacrifice between the strength and the toughness.

Table 9. *Summary of uniaxial mechanical properties of PP and PPNCs.*

Material	E [GPa]	ε_y [%]	ε_b [%]
PP	12.2±0.09	5.81±0.08	496±15
PPNC1	14.6±0.11	6.19±0.01	591±18
PPNC2	11.7±0.08	6.27±0.40	588±18
PPNC5	30.3±0.06	3.11±0.07	493±13
PPNC10	31.0±0.10	2.64±0.08	247±12

Load vs. stretch ratio plots for PP and PPNCs measured during multiaxial deformation at room temperature are shown in Figure 52 and summarized in Table 10. During ex-situ tests the materials were deformed further compared to the in-situ deformations which could be an effect of the form of the deformation where the nose cone is pushed towards the retained film during ex-situ tests and retained film is pushed towards the nose cone during in-situ tests.

As observed for uniaxial deformation perhaps not surprisingly, when multiaxially deformed PP and PPNCs show increased toughness with increasing clay content up to 5 wt% addition. With a clay loading of 10 wt% the PP is brittle and the toughness irs reduced by ~1.5 times than the neat PP and the other PPNCs. This increase in the toughness was observed in the existence of clay platelets previously by *Okamoto et. al.* in foam materials and explained by the clay platelets turning their faces and aligning along the flow direction when subject to biaxial flow (planer orientation) which then causes an

increase in the strain at break [93]. Similar toughness improvements were observed during impact tests [128, 129] and explained by the rapid breakdown of the craze initiation zone in neat PP which does not provide adequate time for the material to respond strain, resulting in brittle-like behavior. The toughness of a material is generally related to the energy dissipating events that occur in the vicinity of a sharp crack. In the nanocomposites, the formations of microvoids are explained to be the responsible mechanism for high toughness. These microvoids release the plastic constraint in the matrix, triggering large-scale plastic deformation with consequent tearing of matrix ligaments between microvoids. While in the neat PP, only crazing contributes to energy absorption, in general, this could not absorb too much energy resulting in more brittle behavior [128, 129]. In addition to these, the stress transfer from the matrix to the reinforcements is more efficient in case of nanocomposites due to the increased surface area with the addition of clays, assuming good adhesion at the interface. Hence, the crack propagation length at the interface becomes longer, improving the toughness [130]. It was also observed that above T_g of the polymer, nanoparticles show cooperative motion and gain the ability to reorient themselves in the strain direction thus helping dissipate energy and reduce crack formation [42]. Depending on the SAXS data, discussed further in the Chapter, where no excess scattering was observed in the very low q region, we believe that the increased toughness is caused by the additional surface area for the cracks to propagate introduced by the clays rather than the formations of microvoids.

However when the clay content reached up to 10 wt%, PP has become more brittle as shown by the 20% decrease of the strain at break. This effect is probably due to the agglomeration of clays [131]. Strengthening of the polymer-filler interface is critical

to properly managing stress transfer during deformation and the formation of agglomerates, as indicated by the formation of a clay peak in the WAXS data, clays interact more with themselves and the polymer. Once the clay percentage reaches 10 wt% the tactoids are able to reduce the toughness probably due to the reduced interactions between the polymer and the clays, resulting a drop in the toughness of PP at room temperature. As the temperature of the deformation increases up to 55℃, this mechanism no longer applies and PP and all the PPNCs fail at similar stretch ratios.

Table 10. *Yield stretch ratio, λ^{*}, and break point stretch ratio, λ^{**}, for PP and PPNCs under multiaxial deformation at two different strain rates at room temperature.*

Material	**0.0025s-1**		**0.025s-1**	
	λ*	**λ****	**λ***	**λ****
PP	1.74±0.02	2.54±0.13	1.48±0.01	2.05±0.10
PPNC1	1.69±0.01	3.15±0.13	1.47±0.01	2.76±0.15
PPNC2	1.70±0.02	3.15±0.13	1.47±0.01	2.86±0.17
PPNC5	1.69±0.01	3.13±0.16	1.48±0.02	2.66±0.13
PPNC10	1.69±0.01	1.98±0.10	1.44±0.02	1.58±0.08

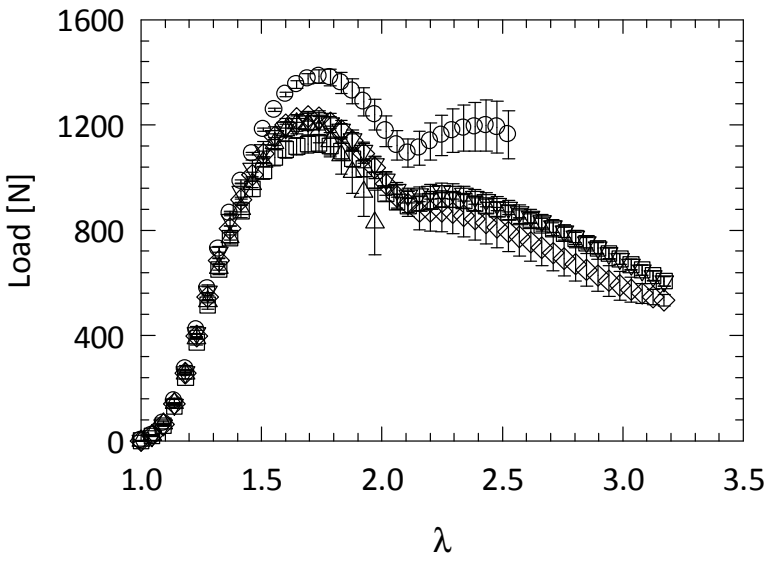

Figure 52. *Averaged multiaxial Load vs. λ curves for PP (○), PPNC1 (∇), PPNC2 (□), PPNC5 (◊), and PPNC10 (Δ) stretched at room temperature at 0.0025s^{-1} strain rate.*

6.2 Thermal Properties

Thermal properties of PP and PPNCs measured with DSC are summarized in Table 11. It was observed that the inclusion of clay did not alter the melting temperature of PP while the overall crystallinity decreased slightly. The unaltered melting temperature with increasing clay content in the PPNCs is similar to the PENC nanocomposites showing that the processing temperature range for PPNCs do not require changing compared to the pure PP. Similar results were reported before where a decrease in the crystallinity in PP with the addition of nanotubes and nanoclays were discussed [132-134]. Possible reasons suggested were the confinement of polymer chains between the intercalated clay layers which limits the degree of freedom of the chains [134]; or the

increased nucleation points created by the nanoparticles for the crystallization to proceed which eventually yielded reduced overall crystallinity and more imperfect crystals [132].

Table 11. *Thermal properties of PP and PPNCs.*

Material	T_m [℃]	X_c [%]
PP	162.0±0.8	72.2±3.0
PPNC1	162.2±0.9	67.6±1.5
PPNC2	162.8±0.4	67.9±3.5
PPNC5	162.5±0.6	66.1±2.5
PPNC10	162.5±0.8	66.8±5.0

6.3 General In-situ X-ray Observations

Representative i*n-situ* X-ray scattering images combined with ex-situ obtained the load versus λ curves for PP and PPNC10 deformed at room temperature at $0.0025s^{-1}$ are shown in Figure 53. As figure illustrates the scattering in the small angle regime increases significantly with increasing strain while in the wide angle regime the intensities drop over the same amount of deformation. The increase in the SAXS intensity at low q is due to the voids and crazes formed in the polymer with increasing deformation, which was optically observed by the whitening of the sample. The decrease in intensities of the crystal peaks in the WAXS data, on the other hand is simply due to the reducing of sample thickness. No evidence of crystallographic phase transformations are observed associated with the multiaxial deformation. However, some diffraction peak

intensities became progressively reduced with increasing strain especially for PPNC1, 2 and 5; and at high strains the peaks are almost lost. This indicates that the sample had either undergone a remarkable strain-induced amorphization [89] or the crystals are progressively orienting perpendicular to the beam hence could not be detected anymore; or both. Although it is not clearly seen from the 2D SAXS patterns of as made PP and PPNCs, the azimuthal scans (see Figure 54) show anisotropy as a result of the sheet extrusion process, similar to PE system. The anisotropy hence the preferential orientation in PPNC5 was observed to be preserved throughout the deformation. On the other hand due to the excess scattering in the further stages of the deformation, the azimuthal scans for deformed samples were dominated by void scattering and anisotropy was no longer observed as shown in Figure 55 for PP.

Figure 56 illustrates representative WAXS patterns for PP, PPNC5 and PPNC10 where the contribution to the scattering from the amorphous, crystalline and background components are shown. It is possible to obtain the amorphous peak by interpolating a line between a number of selected points. The crystal form of PP and PPNCs is dominated by the monoclinic α form as it is the most stable form and therefore under standard synthesis and processing conditions, α form is the predominant structure [135]. The obvious difference between the neat polymer and the nanocomposites is the presence of an extra peak (additional ring in the 2D images) associated with the clay crystals which grows in intensity with increasing clay content. Due to the isotropic nature of the multiaxial deformation, further analysis was performed by radially averaging the SAXS and WAXS patterns due which has the benefit of impairing data quality by improving signal-to-noise ratio.

Representative 2D SAXS images of PP and PPNCs are shown in Figure 57, before starting deformation commences and immediately after cessation of deformation at room temperature. Scattering intensity is observed to increase with increasing deformation for the neat polymer as well as PPNC10 as seen from the intensity profile in the images as well as the representative azimuthal SAXS profile of PP (see Figure 55) before and immediately after cessation of deformation. By comparison there is no significant increase in the scattering intensity of PPNC1, PPNC2 and PPNC5. The increase in intensity for PP and PPENC10 is believed to originate from formation of voids under deformation. Usually voids or cavitations are detected in the SAXS data by a large increase in low q scattering intensity, as discussed in Chapter V. Macroscopically, the extensive void formation is also observed as whitening of the deformed material. Under uniaxial deformation whitening is due to void formation only observed at strains greater than the yield point [136]. In the current case under multiaxial loading, the whitening of the PP and PPNC10 samples, associated with void formation, is observed immediately with increasing of strain.

Response of the PP and PPNCs to tensile deformation indicated an increase in the toughness of PP with the clays for 1, 2, and 5 wt%. The toughness of a material is generally related to energy dissipating mechanisms that occur in the vicinity of a sharp crack. In the nanocomposites, the microvoids are responsible for high toughness [128]. These microvoids release the plastic constraint in the matrix, triggering large-scale plastic deformation with consequent tearing of matrix ligaments between microvoids. While in the neat PP, only crazing mechanism contributes to energy absorption, which in general could not absorb too much energy, resulting in more brittle fracture behavior compared to

PPNCs. The high toughness of clay–reinforced PP nanocomposite is related to the crystal structure and dispersion state of nanoclay particles, and strong interfacial interaction between the nanoclay and polymer matrix [128]. Based on our observations for PPNC1, PPNC2 and PPNC5, it is suggested that the interaction between PP chains and clays were strong enough to increase the toughness of PP by reducing the formation of cavitations during deformation. On the other hand at a clay loading of 10 wt%, this was no longer the case. As the very obvious peak in the WAXS region shows at this concentration the clays are not fully exfoliated and formed tactoids which reduced the load shearing effect of clays hence reduced the toughness of the polymer [137]. The different scattering behavior of PP and PPNC10; and PPNC1, PPNC2 and PPNC5 suggests that the deformation mechanism in these two groups differ. While the deformation is mostly dominated by the formation of voids and crazes [128, 129] in the former group, it is mostly from the clays platelets load sharing contribution to the deformation of PP [93, 130] in the latter group.

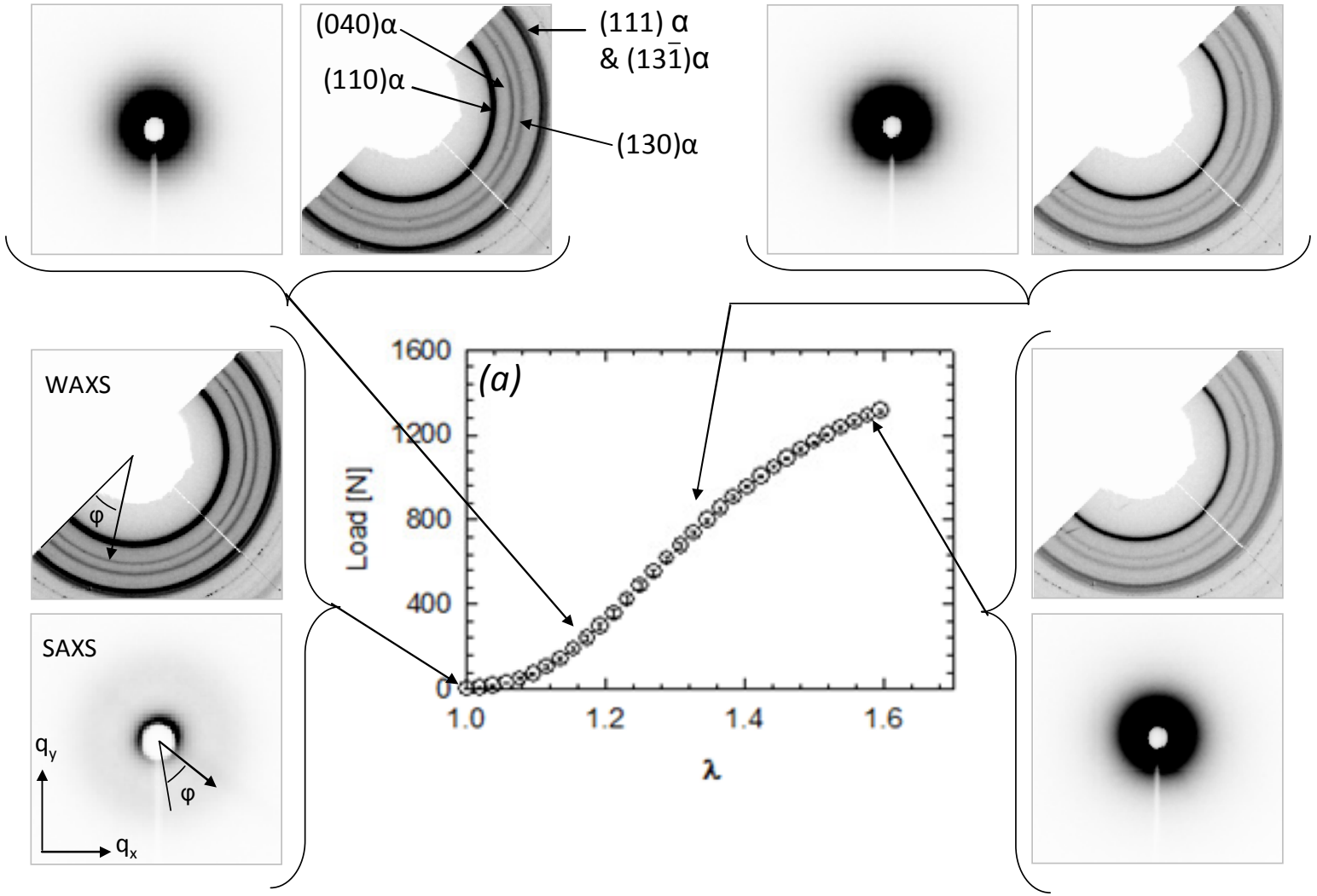

Figure 53. *In-situ collected 2D SAXS and WAXS images combined with ex-situ collected Load vs. λ curves for (a) PP and (b) PPNC10*

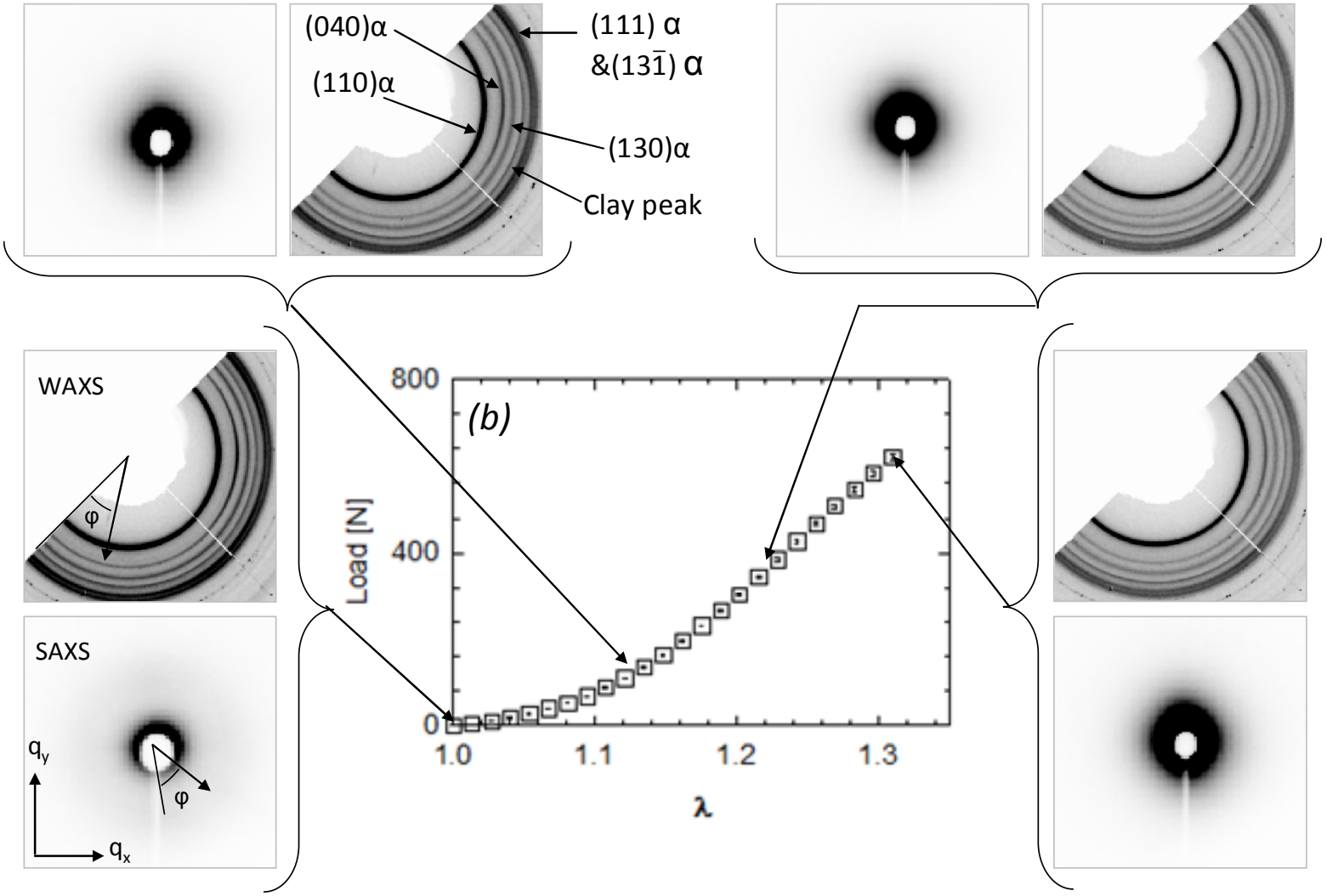

Figure 53 continued

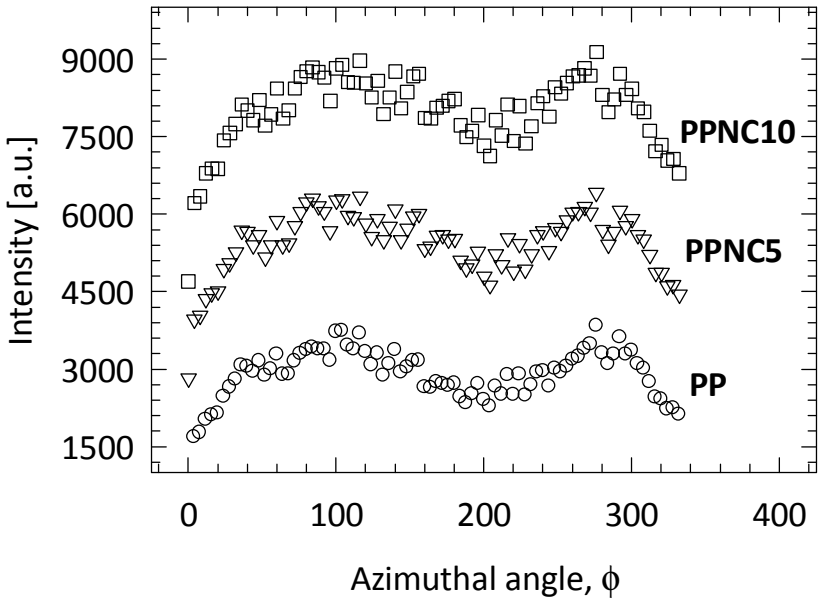

Figure 54. *Azimuthal scans over the SAXS peak at q=0.44nm^{-1} for the as made samples. Plots are shifted upwards for clarity.*

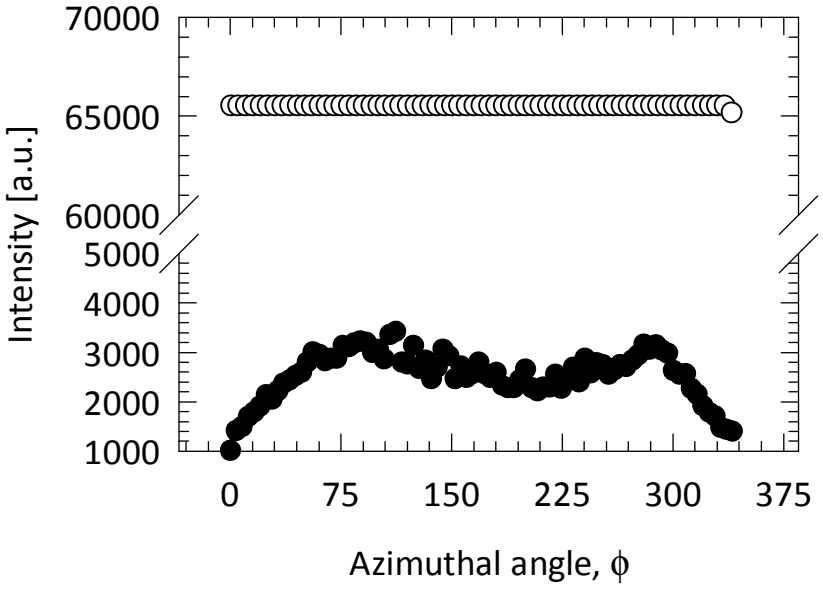

Figure 55. *Azimuthal scans over the q=0.44nm^{-1} in SAXS data for PP before deformation (●) and immediately after cessation of deformation (○).*

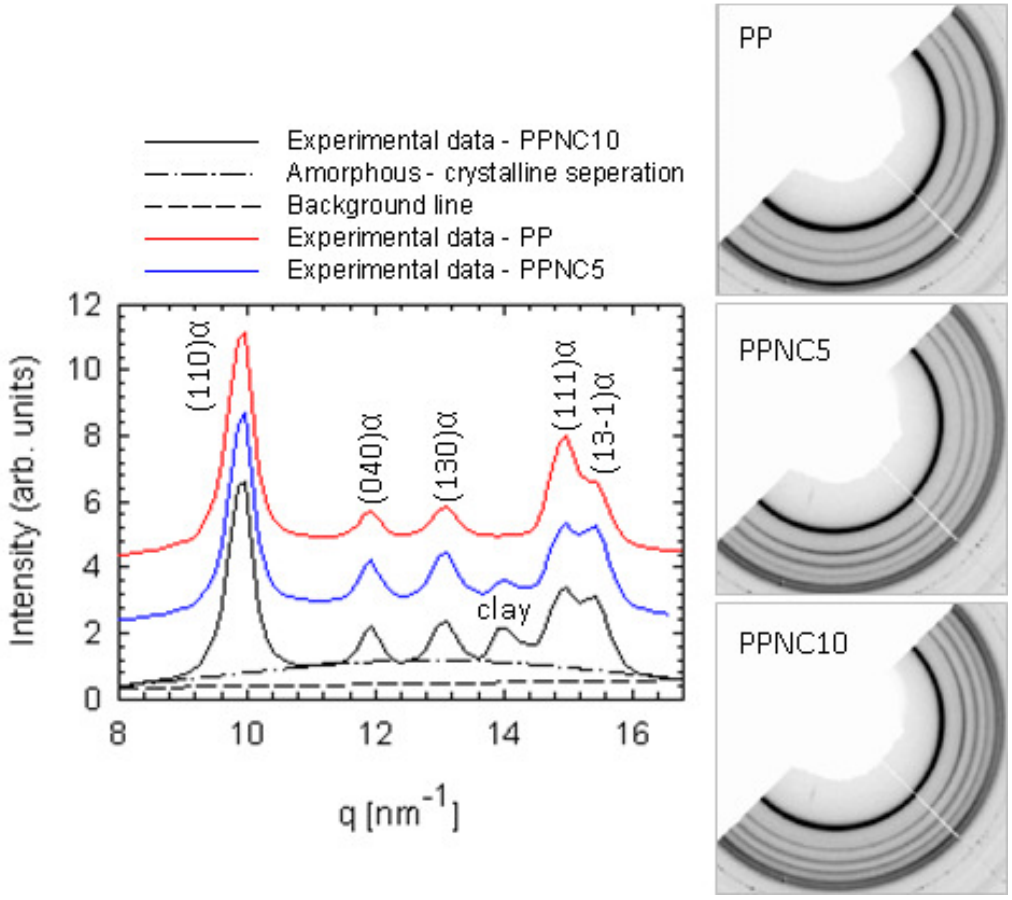

Figure 56. *1D and 2D WAXS data from PP and PPNC10.*

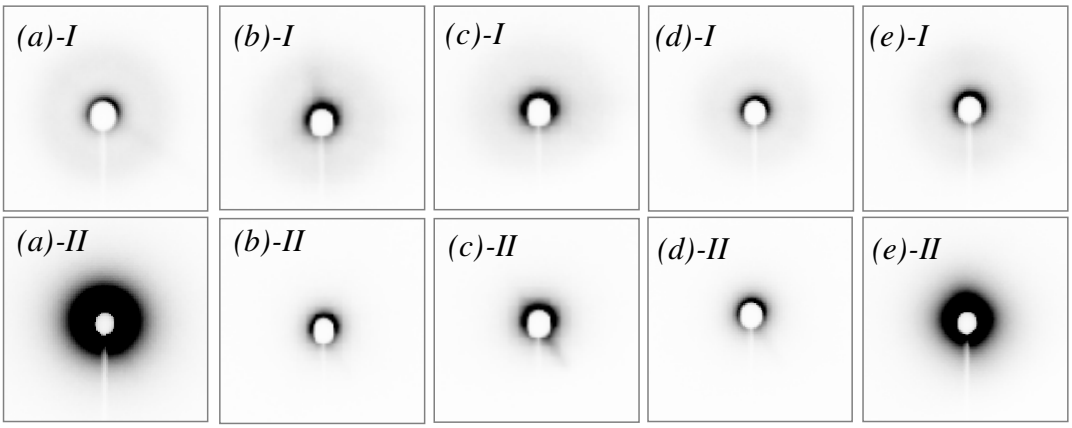

Figure 57. *2D SAXS images of (a) PP, (b) PPNC1, (c) PPNC2, (d) PPNC5 and (e) PPNC10 right before deformation (I) and immediately after cessation of deformation (II).*

6.3.1 Influence of temperature

Radially averaged SAXS plots of PP and PPNCs' show two distinct maxima at q positions of about 0.44 and 0.9 nm^{-1} at room temperature. These maxima are consistent with two different average lamella characteristic repeat thicknesses, of 14 and 7 nm, respectively. This morphology results from the cooling of polymer by chill rolls from one side, which creates a cooling gradient through the thickness of the polymer. *Figure 59* shows the stretch ratio dependence of the SAXS data of PP, obtained at RT and at 55°C, deformed at $0.0025s^{-1}$. With increasing deformation, at RT the dominant peak at q = 0.44 nm^{-1} shifts towards lower q values, reflecting an increase in characteristic repeat distance, reaching 17 nm at λ = 1.1. By contrast, no change in peak position is observed at 55°C due to the faster relaxations of the chains at high temperatures. Similar behavior was also observed for the PE and PE/clay nanocomposites under multiaxial deformation where the peak shift towards lower q values only at RT indicating and increase in the characteristic repeat distance [138].

One dimensional correlation function was used before to extract information from SAXS data including the amorphous and crystalline layer thicknesses as well as the overall repeat distance of PE in Chapter V. However, this method assumes lamellar stack morphology with variation of electron density along one dimension. Applying these methods of analysis to α-form of isotactic polypropylene is complicated as the organization of the lamellae can also exist in perpendicular to each other (see Figure 58) making one-dimensional correlation function is not reliable for the crosshatched morphology [139, 140]. Even so, information regarding the Bragg long spacing (d) was

extracted from SAXS data of PP and PPNCs by fitting Gaussian peaks to the experimental data.

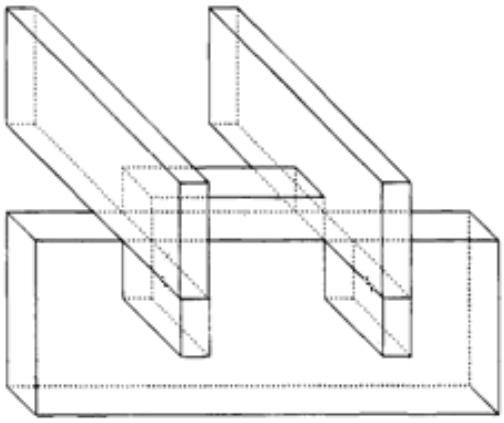

Figure 58. *Schematic of the cross hatched morphology of PP (Reproduced from [139]).*

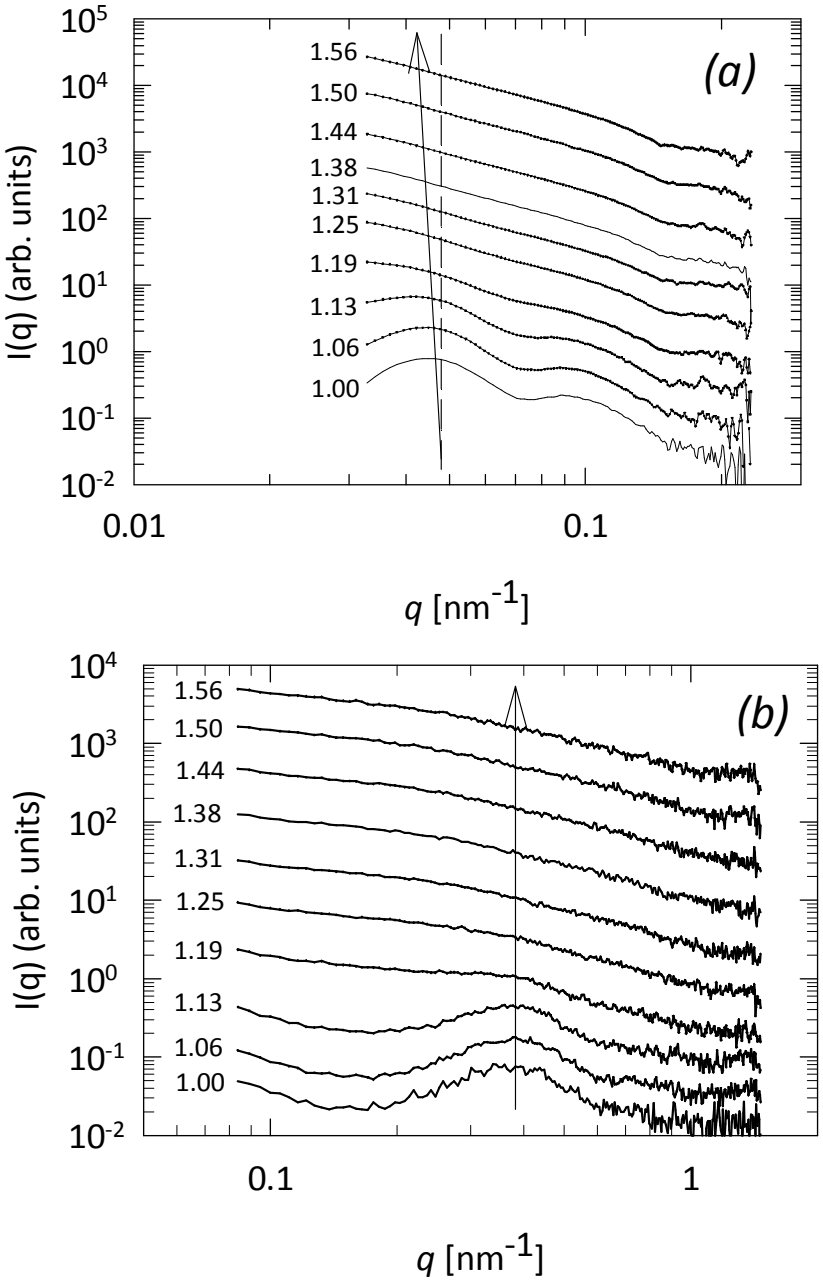

Figure 59. *1D SAXS plots of PP collected during multiaxial deformation at stsrain rate of 0.0025s^{-1} (a) at room temperature (b) at 55*℃*. Curves shifted upwards for clarity.*

Figure 60 summarizes the calculated values of *d* for PP and PPNCs with increasing strain at different temperatures. For clarity the figures only include data from

PP, PPNC5 and PPNC10. Figure 60 shows not only the importance of temperature over the characteristic lamellae long spacing, but that it becomes independent of strain at higher temperatures suggesting the amorphous chains have more freedom to move at this temperature and are able to distribute the stress without any global chain extension. On the other hand at room temperature, characteristic dimension increases with increasing strain which may be explained by the extension of the amorphous layers leading to separation of the lamellae [18]. The figures are limited to certain stretch ratio values, since at higher stretch ratios peaks are no longer visible and the scattering patterns remain effectively unchanged. Deformation is now occurring by drawing more material into the neck, in regions away from the X-ray beam. The loss in peak amplitude could result from either the lamellar stacks rotating into the strain direction and are therefore becoming increasingly perpendicular to the X-ray beam, or more likely from spherulite breaking up, causing a reduction in their average lateral dimensions. In addition, an increase in the scattering intensity at lower q region is observed, especially for PP and PPNC10, with increasing strain, which is believed to originate from void formation under strain as whitening of the samples is also observed with increasing strain.

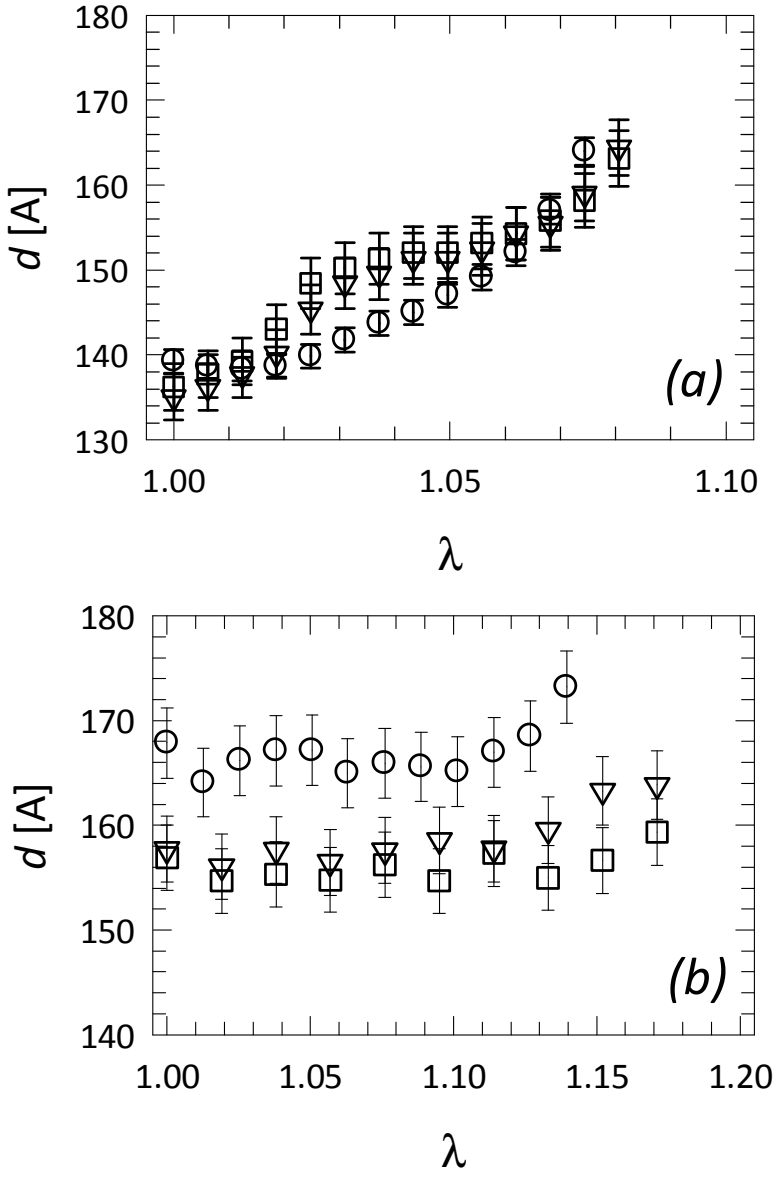

Figure 60. *Bragg long spacing (d) values of PP (circles), PPNC (triangles), and PPNC10 (squares) with respect to increasing strain (a) at RT, and (b) at 55ºC, strain rate at 0.0025s^{-1}*

Figure 61 shows WAXS patterns of PPNC5 during deformation at room temperature. It is observed that the diffraction intensities of the crystals decrease with increasing strain which was more obvious in PPNC1, 2 and 5. A strain induced melting [141] was observed in all materials especially in PPNC1, PPNC2 and PPNC5 during

deformation, detected from these reduced crystal intensities. The WAXS crystallinity index, X_c, is calculated from an azimuthally averaged pattern as follows:

$$X_c = \frac{I_c}{I_{total}} \tag{7}$$

where I_c is the integrated intensity of the crystalline peaks above the baseline and I is the total integrated intensity under the intensity curve (from both crystalline and amorphous components together) in the region of interest (ROI) [16]. A drop in the crystallinity index is observed with increasing deformation at both temperatures as shown in Figure 62. This decrease is in X_c is larger than that calculated values from DSC. However, it is important to note that the calculated values from DSC experiments were higher compared to WAXS data for the undeformed samples (see Figure 63). The reason for this is that the q range used for calculation of crystallinity was rather small. This decrease in the crystallinity could result from break-up of crystalline lamellae transformation causing increases in the amorphous phase [142, 143] or from rotation of crystals under strain and becoming more perpendicular to the incident X-ray beam.

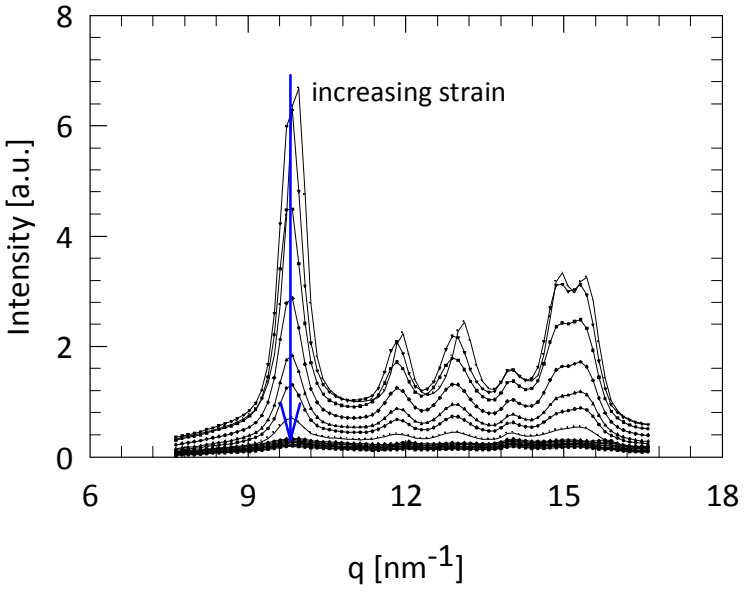

Figure 61. *WAXS plots of PPNC5 obtained during multiaxial deformation at RT at* $0.0025s^{-1}$.

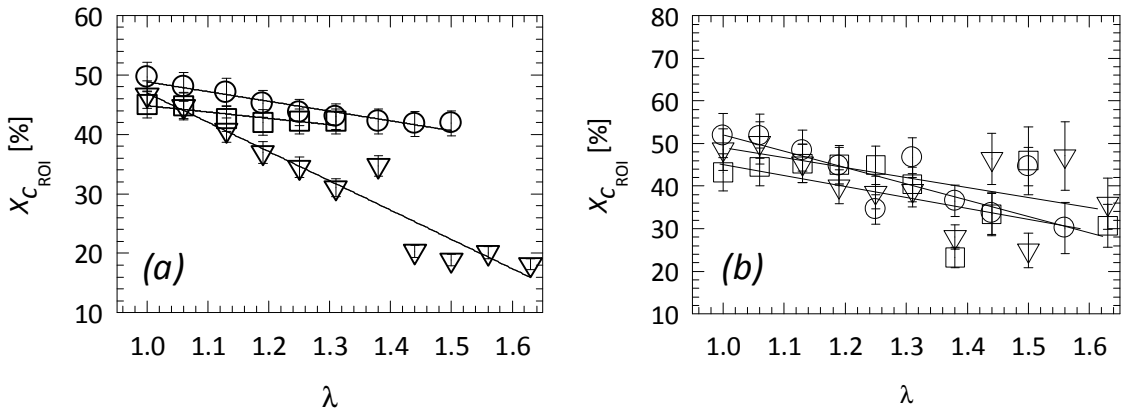

Figure 62. *Change in the crystallinity index* (X_c) *with respect to increasing strain when deformed at (a) RT, (b) 55℃. Lines are guides to the eye only.*

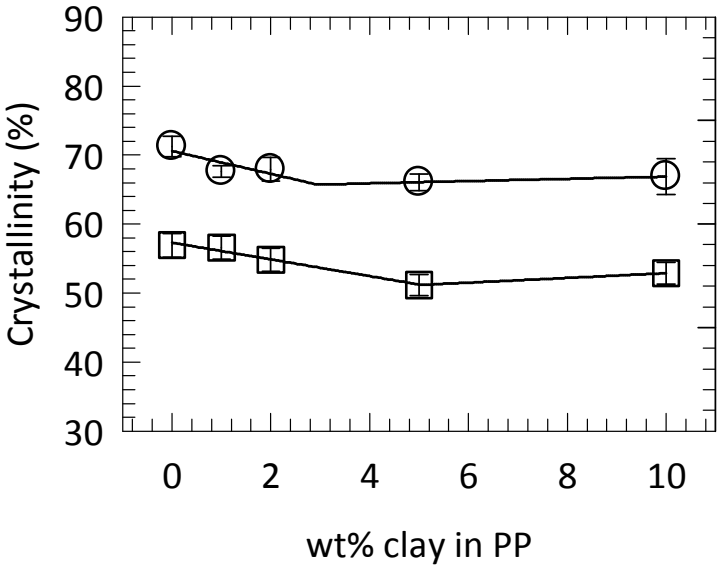

Figure 63. *Crystallinity values calculated for PP and PPNCs from DSC experiments where (o) and (□) denote before and after deformation, respectively. Lines are guide to the eye only.*

6.3.2 Influence of strain rate

Changes in the characteristic repeat distance with increasing strain are shown in Figure 64 for PP and PPNCs at two different strain rates where at higher rate fewer points were captured due to the capture rate of the detectors hence less data points are presented. Figure 64 shows that the rate of increase in the characteristic repeat distance, consequently the stretching in the amorphous chains, was not affected by the rate of the deformation and reached a constant value over the same amount of stretching for the PPNCs. On the other hand this was not the case for PP where an increase in the deformation rate caused a greater increase in the overall repeat distance compared to slower strain rate. This greater increase in the overall repeat distance in PP at higher strain rate is believed to be due to the amount of time that the amorphous chains get

during deformation to rearrange themselves was quite short hence the degree of freedom that the chains have is low which resulted with further increase in the long spacing. Inclusion of clays seems to reduce the observed effect at higher strain rate probably by clays effect of absorbing the additional energy introduced at higher strain rate by the aforementioned cooperative motion of clays [144] and amorphous chains which resulted a smaller rate of increase in the long spacing. This affect was unrelated from the amount of clays as at all clay loadings the rate of increase in *d* was quite similar at both rates.

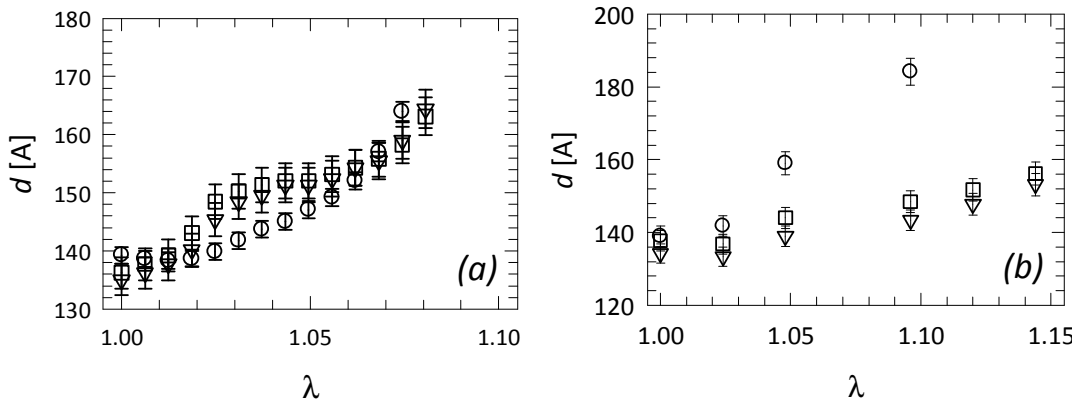

Figure 64. *Bragg long spacing (d) values of PP (circles), PPNC5 (triangles), and PPNC10 (squares) with respect to increasing strain at room temperature at strain sates of (a) 0.0025s^{-1}, and (b) at 0.025s^{-1}.*

By monitoring the change in full width at half maximum (FWHM) of the crystal peaks with increasing strain, it is possible to determine whether macroscopic stress leads to microscopic stress distribution within the crystal structure by effecting the size of the crystallites. In the case of deformation at room temperature variations in FWHM may be considered as an indication of the homogeneity of stress distribution [16]. Figure 65 shows the change on the FWHM at room temperature measured at two different strain

rates for the (110) and (040) reflections with increasing strain. Initially a slight increase in the FWHM of the both peaks is observed at both strain rates, reaching an asymptotic value at $\lambda = 1.1 - 1.2$ for both at $\overset{*}{\gamma} = 0.0025 s^{-1}$ and at $\overset{*}{\gamma} = 0.025 s^{-1}$ indicating a slight distortion in the crystal structure. Towards higher stretch ratios FWHM remained unchanged. In this asymptotic region a homogenous distribution of the multiaxial deformation is produced by pulling more material to the deforming region. One interesting observation was that the FWHM of PPNC10 (040) crystal remained unchanged when deformed at faster strain rate. This may indicate that the stress distribution in PPNC10 at this rate was less homogeneous compared to PP and the other PPNCs. FWHM can also be used as an indicator of the changes in the crystallite sizes (D_{hkl}):

$$D_{hkl} = \frac{\lambda}{\beta_{hkl} Cos\theta_{hkl}} \tag{8}$$

where β_{hkl} is the FWHM and θ_{hkl} is the scattering angle. Capt *et. al. [91]* have discussed that with increasing stretch ratio for biaxially stretched PP the FWHM increased consistent with a reduction in the size of (040) crystals domains of PP at elevated temperatures. The calculated values of D_{040} (~11.1 nm) corresponds to an average size of the crystallites that are oriented parallel to the film plane. Figure 65 suggests that with increasing strain D_{040} decreases (to ~9.45 nm) since FWHM increases at both strain rates with a similar rate. This decrease is probably caused by the chain slip mechanism and breaking up of lamellae into smaller pieces supported by deformation of amorphous

phase by interlamellar sliding which was observed before under simultaneous and sequential biaxial stretching of PP [91, 145].

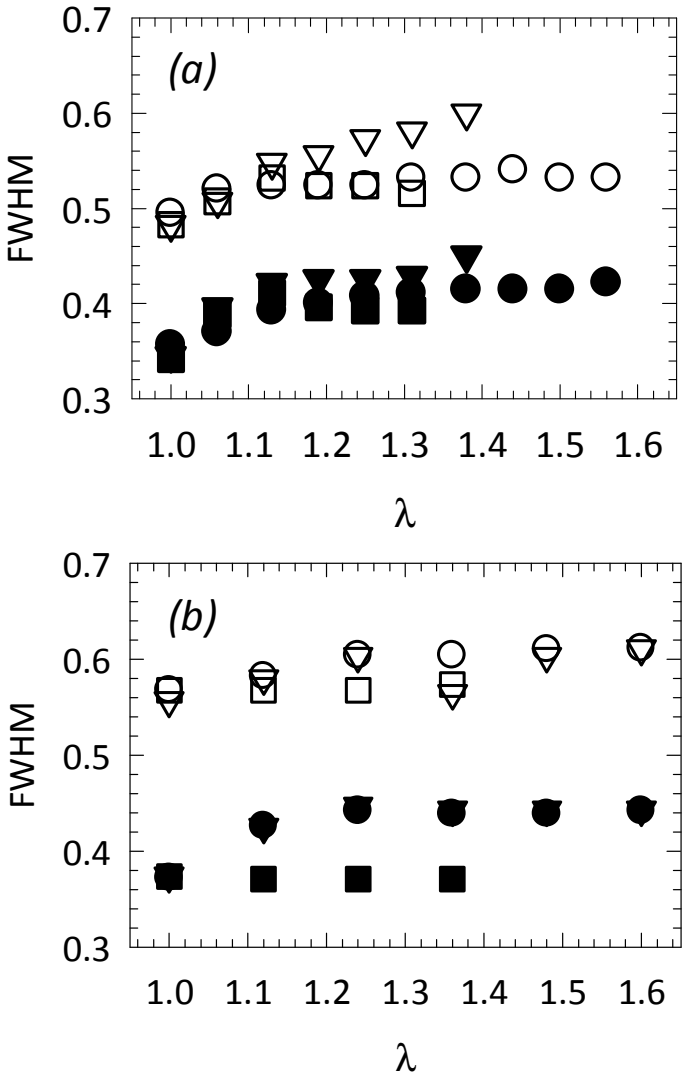

Figure 65. *Change in FWHM of (110) (unfilled symbols) and (040) (filled symbols) reflections with respect to increasing strain at room temperature at (a) 0.0025s-1 and (b) 0.025s-1, for PP (circles), PPNC5 (triangles) and PPNC10 (squares)*

Herman's orientation function (*f*) is a common method of monitoring the change in the orientation of the crystallites under uniaxial deformation, and the effect of fillers in

the orientation of crystallites [132]. Under uniaxial deformation, f is determined by taking the drawing direction as a reference. However in multiaxial deformation there is no reference point similar to that. Therefore instead of calculating f, we have monitored the change in the azimuthal intensity with respect to increasing strain to observe any changes in (110) and (040) crystals' orientation with respect to their initial state as well as the effect of clay platelets on reorganization of crystals. Figure 66 shows the azimuthal scans of PP and PPNC10 during deformation at strain rates of $0.0025s^{-1}$ and $0.025s^{-1}$, respectively. The maximum deformation at $0.0025s^{-1}$ is λ=1.3 where it is λ=1.36 for $0.025s^{-1}$, which were the limitations for PPNC10 during in-situ experiments. Neat PP shows a very slight azimuthal peak compared to PPNC10 suggesting that the (110) crystals are almost isotropically oriented in the sample. On the other hand, more obviously observed azimuthal peak in (110) crystals for PPNC10 suggests that the existence of clay platelets cause a preferential orientation of the (110) crystals of PP, which does then not dissipate over the course of deformation at neither strain rates. The initial preferential orientation was most likely caused by the confinement effect of clay platelets and did not dissipate strain again for the same reason.

Similar analysis was performed on the clay peak to monitor the changes in the clay orientation. As shown in Figure 67 neither an orientation was observed initially nor did any changes occurred over the course of deformation on the azimuthal scans of peak associated with Cloisite® 15A clays. Scherer's equation was also used to calculate the size of the clay tactoids occurring in PPNC5 and PPNC10 by fitting Lorentzian curves to the clay peaks with respect to increasing deformation. The FWHM was calculated and the

crystal size was determined to be 10.81nm. The calculated crystal size was constant showing no dependence to the applied strain in both PPNC5 and PPNC10.

Comparison of the effect of temperature, 55℃, was not possible since these measurements were taken at DLS where a line detector instead of an area detector was employed.

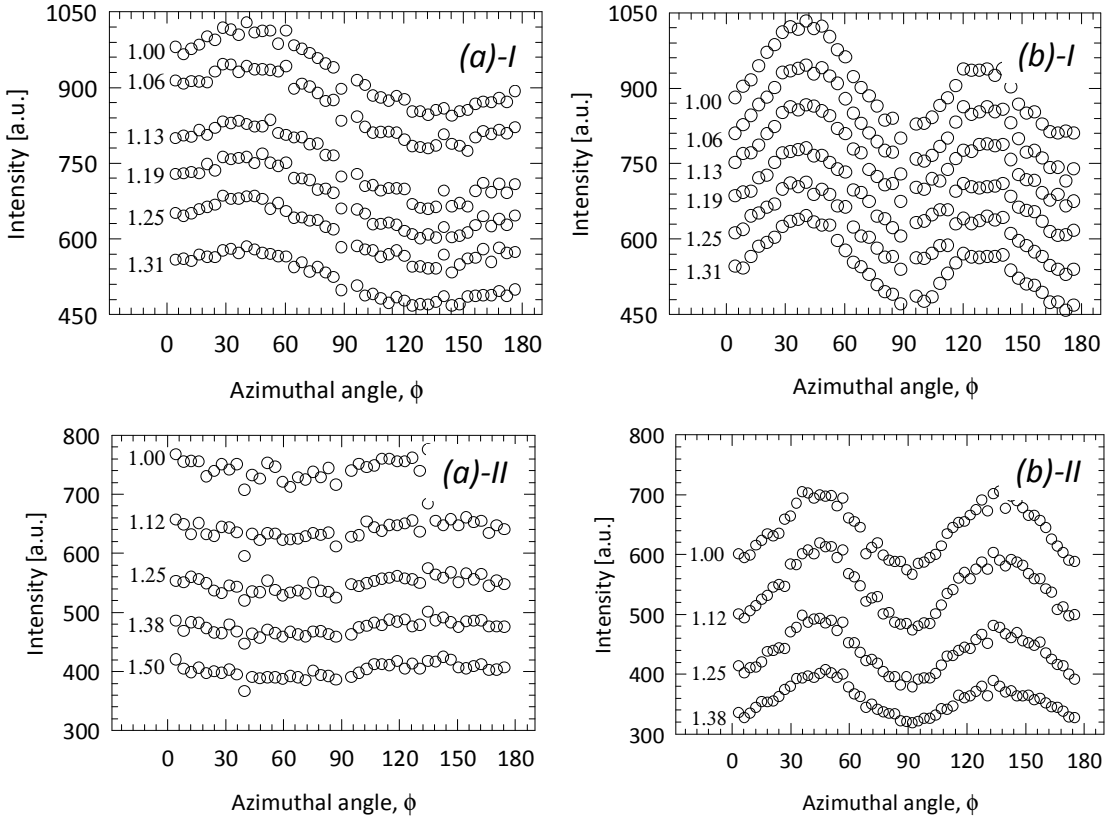

Figure 66. *Change in the azimuthal cans of (110) crystal with respect to increasing deformation (as indicated) at room temperature for (a) PP and (b) PPNC10; (I) 0.0025s^{-1} and (II) 0.025s^{-1}*

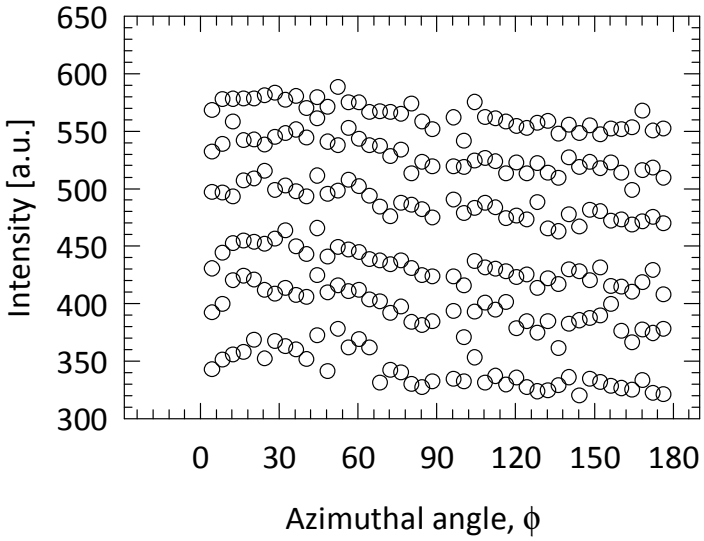

Figure 67. *Azimuthal scans of the clay pea with respect to increasing strain (as indicated) in PPNC10 at RT at 0.0025s^{-1}.*

6.4 Effect of shear deformation

The measurement of rheological properties of polymeric materials in the melt state is essential to gain a fundamental understanding of the processibility of that material. In the case of polymer/clay nanocomposites, the measurements of rheological properties are not only important to understand the knowledge of the processibility of these materials, but are also helpful to determine the structure-property-processing relationships in nanocomposites. This is because rheological properties are strongly influenced by their nanoscale structure and interfacial characteristics. It is instructive to study the rheology of polymer/clay hybrids for two reasons. First, rheological properties are indicative of melt-processing behavior in unit operations such as injection molding. Second, since the rheological properties of particulate suspensions are sensitive to the structure, particle size, shape, and surface characteristics of the dispersed phase.

Rheology potentially offers understanding of dispersion of nanocomposites directly in the melt state. Thus, rheology can be envisaged as a tool that is complementary to traditional methods of materials characterization such as electron microscopy, X-ray scattering, dynamic mechanical analysis, and mechanical testing.

In melt rheological tests, initially a dynamic strain sweep test was applied to the nanocomposite samples in order to characterize strain dependence of the viscoelastic properties of the samples and determine the linear viscoelastic region (LVR). The dependence of the complex viscosity (η^*) on the shear strain (γ) at frequency (ω) = 1 Hz for the samples is shown in Figure 68. Comparison of the linear viscoelastic response of neat PP and the nanocomposites shows the significant effect of the clays, particularly at low frequencies. The complex viscosity of all the samples exhibits a linear region (Newtonian plateau) at low strains and a non-linear region at high strain amplitudes. It was observed that the plateau modulus readily increases with the clay amount at a fixed strain showing a more solid-like behavior as the solid dispersed phase of clays strongly influences the melt behaviors at low strains [73, 146]. The viscosity deviates from the linear to non-linear viscoelastic behavior in a limited strain region the value of which is dependent of clay content. The linear viscoelastic range of the nanocomposite samples is lower than that of neat polymer. The LVR range decreases with increasing clay content. The network structure of the sample stems from the presence of entanglements of amorphous and ordered crystalline domains in the PP. This network structure sustains in large deformations in strain sweep experiment in the neat PP. On the other hand in the nanocomposites, layered platelets decrease the entanglement density of amorphous chains

and the network structure becomes weaker which does not resist large deformation like neat PP [147].

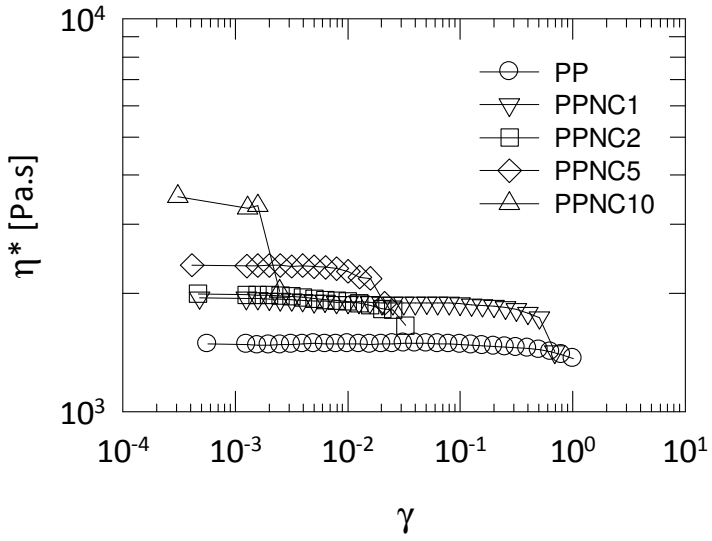

Figure 68. *Variation of complex viscosity as a function of strain for PP and PPNCs.*

The storage modulus (G'), loss modulus (G") and the crossover frequencies of G' and G" for PP and PPNCs are shown in Figure 69. Over the entire frequency range studied the storage and loss modulus of the nanocomposites are substantially higher than that of PP. The storage modulus and loss moduli increase with increasing frequency for all the samples studied. This occurs because at low frequency, the time scales are large enough to unravel the entanglements so that a large amount of relaxation occurs resulting in a low value of storage and loss modulus. However, when a polymer sample is deformed at higher frequencies the entangled chains do not have time to relax, so the modulus goes up. There is a linear drop in the crossover frequencies of PPNCs with

increasing clay content showing that the elasticity of the composites increase with increasing clay as expected.

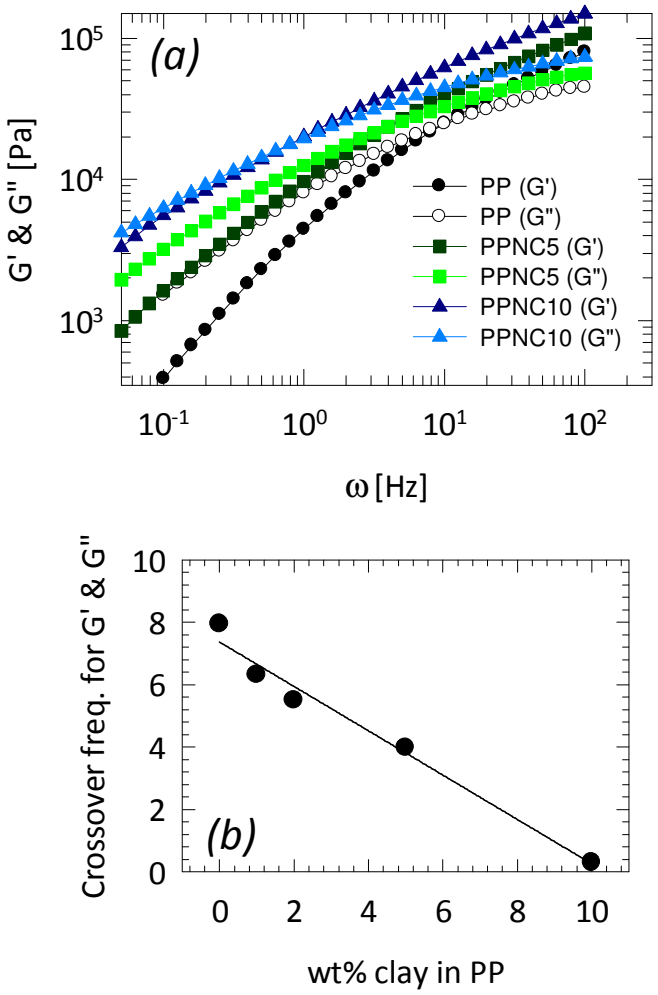

Figure 69. *Variation of G' and G" as a function of frequency and, (b) Cross over frequencies for G" and G" for PP and PPNCs*

The change in complex viscosity (η^*) of nanocomposites and the neat PP as a function of frequency is shown in Figure 70. The complex viscosity decreases with increased frequency due to the strong shear thinning behavior of the polymer and the nanocomposites. The viscosity of the nanocomposites is higher than the neat PP. The

shear viscosities of the nanocomposites increase monotonically with clay loading. The intercalated nanocomposites display a more pronounced shear thinning behavior which is observed at lower shear rates with increasing clay content. In other words, at low shear rate, the addition of very small amounts of clays results in a significant enhancement in the shear viscosity. At high shear rates, however, the shear viscosities for the nanocomposites are comparable with or even lower than that of the pure PP as a result of the preferential orientation of the clay layers or even anisotropic tactoids that are parallel to the flow direction. The increment of melt viscosity of the nanocomposite is attributed to the strong interaction of clays and PP matrix [147, 148]. Moreover, viscosity curves at low frequency region could be fitted by the power law model. Several authors have used η* curves to determine power law parameters and explain shear thinning behavior of the polymer nanocomposites at low frequency region [149, 150]. For the frequency sweep data, power law expression is written as:

$$\eta^* = k\omega^n \tag{9}$$

where η^* is dynamic viscosity, k is a sample specific pre-exponential factor, ω is the oscillation frequency in the frequency sweep test and n is the shear thinning exponent. k and n can be directly determined from the logarithmic plot of η* vs. ω as:

$$\log(\eta^*) = \log(k) + n\log(\omega) \tag{10}$$

Shear thinning exponent, n, is the slope of straight line obtained by plotting $log(\eta^*)$ vs. $log(\omega)$ and it is a semi-quantitative measure of the clay dispersion in polymer phase. Power law exponents were listed in Table 12. Values suggest that the exfoliation of clays were quite similar except PPNC2 which reached a better exfoliation degree compared to the other nanocomposites. For comparison purposes the n value of PP is also included

which is very small as frequency independent behavior is expected from the neat polymer at very small frequencies.

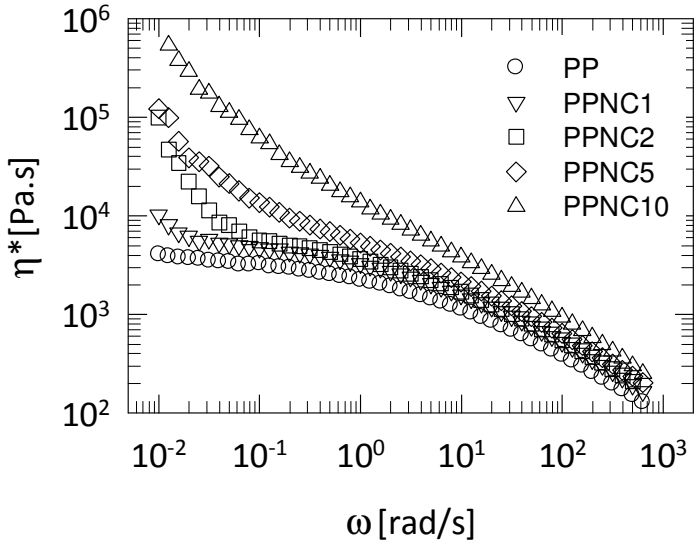

Figure 70. *Variation in complex viscosity as a function of frequency and the terminal slope of the curves for PP and PPNCs at low frequency region.*

Table 12. *Calculated shear thinning exponents for PP and PPNCs.*

Sample	-n	R^2
PP	0.107	0.958
PPNC1	0.918	0.996
PPNC2	1.927	0.971
PPNC5	1.262	0.928
PPNC10	1.273	0.974

Time sweep experiments are important by providing the necessary information about how a material changes with time when testing materials that may undergo macro- or micro-structural rearrangement with time. These rearrangements directly influence rheological behavior. Results from transient flow experiments for PP and PPNCs at two

different shear rates are shown in Figure 71. At both rates PP, PPNC1 and PPNC2 shows shear thinning behavior with increasing time of shearing indicating a matrix dominated behavior. On the other hand, time-dependent behavior of PPNC5 and PPNC10 build up of solid-like, shear thickening characteristics. The decrease in the viscosity provides an evidence for the disentanglement of polymer chains. At higher filler loadings, the effect of the filler structure dominates the flow so that an increase in the viscosity was observed. Similar observations in polycarbonate reinforced with glass beads was reported before where the existence of fillers dominate the structure in the melt shearing state and cause a more solid-like behavior [151]. The increase in the viscosity with shear flow as a function of time indicate that either anisotropic clay domains or PP crystallites or both are flow-aligned at these shear rates [4, 152]. It was suggested that for clay loadings in excess of 6.7 wt.% the clay tactoids form a percolating network as a result of physical jamming, which then offers considerable resistance to deformation and hence solid-like behavior [153]. It was also postulated that flow-induced alignment or shear orientation of the clay occurs at higher strain which then results in an increase in viscosity [153, 154].

From Figure 71, it can be seen that both the shear thickening of PPNC5 and PNC10, and the shear thinning of PP, PPNC1 and PPNC2 are more pronounced when the frequency is lower. It takes almost two times longer for the shear thickening and thinning to start at 1 Hz compared to 10Hz. This shows that at higher frequencies the alignment of clays and/or the crystal domains does not occur so efficiently since they have less time to rearrange themselves with respect to shearing. At lower frequencies, on the other hand, the structures can rearrange themselves more efficiently resulting in a more pronounced shear thickening effect.

Based on these observations, it can be said that at lower clay loadings the matrix PP dominates the processibility of the materials hence the melt processing of PP, PPNC1 and PPNC2 will be very similar. This would mean that PPNC1 and PPNC2 may not require any adjustments of processing conditions compared to pure PP. In injection molding processes for example, smaller viscosity in the melt state results with filling the mold cavities better, on the other hand the loss of melt strength requires the material to be processed at lower temperatures to preserve consistency, sagging and degradation [155]. For the case of PPNC5 and PPNC10, however, shear behavior is dominated by the clay particles consequently with increasing processing time, the viscosity of the materials increases. This may require adjustments to the processing of higher clay loaded polymers, such as increased processing temperature or increased rate of shear, as at higher rates the increase in viscosity is as strongly pronounced as at lower rates. Conversely, this behavior would be advantageous in for instance human protection applications, that require energy absorbing mechanisms so in these cases responsive fluids have been used which transforms from low to high viscosity under an imposed deformation field [156].

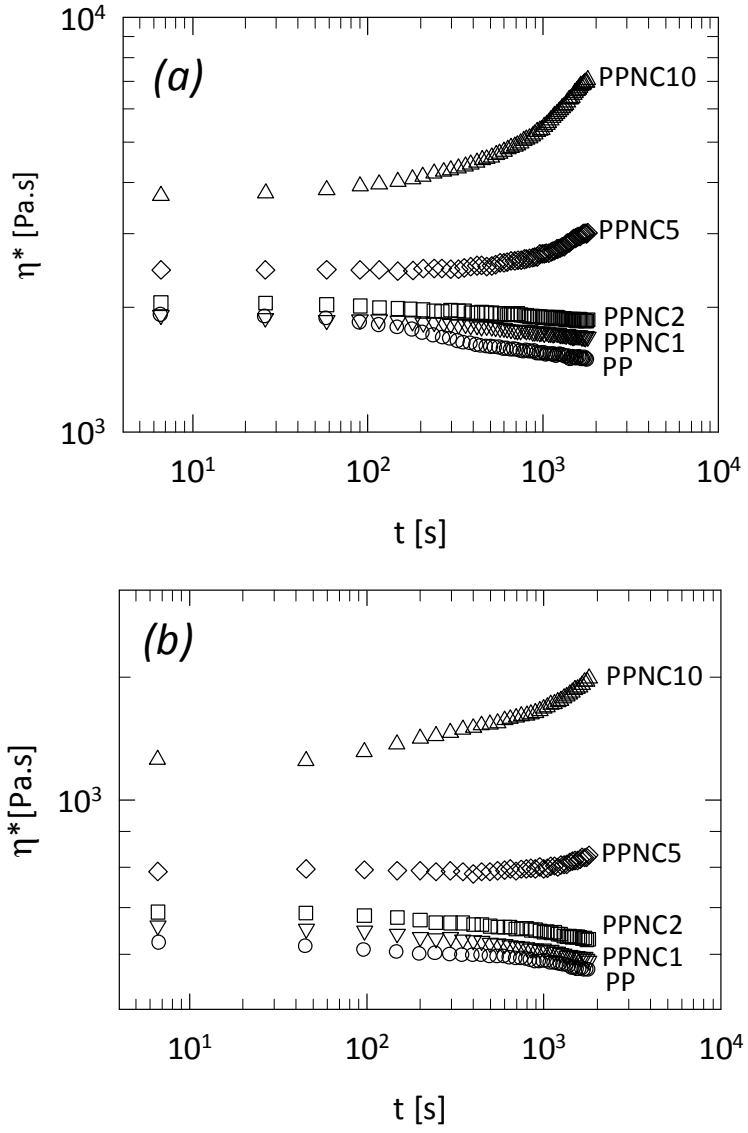

Figure 71. *Time dependent viscosity of PP and PPNCs at 180℃ measured at (a) 1Hz and (b) 10Hz frequency.*

6.5 Time dependent recovery after multiaxial deformation

SAXS data from PP and PPNC samples were collected after the stress was fully removed from the multiaxially deformed samples to see the effect of time dependent recovery on the morphology of PP (see Figure 72). As mentioned before there is

anisortopy in the PP and PPNCs which disappears with increasing deformation at room temperature and at 55C. Scattering from samples relaxed for 3, 4 and 5 weeks were collected to track any changes in the PP morphology during recovery time. Compared to uniaxial deformation of PP [141] where the periodicity of lamella was observed to fully recover, different behavior in PP following multiaxial deformation is observed. As shown in Figure 72, it was observed that there is no difference in the scattering data of PP and PPNCs between immediately after cessation of deformation ($\lambda = 1.38$) and the data from relaxed sample for 3 weeks. Neither a change is tracked with increasing time of recovery in PP, PPNC5 and PPNC10. These observations are quite different from PE where full recovery in the ordering was only seen after 5 weeks of recovery time in both PE and PENCs. Although these two polymers are very similar to each other in terms of chemistry and properties; recovery behavior from multiaxial deformation of the two systems are quite different. PP and PPNCs do not recover their initial ordering like PE and PENCs did. The reason PP system did not recover may result from requiring longer times than 5 weeks for full recovery.

On the other hand, although no significant transformations were observed in the WAXS scattering for PP and PPNC10, recovery of PP crystal chains and clays were quite monotonic (see Figure 73) that the crystal peak intensities partially grow back in time. A strain induced melting [141] was observed in PPNC5 during deformation, detected from the reduction in crystal peak intensities, was observed to recover back to initial morphology in 3 weeks. After 4 and 5 weeks recovery times no additional recovery was detected.

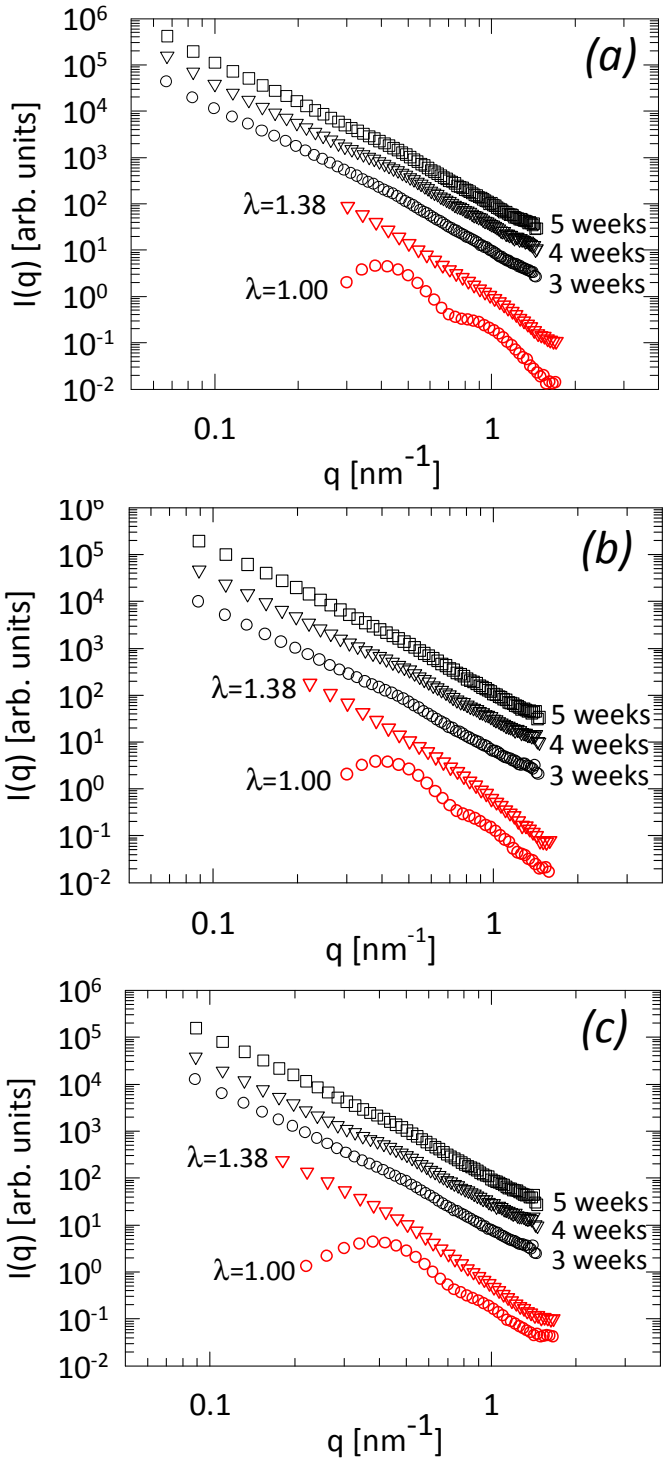

Figure 72. *1D SAXS profiles of (a) PP, (b) PPNC5 and (c) PPNC10 where red marks denote in-situ collected data and black marks for data collected after relaxation as indicated.*

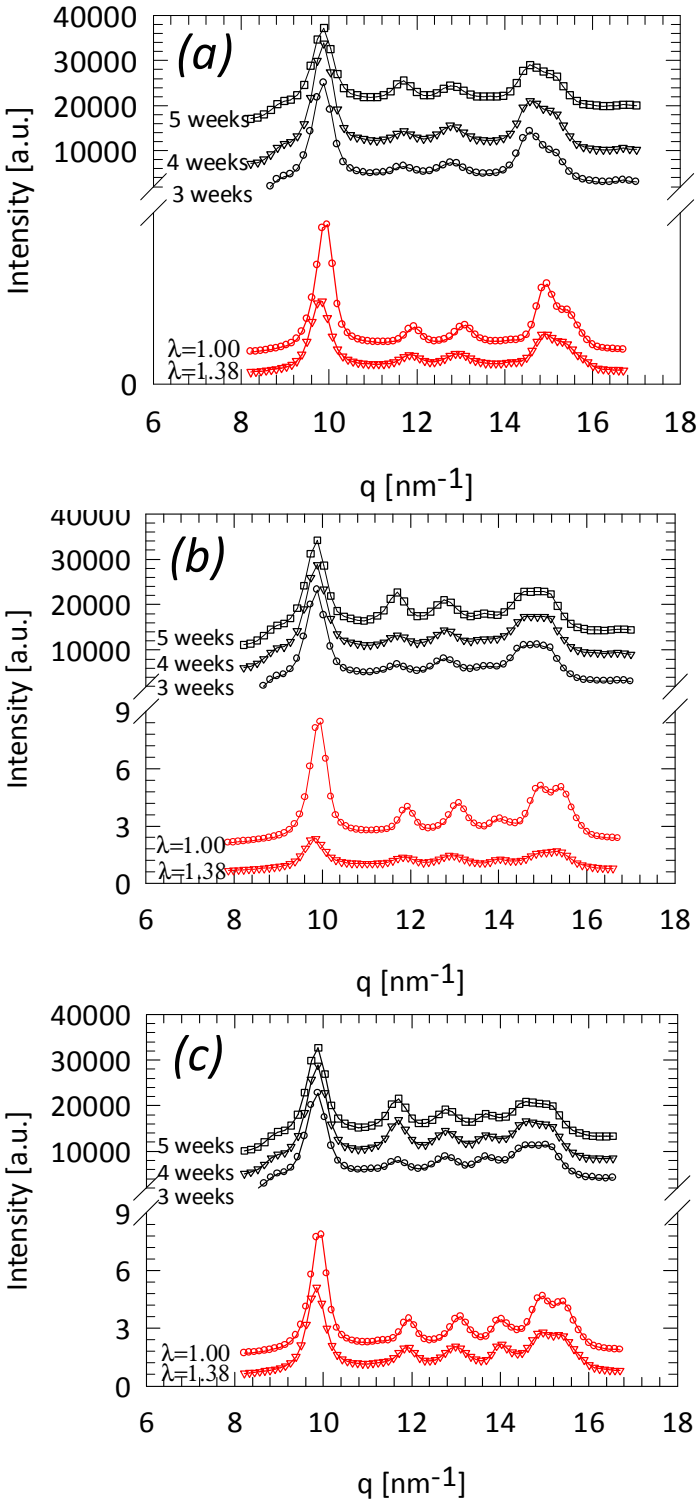

Figure 73. *1D WAXS profiles of (a) PP, (b) PPNC5 and (c) PPNC10 where red marks donote in-situ collected data and black marks are for data collected after relaxation as indicated.*

CHAPTER VII

CONCLUSIONS AND RECOMMENDATIONS FOR FUTURE WORK

7.1 Conclusions

The overall objective of this work was to contribute to the design of polymer/clay nanocomposites with desired properties for specific applications by building an understanding of structure-processing relationship of these materials. In that perspective real time structural changes in high density polyethylene and its clay nanocomposites; and polypropylene and its clay nancomposites during multiaxial deformation was studied on the molecular and supramolecular scales with simultaneous *in-situ* small and wide angle x-ray scattering techniques for the first time. The structural changes which occur under multiaxial loading are more complex than those in uniaxial. Although PP and PE are polyolefins and as such possess similar properties and end-use areas, the multiaxial deformation of these two polymers and their clay nanocomposites have shown similarities but also significant differences. This section of the dissertation summarizes both the similarities and differences in the *in-situ* multiaxial deformation behavior of PE and PP.

The general observation from the multiaxial deformations of nanocomposites was the fact that once the clay is added there are some changes happening to the morphology evolution of the polymer during deformation. However the increase in the amount of clays up to 6 wt% in PE and 5 wt% in PP did not alter the deformation behavior of the

polymer compared to lower clay loadings; 3wt% in PE and 1, and 2 wt% in PP. This suggests that it is possible to enhance the mechanical, thermal and barrier properties of these polymers by adding more clay without too much sacrifice in the processibility of the polymer.

In addition our work has shown that both the enhancement in the mechanical behavior and the morphology evolutions during deformations are quite different under multiaxial and uniaxial deformations for the materials used. Although there is a systematic enhancement in the uniaxial mechanical properties of PE and PP, under multiaxial deformations the enhancement is not directly correlated with increasing clay content. Nanocomposites tend to deviate from this linear relationship in the mechanical strength and strain hardening under multiaxial deformations, with increasing clay content in the polymer. These observations suggest that one cannot directly correlate the tensile or uniaxial deformation properties and morphology change during deformation with those more complex biaxial and multiaxial deformations. Such deformations require specific observations of their own.

The scattering patterns of PE and PENCs have shown an anisotropic structure, which is an indication of the orientation caused by the film forming extrusion process. On the other hand, the scattering patterns of PP and PPNCs showed that the film extrusion process only slightly changes the morphology as the scattering patterns of as made samples were slightly anisotropic in both the SAXS and the WAXS regimes. Although the initial scattering patterns of PE and PENCs were quite anisotropic, multiaxial deformation removes the initial orientation and the scattering patterns became increasingly more isotropic with increasing stretching, while PP and PPNCs' overall

orientation also observed to become more isotropic with increasing deformation. In both systems whitening of the sample as well as increased scattering in the small angle regime indicate the formation of voids and crazes. In PP system, this increased scattering was more obvious in neat PP and PPNC10 compared to other PPNCs showing that the high degree of clay exfoliation is responsible for reducing the formation of voids in PP, unlike PE where no similar difference with clays were observed.

Both polymers and their nanocomposites exhibited an increase in the characteristic repeat distance of lamellar stacks with increasing multiaxial stretching. This was attributed to the stretching in the amorphous component of the polymer. This increase in amorphous layer thickness was more pronounced at room temperature, while at 55C with increasing strain no change in overall spacing was observed for either system (PE-PENCs and PP-PPNCs). This can be attributed to the faster relaxations of amorphous chains at this increased temperature. The growth rate in lamellar spacing reached its highest values in the case of PENC compared to PE, while PP and PPNCs showed very similar rates of change. This suggests that the interaction between the PE and clays were weaker than the interactions between PP and clays since the bigger amorphous layer thicknesses obtained in PENCs was suggested to be affected by polymer-clay interfacial de-bonding. The highest value of amorphous layer thickness reached was higher at the highest rate of deformation compared to the lower rate. This was again more pronounced in PENCs than the neat PE, supporting the hypothesis of polymer-clay interfacial de-bonding. At higher temperatures, however, this effect was eliminated due to increased chain freedom to move.

In the PE system stable orthorhombic crystalline structures dominated when the extruded films, while in the PP system more stable α-crystallines were formed. The existence of clays was observed not to alter the as made polymers' most stable forms. With increasing deformation in PE systems, there is an increase in the amount of meta-stable monoclinic crystallites at the expense of the amount of orthorhombic crystallites. The existence of clays caused formation of less monoclinic crystallites in PE, while the amount of clay did not effect the formation of monoclinic crystals as only slight differences were observed between PENC3 and PENC6. The amount of monoclinic crystal phase formed at room temperature was higher than at 55C, in addition to the fact that the onset of monoclinic crystal formation was delayed at 55C. This shows that metastable monoclinic phases are formed more readily at room temperature. Increase in rate of deformation accelerated the formation and growth of monoclinic crystal phase.

For the PP system, no transformation between different crystal phases was observed under deformation. However as mentioned earlier, slight orientation of crystals was detected especially with increasing clay content showing that clays contribute to the crystalline organization by helping crystals to align in the extrusion direction. It was seen that multiaxial deformation reduced the anisotropy of the as made PPNC samples and made the scattering more isotropic. While no change detected in the crystallinity of PE system before and after deformation, slight reductions in the PP system was observed. This could result from the amount of strain put in PP system.

It was observed that PE system needed a shorter recovery time compared to the PP system, where in 3-5 weeks all the PE and PENC samples returned to their initial morphology as observed by their scattering. The recovery rate was faster in neat PE

compared to PENCs due to the clay acting to prevent the PE chains to recover. On the other hand PP system showed no recovery either in the SAXS regime after recovery. This could be result of higher strains applied to PP, as the clays did not alter the recovery of PP. Partial recovery of the α-crystals was detected in the WAXS regime after recovery.

Although both polyolefins, *in-situ* observations of PP and PE as well as the time dependent recovery behaviors have shown that more detailed and specific approaches should be applied to different nanocomposites systems with different matrices. The effect of clays in the multiaxial deformation of polymers could change from polymer to polymer even when they are very similar such as PE and PP.

In addition to uniaxial, multiaxial and biaxial deformations, effect of shear was investigated. Existence of clays in the polymer was seen to change the response of the polymer to the melt flow conditions especially at higher clay loadings. An increase in the viscosity with increasing time of shearing was observed in PPNC5 and PPNC10 which may require some alterations to the melt processing conditions of these polymer/clay nanocomposites.

7.2 Recommendations for future work

As previously mentioned, polymer clay nanocomposites offer a variety of advantages over their conventional counterparts which is the reason these materials attract a great interest in research. Although there is great deal of research on the structure-property relations of these materials, still very little known about how these materials reach their characteristic forms during processing. Neither there is a model that allows one to design a nanocomposite and a processing route with specific properties for

specific applications. With this work we have contributed to the missing part in this area with working on structure-processing relationships of polymer/clay nanocomposites.

Our studies have shown that uniaxial deformation studies for building structure-processing relationships are not enough by themselves hence multiaxial and biaxial deformation studies are necessary. It was shown that uniaxial and multiaxial (biaxial) deformations are quite different and require different approaches in order to understand the morphology evolution during deformation. Processes used in the polymer industry such as thermoforming and blow molding require more in-depth understanding so that polymers and polymer clay nanocomposites can go through predetermined processing routes and predetermined properties can be obtained.

Being the first in its kind, hopefully this work will open new windows in building structure-processing relationships of polymer/clay nanocomposites. There is still a big gap in this area of research. More work needs to be done on the high temperature studies under processing conditions. Although we have reached 55C, in order to obtain a complete understanding during processing, biaxial deformations at temperatures up to 150°C need to be studied. With our IBDD design, we aimed to reach these temperatures in-situ with x-rays. Unfortunately synchrotron radiation facilities are quite popular and obtaining beamtime is getting more competitive each year. This meant that we could not test IBDD and perform *in-situ* elevated temperature deformation studies requiring all our beamtime to complete the lower temperature experiments. In the future, this will be the purpose of the research where in-situ biaxial deformations coupled with x-rays will be performed at elevated temperatures so a better understanding of what is happening in the polymer morphology during real processing conditions are learned.

In order to design a nanocomposite for a specific end-use with required properties, it is important to understand the morphology both during and after processing. Observations of time dependent recovery on the morphology of PE and PENCs showed that what occurs during processing and what is obtained after may be different. In addition we also saw that the clays affected the morphology after recovery by increasing the required time for recovery. In the light of these observations, we believe there is more to discover to what happens after processing (or during time dependent recovery), in addition to what is happening during processing.

Polyolefins have been the focus of this research. However, polymer/clay nanocomposites are produced with variety of matrix polymers such as PET mainly for food packaging applications and nylon-6 mainly for automotive applications. In addition to polyolefins, clay nanocomposites of these commonly used polymers should also be studied and structure processing relationships should be established for these promising composites.

Additionally, shear induced morphology studies showed that the melt processing time has an important effect on the viscosity. The observations of shear thickening in PPNC5 and PPNC10 with increasing time under oscillatory shear shows that the processing route of high wt % clay added nanocomposites may require adjustments to the processing temperature. Such observations require more detailed understanding to make conclusions about the melt flow properties of PLS materials. As melt processing is a very powerful tool to make plastics, we believe this could be an area of further investigations.

APPENDIX A

MULTIAXIAL DEFORMATION DATA OF PE AND PP NANOCOMPOSITE SYSTEMS

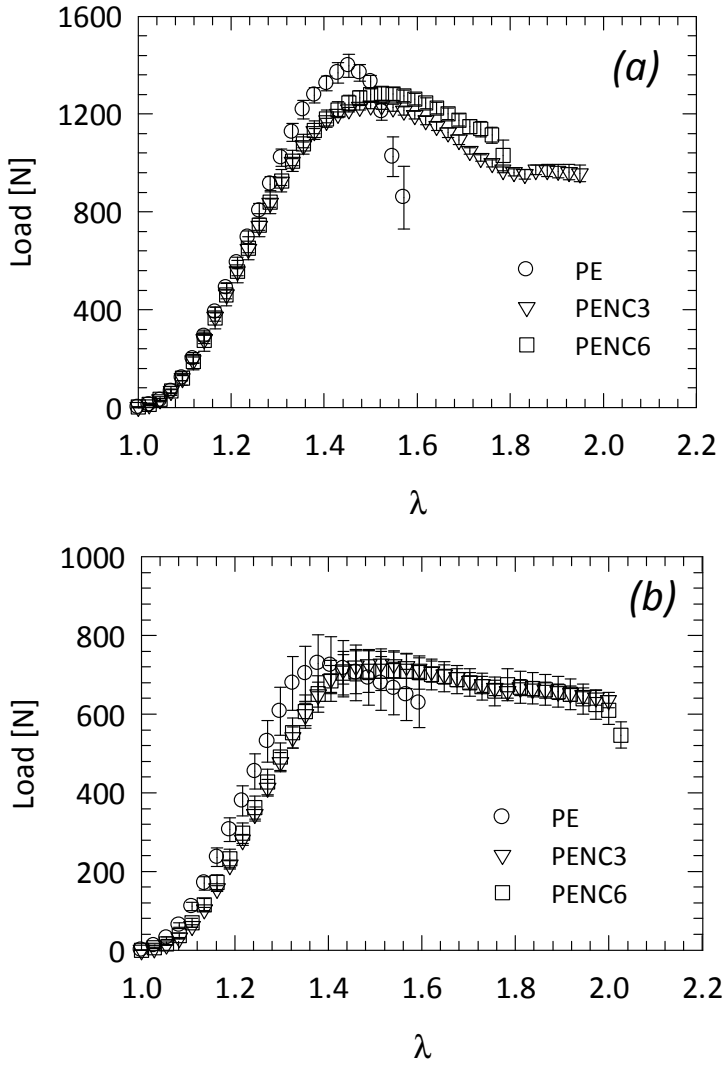

***Figure 74**. Multiaxial load vs. stretch ratio curves of PE and PENCs (a) at RT at 0.025s^{-1} and (b) at 55℃, 0.0025s^{-1}*

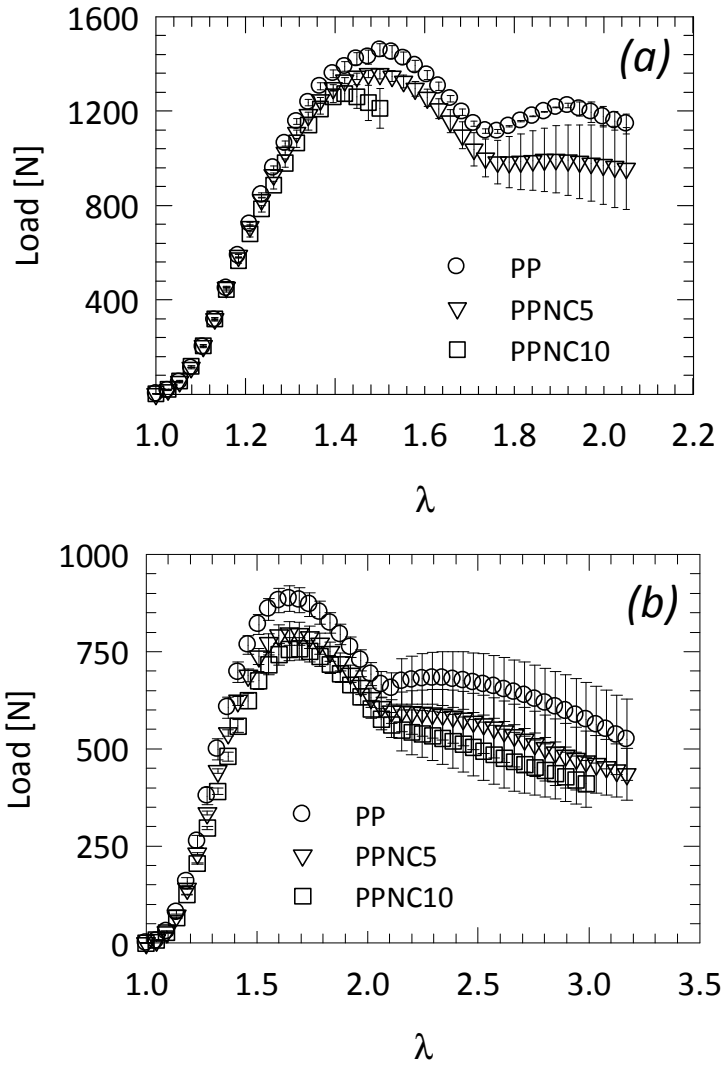

Figure 75. *Multiaxial load vs. stretch ratio curves of PP, PPNC5 and PPNC10 (a) at RT at 0.025s^{-1} and (b) at 55℃, 0.0025s^{-1}*

APPENDIX B

EX-SITU UNIAXIAL DEFORMATION BEHAVIOR OF PE AND PENCS

Small and wide angle scattering data was collected from PE and PENC6 after fully relaxation of samples following tensile deformation for comparison purposes between the multiaxial and uniaxial deformation behaviors (see Figure 76). Although the samples were fully relaxed, some of the aforementioned behavior under tensile strain can be seen from the 2D images such as the increasing anisotropy with increasing strain. As mentioned before SAXS images of the as made sample is anisotropic due to the sheet extrusion process however the applied strain was in the opposite direction and caused the loose of this anisotropy and growth of a new ordering in the strain direction. Since the samples were fully relaxed the formation and growth of monoclinic crystals are only indistinctly observed in the WAXS. The scattering patterns become more like fiber scattering with increasing strain. Morphology evolutions of both PE and PENC6 under uniaxial deformation were observed to be very similar except the improved toughness of the PE with the addition of clays as reported earlier.

Figure 77 shows 1D SAXS patterns of PE and PENC6 with respect to increasing strain. Some of the selected strain points are indicated in the figure. Since the scattering data was collected ex-situ, only a limited number of strain points were chosen and the scattering was collected from those samples. With increasing strain, for PE and PENC6, both of the peaks origination from sheet extrusion and chill roll processes were observed to shift towards lower q values which are similar with what was observed during

multiaxial deformation. However, since significantly higher strains were achieved during uniaxial deformation the shift in the q position at 0.024 nm^{-1} was exceeded the limits of the x-ray detector. The peak at q = 0.6 nm^{-1} was, on the other hand was observed to shift to q = 0.4 nm^{-1}, indicating an increase in the characteristic repeat distance of lamella from 10nm to 15 nm.

A slight difference between the neat polymer and the nanocomposite was the stretch point where the peaks were started to shift. This was happened earlier in the case of PENC6 where it was slightly delayed to a higher stretch ratio of around 2.35 in the case of PE. This delay suggests that the clay platelets actually support the re-organization of lamellae in the stretching direction hence they are shortening the required time whereas in the neat PE the required stretching is longer due to the lack of support from clays.

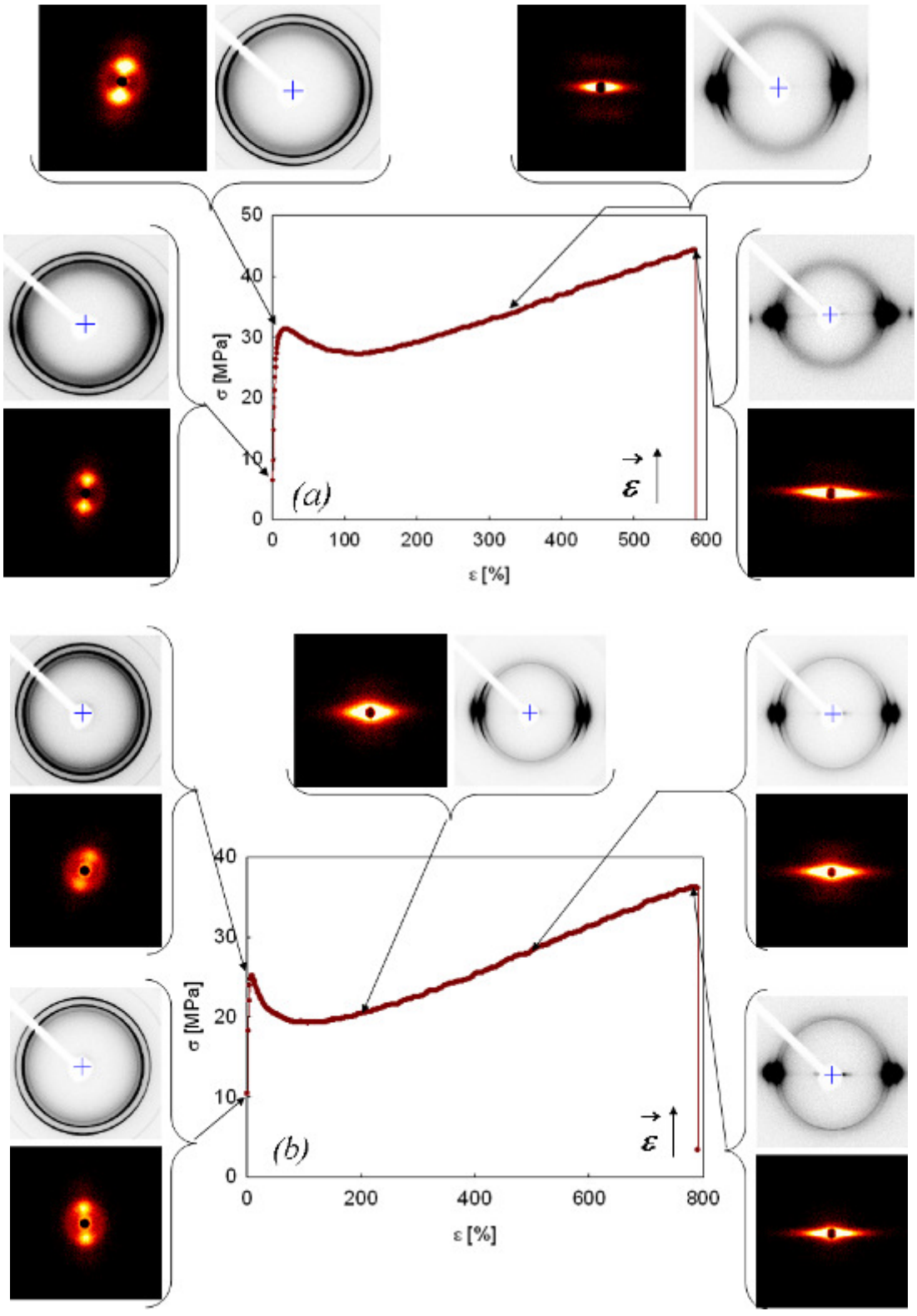

Figure 76. *2D WAXS and SAXS images of (a) PE and (b) PENC6 collected after uniaxial deformation*

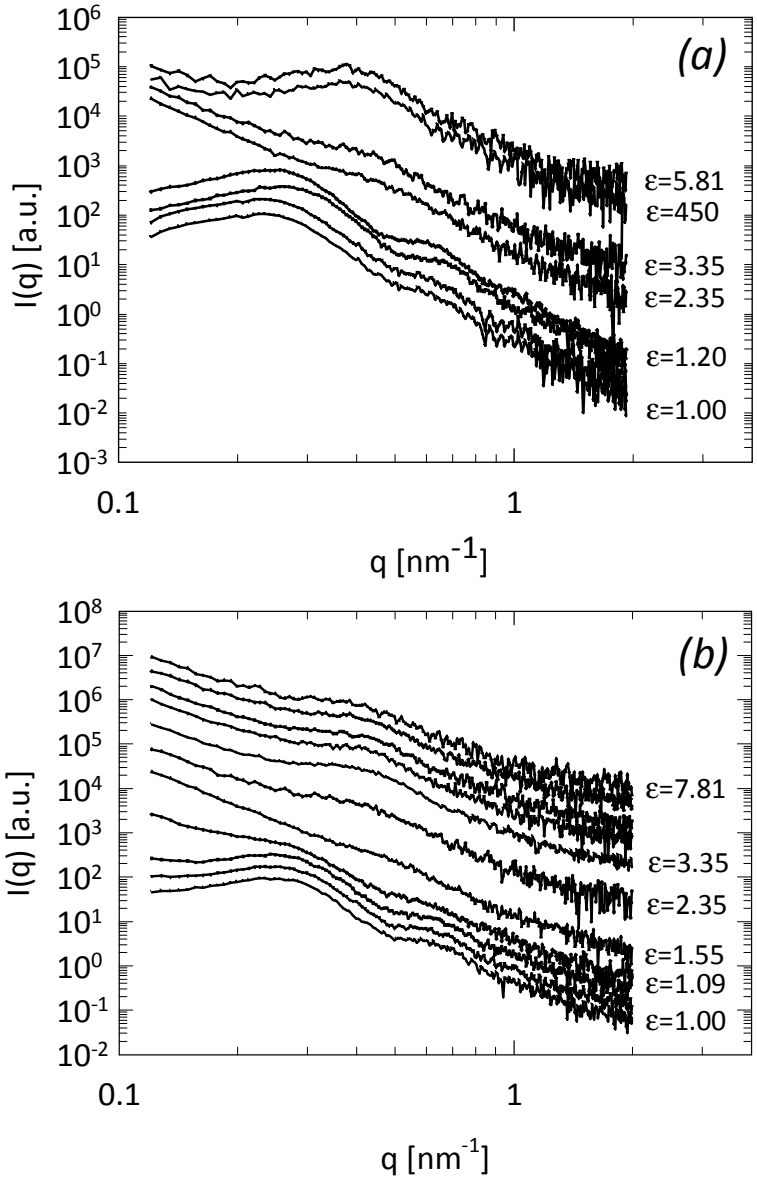

Figure 77. *1D SAXS plots from (a) PE and (b) PENC6 after uniaxial deformation, with increasing strain as indicated.*

From ex-situ 1D WAXS plots of PE and PENC, it is unlikely to monitor the formation and growth of monoclinic crystallites (see Figure 78). However the scattering from relaxed samples suggest that monoclinic crystals disappear fully in PE while in PENC6, even after complete relaxation, monoclinic crystals still exist in the PE morphology. This suggests that the clays prevent the transformation of the monoclinic

crystals back into orthorhombic form by creating a confined environment, similar to the relation in multiaxial deformation. Hence even after fully relaxation, there is a trace of monoclinic crystals exist in PE morphology due to clays.

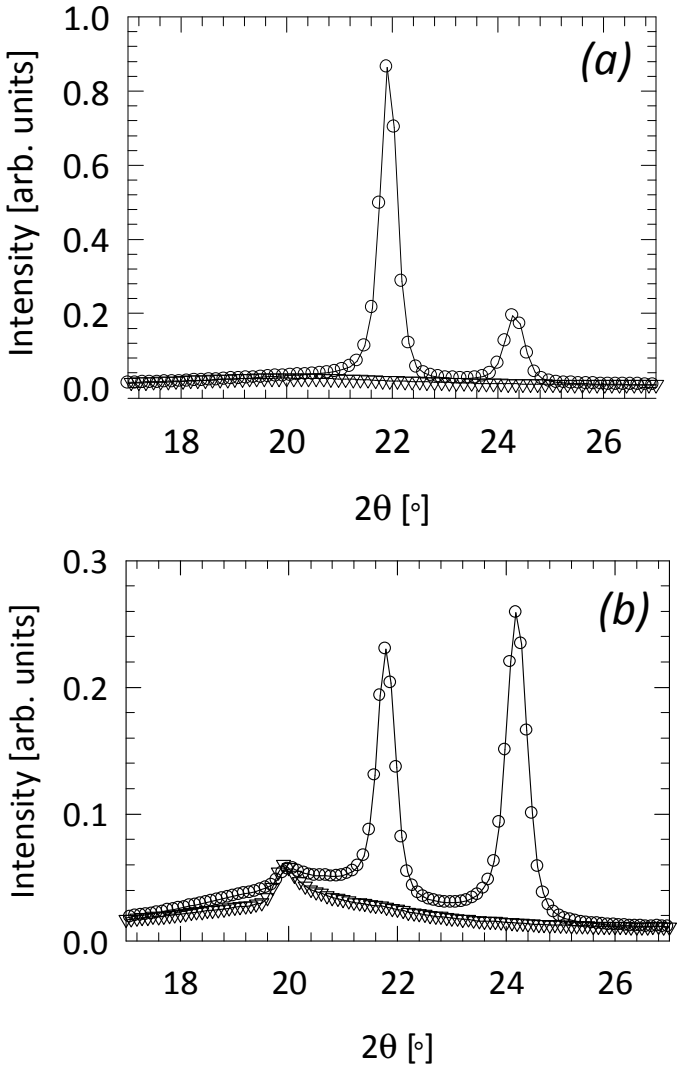

Figure 78. *1D cross sectional WAXS plots of (a) PE and (b) PENC6 in the strain direction before deformation (○) and after fracture(∇).*

APPENDIX C

SHEAR DEFORMATION AND WAXS STUDIES ON SHEARED PP AND PPNC SAMPLES

WAXS studies were performed on sheared PP and PPNCs to monitor the effect of shearing on the alignment/orientation of the PP crystallites as well as clays on the samples that were sheared for 30 min at 1Hz and 10Hz (see Figure 79). Before shearing, PP has shown isotropic scattering and PPNC5 and PPNC10 have shown slightly anisotropic scattering indicating clay platelet induced limited orientation in PP crystals. The rheological data show that, although the WAXS data are not significantly different, their rheological behavior is very different. In earlier works it was suggested that the principle difference in the microstructure of these materials is the state of dispersion of the clay tactoids in the matrix. The clay is expected to be well dispersed in the matrix [74]. In this case, however, it was observed that the orientation of the clays do not change significantly but they induce further orientation of (040)α and (113)α crystals of PP in the shear direction as can be seen from the anisotropic scattering patterns of PPNC5 and PPNC10 becoming more like two point pattern. The clays on the other hand were not observed to orient under shear flow as no change was detected in the clay peak.

As it was monitored from the higher viscosities reached at slower shear rate which was supported by the increase in the orientation of crystals seen from the 2D WAXS patterns. Rings patterns in WAXD images associated with (113)α and (13-1)α crystals became more like four point patterns indicating an higher degree of orientation

forming in PP. The rheological data indirectly suggest that the complex viscoelastic behavior is linked with deformation-induced micro-structural changes in the materials. The large aspect ratio of platelets promotes a supramolecular organization similar to other mesoscopic systems such as liquid crystalline polymers, surfactants or block copolymers [157].

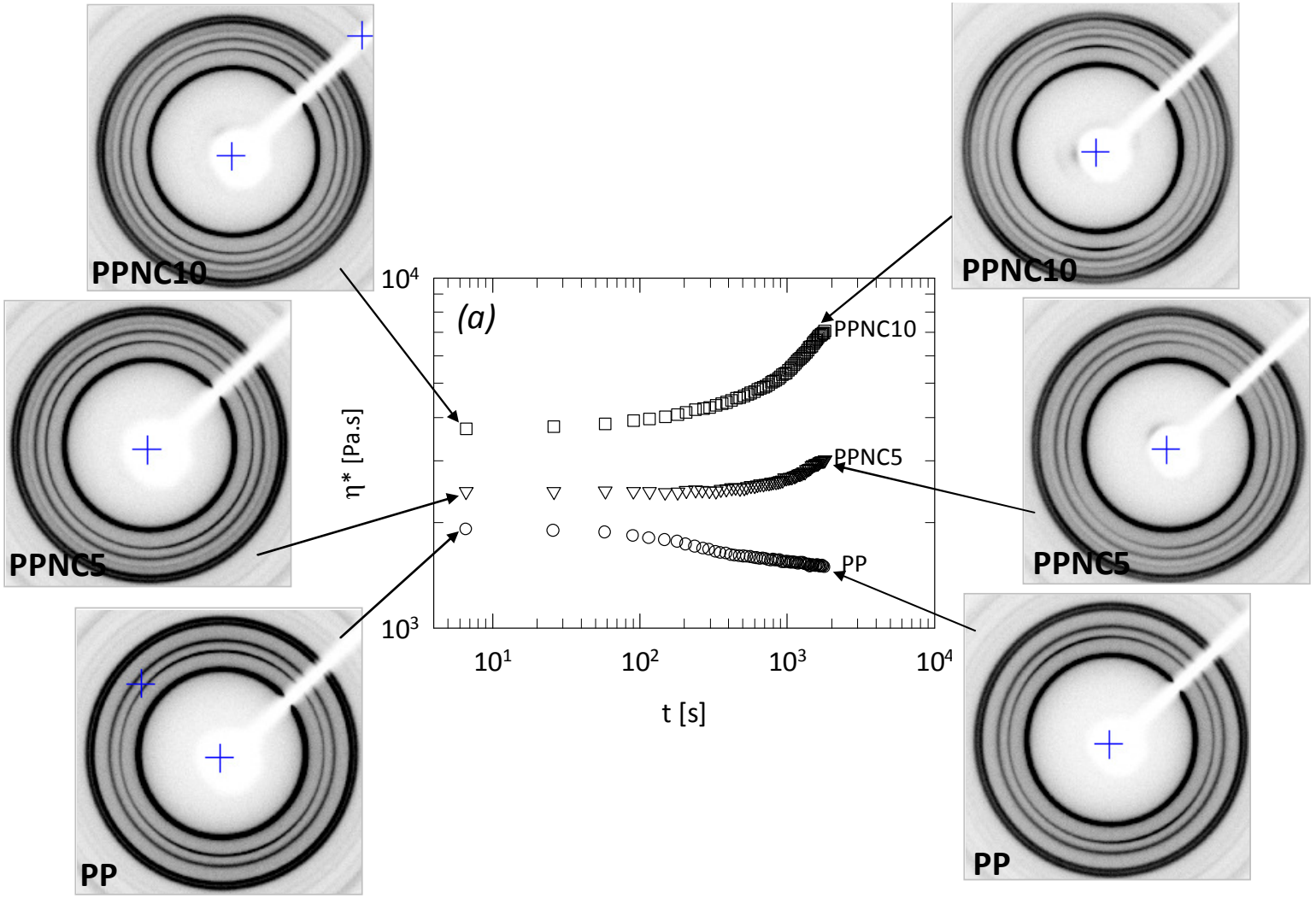

Figure 79. *2D WAXS images of PP and PPNCs before and after time sweep experiments combined with the time sweep data obtained at (a) 1Hz and (b) 10Hz.*

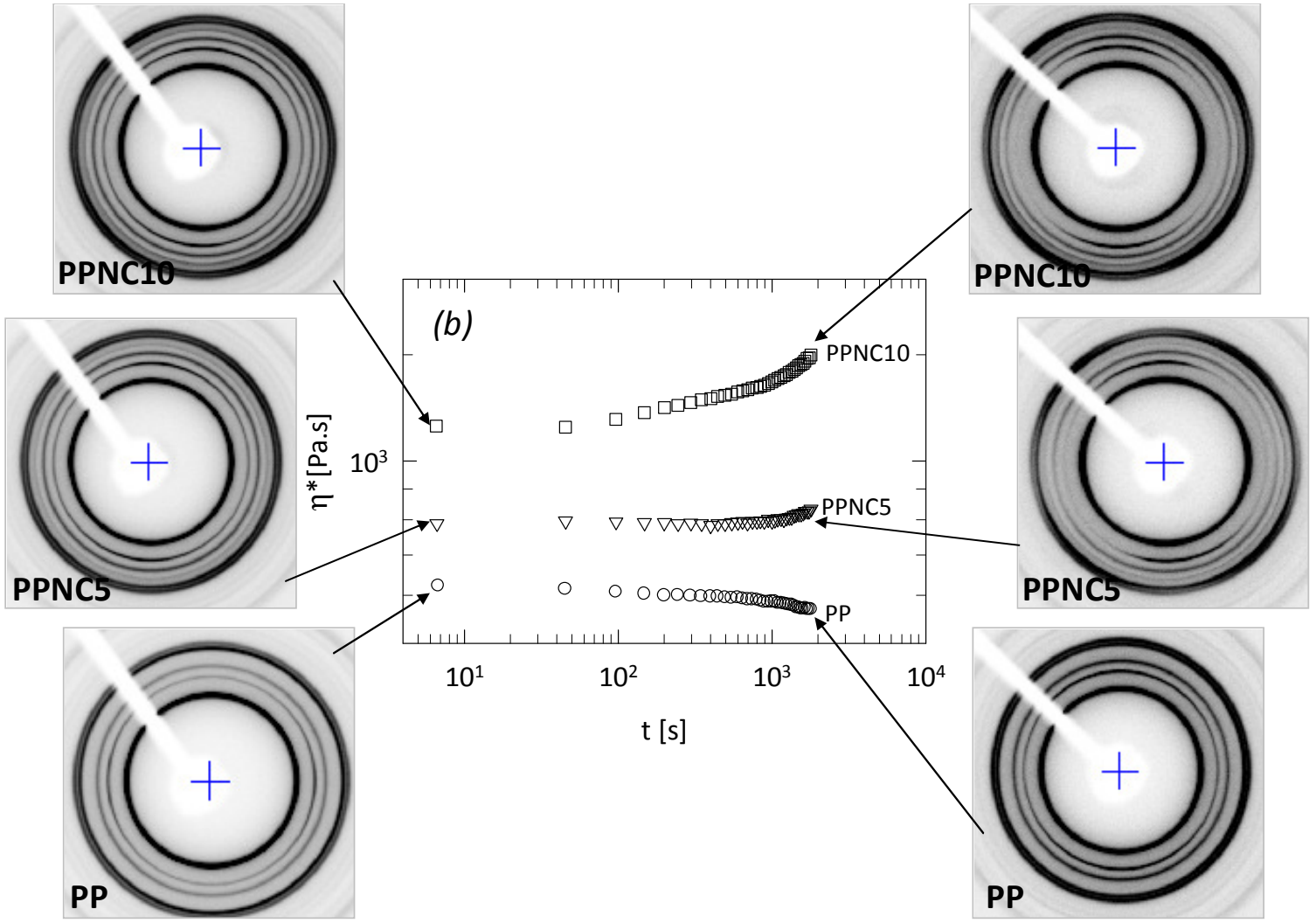

Figure 79 continued

APPENDIX D

PEAK FITTING ANALYSIS ON WAXS DATA

In Chapter V, area analysis under the crystal peaks were discussed to determine and to track the changes in the amount of monoclinic and orthorhombic crystals existing in PE during multiaxial deformation. Here we show examples and explain how the peak fitting analysis was performed to determine area under the peaks.

Peak fitting procedures typically need to consider removal of background such as diffraction of a continuous spectrum of wavelengths, diffraction scattering from materials other than the specimen including slits and sample mount and air; and diffuse scattering from the specimen itself. This background removal procedure for our experiments was performed at the synchrotron facilities that we used.

As explained in Chapter III, the film was stretched around an aluminum nose to create multiaxial deformation. Hence the scattering data that was collected *in-situ* also included the scattering from Al. Before the peak fitting analysis, in order to remove the effects of Al scattering, scattering from Al nose was collected and subtracted from the *in-situ* data.

Figure 80 and Figure 81 show the *in –situ* collected raw data of PE at stretch ratio of 1.00 and 1.38, respectively. In both Figure 80 (*a*) and Figure 81 (*a*), the scattering from the amorphous component of the polymer was obtained by fitting a Gaussian curve between a number of selected points. Later this amorphous scattering was removed from the total scattering and the scattering from only the crystallites of the polymer was

obtained. As seen from Figure 80 (*b*) and Figure 81 (*b*) the monoclinic and the orthorhombic crystal peaks are quite leveled with the zero line and quite distinguished from each other without any overlaps, which is a requirement for our peak fitting and area analysis. A Gaussian peak was fitted to each crystal peak and the area underneath the peaks was calculated using SigmaPlot software's in-built peak fitting and area analysis options. Equation 11 and 12 show the form of the fitted Gaussian curves to the crystal peaks and the formula for calculating the area underneath the peaks, respectively, where equation 12 uses the well-known trapezoid rule to calculate the area under the peak.

$$y = ae^{[-0.5(\frac{x-x_0}{b})^2]} \tag{11}$$

$$A = \int_a^b f(x)dx \approx \frac{1}{2}\sum_{i=2}^{N}(x_i - x_{i-1})(y_i + y_{i-1}) \tag{12}$$

where $y_i = f(x_i)$.

All these steps including Al background subtraction, amorphous background removal, as well as peak fitting and area analysis was performed at every step of the deformation and changes with respect to increasing multiaxial stretch ratio was tracked and reported accordingly in Chapter V.

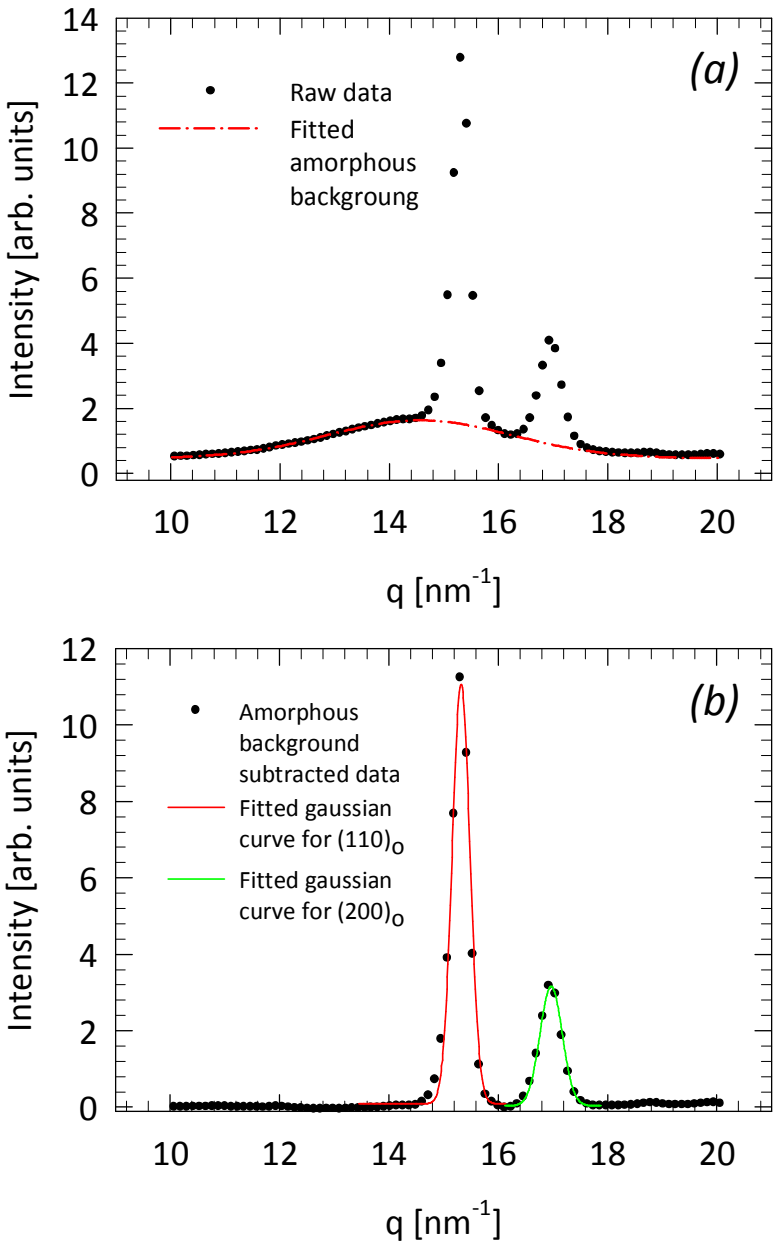

Figure 80. *Examples of curve fitting analysis for PE at λ=1.00 (a) for raw data and amorphous background, and (b) fitted Gaussian curves for crystal peaks*

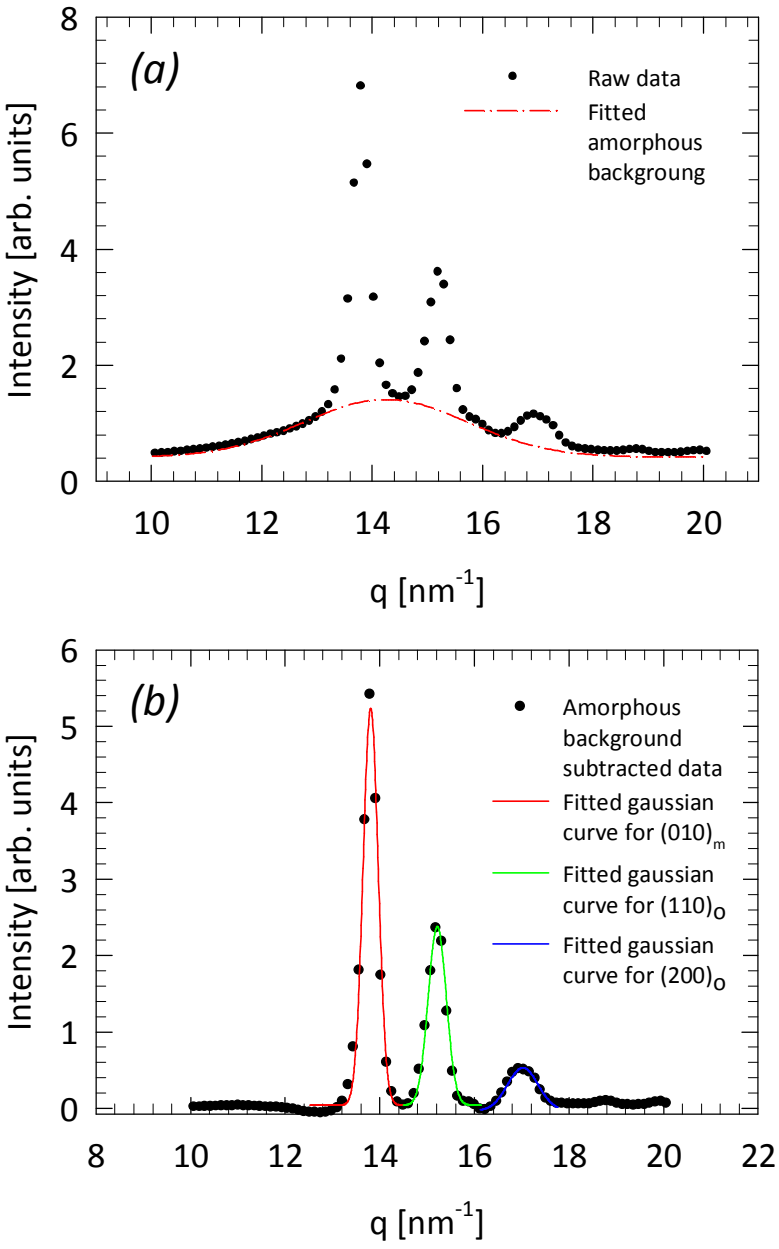

Figure 81. *Examples of curve fitting analysis for PE at λ=1.38 (a) for raw data and amorphous background; and (b) fitted Gaussian curves for crystal peaks*

REFERENCES

1. Kojima, Y., et al., *Mechanical properties of nylon 6-clay hybrid.* Journal of Materials Research(USA), 1993. **8**(5): p. 1185-1189.
2. Usuki, A., et al., *Synthesis of nylon 6-clay hybrid.* Journal of Materials Research(USA), 1993. **8**(5): p. 1179-1184.
3. Giannelis, E., *Polymer layered silicate nanocomposites.* Advanced Materials, 1996. **8**: p. 29-35.
4. Giannelis, E., R. Krishnamoorti, and E. Manias, *Polymer-silicate nanocomposites: model systems for confined polymers and polymer brushes.* Polymers in confined environments, 1999: p. 107-147.
5. *Polymer-clay nanocomposites.* Wiley series in polymer science, ed. T.J. Pinnavaia and G.W. Beall. 2000, Chichester, England: Wiley.
6. Biswas, M. and S. Ray, *Recent progress in synthesis and evaluation of polymer-montmorillonite nanocomposites.* Advances in Polymer Science, 2001. **155**: p. 167-222.
7. LeBaron, P., Z. Wang, and T. Pinnavaia, *Polymer-layered silicate nanocomposites: an overview.* Applied Clay Science, 1999. **15**(1-2): p. 11-29.
8. Ray, S. and M. Bousmina, *Biodegradable polymers and their layered silicate nanocomposites: in greening the 21st century materials world.* Progress in Materials Science, 2005. **50**(8): p. 962-1079.
9. Ray, S. and M. Okamoto, *Polymer/layered silicate nanocomposites: a review from preparation to processing.* Progress in Polymer Science, 2003. **28**(11): p. 1539-1641.
10. http://www.nanocor.com/
11. Butler, M., A. Donald, and A. Ryan, *Time resolved simultaneous small-and wide-angle X-ray scattering during polyethylene deformation. 2. Cold drawing of linear polyethylene.* Polymer, 1998. **39**(1): p. 39-52.
12. Butler, M., et al., *A real-time simultaneous small-and wide-angle X-ray scattering study of in-situ deformation of isotropic polyethylene.* Macromolecules, 1995. **28**(19): p. 6383-6393.
13. Elwell, M., S. Mortimer, and A. Ryan, *A Synchrotron SAXS Study of Structure Development Kinetics during the Reactive Processing of Flexible Polyurethane Foam.* Macromolecules, 1994. **27**(19): p. 5428-5439.
14. Elwell, M., et al., *In-situ studies of structure development during the reactive processing of model flexible polyurethane foam systems using FT-IR spectroscopy, synchrotron SAXS, and rheology.* Macromolecules, 1996. **29**(8): p. 2960-2968.
15. Butler, M. and A. Donald, *A real-time simultaneous small-and wide-angle X-ray scattering study of in situ polyethylene deformation at elevated temperatures.* Macromolecules, 1998. **31**(18): p. 6234-6249.
16. Davies, R., et al., *The use of synchrotron X-ray scattering coupled with in situ mechanical testing for studying deformation and structural change in isotactic polypropylene.* Colloid & Polymer Science, 2004. **282**(8): p. 854-866.

17. Butler, M., A. Donald, and A. Ryan, *Time resolved simultaneous small-and wide-angle X-ray scattering during polyethylene deformation 3. Compression of polyethylene.* Polymer-London, 1998. **39**: p. 781-792.
18. Zhang, X., M. Butler, and R. Cameron, *The ductile–brittle transition of irradiated isotactic polypropylene studied using simultaneous small angle X-ray scattering and tensile deformation.* Polymer, 2000. **41**(10): p. 3797-3807.
19. Vigny, M., et al., *Study of the molecular structure of PET films obtained by an inverse stretching process. Part I: Constant speed drawing of amorphous films.* Polymer Engineering & Science, 1997. **37**(11).
20. Mahendrasingam, A., et al., *Effect of draw ratio and temperature on the strain-induced crystallization of poly (ethylene terephthalate) at fast draw rates.* Polymer-London, 1999. **40**: p. 5553-5565.
21. Kawakami, D., et al., *Deformation-induced phase transition and superstructure formation in poly (ethylene terephthalate).* Macromolecules, 2005. **38**(1): p. 91-103.
22. Kawakami, D., et al., *Structural formation of amorphous poly (ethylene terephthalate) during uniaxial deformation above glass temperature.* Polymer, 2004. **45**(3): p. 905-918.
23. Kawakami, D., et al., *Superstructure evolution in poly (ethylene terephthalate) during uniaxial deformation above glass transition temperature.* Macromolecules, 2006. **39**(8): p. 2909-2920.
24. Kawakami, D., et al., *Mechanism of structural formation by uniaxial deformation in amorphous poly (ethylene terephthalate) above the glass temperature.* Macromolecules, 2003. **36**(25): p. 9275-9280.
25. Gurun, B., Y. Thio, and D. Bucknall, *Combined multiaxial deformation of polymers with in situ small angle and wide angle x-ray scattering techniques.* Review of Scientific Instruments, 2009. **80**: p. 123906.
26. [cited August 2010; Available from: www.energy.ca.gov/process/pubs/composites.pdf.
27. Gaier, J., et al., *The electrical and thermal conductivity of woven pristine and intercalated graphite fiber-polymer composites.* Carbon, 2003. **41**(12): p. 2187-2193.
28. Kim, J. and D. Reneker, *Mechanical properties of composites using ultrafine electrospun fibers.* Polymer composites, 1999. **20**(1): p. 124-131.
29. Liu, C. and C. Martin, *Composite membranes from photochemical synthesis of ultrathin polymer films.* 1991.
30. Singh, R., M. Zhang, and D. Chan, *Toughening of a brittle thermosetting polymer: effects of reinforcement particle size and volume fraction.* Journal of Materials Science, 2002. **37**(4): p. 781-788.
31. Yang, H., et al., *Rice-husk flour filled polypropylene composites; mechanical and morphological study.* Composite Structures, 2004. **63**(3-4): p. 305-312.
32. Kopeliovich, D. *Polymer Matrix Composites (introduction).* 2009 [cited 2010 August]; Available from: http://www.substech.com/dokuwiki/doku.php?id=polymer_matrix_composites_introduction.

33. Choudhury, N., A. Kannan, and N. Dutta, . *Novel nanocomposites and hybrids for lubricating coating applications.* Tribology and Interface Engineering Series, 2008. **55**: p. 501-542.
34. Koo, J., *Polymer nanocomposites: processing, characterization, and applications*. 2006: McGraw-Hill Professional.
35. Vaia, R., et al. *Polymer Nanocomposites with Prescribed Morphology: Going beyond Nanoparticle-Filled Polymers*. Proceedings of American Chemical Society Meeting 2007; Available from: http://zeus.plmsc.psu.edu/~manias/PDFs/POLY_inv2_mar07.pdf.
36. Vaia, R. and H. Wagner, *Framework for nanocomposites.* Materials Today, 2004. **7**(11): p. 32-37.
37. Harper, C., *Handbook of plastics technologies: the complete guide to properties and performance*. 2006: McGraw-Hill Professional.
38. Markarian, J., *Automotive and packaging offer growth opportunities for nanocomposites.* Plastics, Additives and Compounding, 2005. **7**(6): p. 18-21.
39. Zeng, Q., et al., *Clay-based polymer nanocomposites: research and commercial development.* Journal of nanoscience and nanotechnology, 2005. **5**(10): p. 1574-1592.
40. Meals, R. and F. Lewis, *Silicones (1959)*, Reinhold Publishing Corp., New York.
41. Shah, D., et al., *Dramatic enhancements in toughness of polyvinylidene fluoride nanocomposites via nanoclay-directed crystal structure and morphology.* Advanced Materials, 2004. **16**(14): p. 1173-1177.
42. Shah, D., et al., *Effect of nanoparticle mobility on toughness of polymer nanocomposites.* Advanced Materials, 2005. **17**(5): p. 525-528.
43. Krishnamoorti, R. and R. Vaia, eds. *Polymer Nanocomposites: Synthesis, Characterization, and Modeling* Journal of the American Chemical Society. Vol. 124. 2002, American Chemical Society: Washington, DC.
44. Gurmendi, U., J. Eguiazabal, and J. Nazabal, *Structure and Properties of Nanocomposites with a Poly (ethylene terephthalate) Matrix.* Macromolecular Materials and Engineering, 2007. **292**(2): p. 169-175.
45. Agag, T., T. Koga, and T. Takeichi, *Studies on thermal and mechanical properties of polyimide-clay nanocomposites.* Polymer, 2001. **42**(8): p. 3399-3408.
46. Lepoittevin, B., et al., *Poly (-caprolactone)/clay nanocomposites prepared by melt intercalation: mechanical, thermal and rheological properties.* Polymer, 2002. **43**(14): p. 4017-4023.
47. Kornmann, X., et al., *Nanocomposites based on montmorillonite and unsaturated polyester.* Polymer Engineering and Science, 1998. **38**(8): p. 1351-1358.
48. Shelley, J., P. Mather, and K. DeVries, *Reinforcement and environmental degradation of nylon-6/clay nanocomposites.* Polymer, 2001. **42**(13): p. 5849-5858.
49. Luo, J. and I. Daniel, *Characterization and modeling of mechanical behavior of polymer/clay nanocomposites.* Composites Science and Technology, 2003. **63**(11): p. 1607-1616.
50. Tsai, J. and C. Sun, *Effect of platelet dispersion on the load transfer efficiency in nanoclay composites.* Journal of Composite Materials, 2004. **38**(7): p. 567.

51. Cho, J. and D. Paul, *Nylon 6 nanocomposites by melt compounding.* Polymer, 2001. **42**(3): p. 1083-1094.
52. Meneghetti, P. and S. Qutubuddin, *Synthesis, thermal properties and applications of polymer-clay nanocomposites.* Thermochimica Acta, 2006. **442**(1-2): p. 74-77.
53. Hwu, J., et al., *The characterization of organic modified clay and clay-filled PMMA nanocomposite.* Journal of Applied Polymer Science, 2002. **83**(8): p. 1702-1710.
54. Fu, X. and S. Qutubuddin, *Polymer–clay nanocomposites: exfoliation of organophilic montmorillonite nanolayers in polystyrene.* Polymer, 2001. **42**(2): p. 807-813.
55. Rao, Y. and J. Pochan, *Mechanics of Polymer- Clay Nanocomposites.* Macromolecules, 2007. **40**(2): p. 290-296.
56. in *Committee on Technology, Subcommittee of Nanoscale Science, Engineering, and Technology* U.S.N.S.F.a.U.S.N.S.a.T. Council, Editor. 2000: Washington DC. p. 88.
57. Alexander, L., *X-ray diffraction methods in polymer science.* 1969.
58. Cullity, B. and S. Stock, *Elements of X-ray Diffraction. 2001.* Upper Saddle River, NJ.
59. Balta-Calleja, F. and C. Vonk, *X-ray scattering of synthetic polymers.* 1989.
60. Cebe, P., B. Hsiao, and D. Lohse, *Scattering from polymers: characterization by X-rays, neutrons, and light*. 2000: ACS Publications.
61. Xia, Z., et al., *Determination of crystalline lamellar thickness in poly(ethylene terepthalate) using small angle X-ray scattering and transmission electron microscopy* Journal of Macromolecular Science, Part B, 2001. **40**(5): p. 625-638.
62. Vonk, C., *Synthetic polymers in the solid state.* Small Angle X-ray Scattering, ed by Glatter O and Kratky O, Academic Press, London, UK. p, 1982. **433**.
63. Feigin, L. and D. Svergun, *Structure analysis by small-angle X-ray and neutron scattering*. 1987: Plenum Press New York.
64. Strobl, G. and M. Schneider, *Direct evaluation of the electron density correlation function of partially crystalline polymers.* Journal of Polymer Science: Polymer Physics Edition, 1980. **18**(6): p. 1343-1359.
65. Thompson, A., et al., *X-ray data booklet.* Lawrence Berkeley National Laboratory, 2001: p. 1–38.
66. Hendrix, J., *Advances in Polymer Science, ed. HH Kausch and HG Zachmann. Vol. 67. 1985*, Springer Verlag: Berlin.
67. Chu, B. and B. Hsiao, *Small-angle x-ray scattering of polymers.* Chem. Rev, 2001. **101**(6): p. 1727-1762.
68. Somani, R., et al., *Structure development during shear flow induced crystallization of i-PP: in situ wide-angle X-ray diffraction study.* Macromolecules, 2001. **34**(17): p. 5902-5909.
69. Cho, K., et al., *Real time in situ X-ray diffraction studies on the melting memory effect in the crystallization of [beta]-isotactic polypropylene.* Polymer, 2002. **43**(4): p. 1407-1416.
70. Androsch, R., *Melting and crystallization of poly (ethylene-co-octene) measured by modulated dsc and temperature-resolved X-ray diffraction.* Polymer, 1999. **40**(10): p. 2805-2812.

71. Androsch, R., et al., *Wide-and Small-Angle X-ray Analysis of Poly (ethylene-co-octene).* Macromolecules, 1999. **32**(11): p. 3735-3740.
72. Butler, M., A. Donald, and A. Ryan, *Time-Resolved Simultaneous Small-Angle and Wide-Angle X-Ray-Scattering During Polyethylene Deformation. 1. Cold Drawing of Ethylene-Alpha-Olefin Copolymers.* Polymer, 1997. **38**(22): p. 5521-5538.
73. Galgali, G., C. Ramesh, and A. Lele, *A rheological study on the kinetics of hybrid formation in polypropylene nanocomposites.* Macromolecules, 2001. **34**(4): p. 852-858.
74. Lele, A., et al., *In situ rheo-x-ray investigation of flow-induced orientation in layered silicate–syndiotactic polypropylene nanocomposite melt.* Journal of Rheology, 2002. **46**: p. 1091.
75. Chin, I., et al., *On exfoliation of montmorillonite in epoxy.* Polymer, 2001. **42**(13): p. 5947-5952.
76. Addiego, F., et al., *Characterization of volume strain at large deformation under uniaxial tension in high-density polyethylene.* Polymer, 2006. **47**(12): p. 4387-4399.
77. Tang, Y., et al., *Uniaxial deformation of overstretched polyethylene: In-situ synchrotron small angle X-ray scattering study.* Polymer, 2007. **48**(17): p. 5125-5132.
78. Hegemann, B., et al., *Biaxial deformation behavior of PET dependent on temperature and strain rate.* Journal of macromolecular science. Physics, 2002. **41**(4-6): p. 647-656.
79. Marco, Y., L. Chevalier, and M. Chaouche, *WAXD study of induced crystallization and orientation in poly (ethylene terephthalate) during biaxial elongation.* Polymer, 2002. **43**(24): p. 6569-6574.
80. Cakmak, M., et al., *Small angle and wide angle x-ray pole figure studies on simultaneous biaxially stretched poly (ethylene terephthalate)(PET) films.* Polymer Engineering and Science, 1987. **27**(12): p. 893-905.
81. Lüpke, T., et al., *Sequential biaxial drawing of polypropylene films.* Polymer, 2004. **45**(20): p. 6861-6872.
82. Butler, M. and A. Donald, *Real-time in situ light scattering and X-ray scattering studies of polyethylene blown film deformation.* Journal of Applied Polymer Science, 1998. **67**(2): p. 321-339.
83. Pawlak, A., *Cavitation during tensile deformation of high-density polyethylene.* Polymer, 2007. **48**(5): p. 1397-1409.
84. Schneider, K., et al. *The Study of Cavitation in HDPE Using Time Resolved Synchrotron X-ray Scattering During Tensile Deformation*. 2006: WILEY-VCH Verlag Weinheim.
85. Ren, C., et al., *Microstructure and Deformation Behavior of Polyethylene/Montmorillonite Nanocomposites with Strong Interfacial Interaction.* J. Phys. Chem. B, 2009. **113**(43): p. 14118-14127.
86. Wang, K., et al., *Deformation behavior of polyethylene/silicate nanocomposites as studied by real-time wide-angle X-ray scattering.* Macromolecules, 2002. **35**(14): p. 5529-5535.

87. Tzavalas, S. and V. Gregoriou, *Stress-Induced Crystal-to-Crystal Transformations in High-Density Polyethylene-Layered Silicate Nanocomposites: A Spectroscopic Study.* Applied spectroscopy, 2005. **59**(9): p. 1148-1154.
88. Stribeck, N., et al., *Tensile tests of polypropylene monitored by SAXS. Comparing the stretch-hold technique to the dynamic technique.* Journal of Polymer Science Part B: Polymer Physics, 2008. **46**(7): p. 721-726.
89. Machado, G., et al., *Crystalline properties and morphological changes in plastically deformed isotatic polypropylene evaluated by X-ray diffraction and transmission electron microscopy.* European Polymer Journal, 2005. **41**(1): p. 129-138.
90. Sakurai, T., et al., *Structural deformation behavior of isotactic polypropylene with different molecular characteristics during hot drawing process.* Polymer, 2005. **46**(20): p. 8846-8858.
91. Capt, L., et al. *Morphology Development during Biaxial Stretching of Polypropylene Films*. [cited 2010.
92. Galgali, G., S. Agarwal, and A. Lele, *Effect of clay orientation on the tensile modulus of polypropylene-nanoclay composites.* Polymer, 2004. **45**(17): p. 6059-6069.
93. Okamoto, M., et al., *A house of cards structure in polypropylene/clay nanocomposites under elongational flow.* Nano Letters, 2001. **1**(6): p. 295-298.
94. Doudard, C., et al., *Determination of an HCF criterion by thermal measurements under biaxial cyclic loading.* International Journal of Fatigue, 2007. **29**(4): p. 748-757.
95. Lecompte, D., et al., *Mixed numerical-experimental technique for orthotropic parameter identification using biaxial tensile tests on cruciform specimens.* International Journal of Solids and Structures, 2007. **44**(5): p. 1643-1656.
96. Chevalier, L. and Y. Marco, *Identification of a strain induced crystallisation model for PET under uni-and bi-axial loading: Influence of temperature dispersion.* Mechanics of Materials, 2007. **39**(6): p. 596-609.
97. Martin, P., et al., *Biaxial characterisation of materials for thermoforming and blow moulding.* Plastics, Rubber, and Composites, 2005. **34**(5-6): p. 276-282.
98. *Bi-axial Stress/Strain Measurement*. Available from: http://www.bhrgroup.com/bi-axial_stress-strain_measurement.aspx.
99. Jéol, S., et al., *Drastic modification of the dispersion state of submicron silica during biaxial deformation of poly (ethylene terephthalate).* Macromolecules, 2007. **40**(9): p. 3229-3237.
100. Jankauskaité, V., E. Strazdiené, and A. Laukaitiené, *Stress distribution in polymeric film laminated leather under biaxial loading.* Proc. Estonian Acad. Sci. Eng, 2006. **12**(2): p. 111-124.
101. Hubbell, J. and S. Seltzer. *Tables of X-Ray Mass Attenuation Coefficients and Mass Energy-Absorption Coefficients*. [cited 2006-2010; Available from: http://www.nist.gov/physlab/data/xraycoef/index.cfm.
102. *Compley Motions*. [cited 2006-2010; Available from: http://www.copleycontrols.com/Motion/Downloads/software.html.

103. Geiger, M., W. Hußnätter, and M. Merklein, *Specimen for a novel concept of the biaxial tension test.* Journal of Materials Processing Technology, 2005. **167**(2-3): p. 177-183.
104. Yu, Y., et al., *Design of a cruciform biaxial tensile specimen for limit strain analysis by FEM.* Journal of Materials Processing Technology, 2002. **123**(1): p. 67-70.
105. Demmerle, S. and J. Boehler, *Optimal design of biaxial tensile cruciform specimens.* Journal of the Mechanics and Physics of Solids, 1993. **41**(1): p. 143-181.
106. Makris, A., et al., *Shape optimisation of a biaxially loaded cruciform specimen.* Polymer Testing, 2009.
107. Brandrup, J. and E. Immergut, *Polymer Handbook, 3^ rd ed.* New York: A Wiley-Interscience Publication, 1989.
108. Wunderlich, B., *Macromolecular physics*. 1973: Academic Press.
109. *Advanced Photon Source, Beamline 5-ID-B,C,D: Sector 5 - ID Beamline DND-CAT, Materials Science, Polymer Science*. http://www.dnd.aps.anl.gov/ [cited 2010.
110. *Diamond Light Source, I22 - Non-crystalline diffraction*. http://www.diamond.ac.uk/Home/Beamlines/I22.html [cited 2010.
111. Hammersley, A. *FIT2D: An Introduction and Overview*. 1997 [cited 2010; Available from: http://www.esrf.eu/computing/scientific/FIT2D/FIT2D_INTRO/fit2d.html.
112. Zhao, C., et al., *Mechanical, thermal and flammability properties of polyethylene/clay nanocomposites.* Polymer Degradation and Stability, 2005. **87**(1): p. 183-189.
113. Gopakumar, T., et al., *Influence of clay exfoliation on the physical properties of montmorillonite/polyethylene composites.* Polymer, 2002. **43**(20): p. 5483-5491.
114. Zhang, M. and U. Sundararaj, *Thermal, Rheological, and Mechanical Behaviors of LLDPE/PEMA/Clay Nanocomposites: Effect of Interaction Between Polymer, Compatibilizer, and Nanofiller.* Macromolecular Materials and Engineering, 2006. **291**(6): p. 697-706.
115. Tanniru, M., et al., *The determining role of calcium carbonate on surface deformation during scratching of calcium carbonate-reinforced polyethylene composites.* Materials Science and Engineering: A, 2005. **404**(1-2): p. 208-220.
116. Araújo, E., et al., *Effects of organoclays on the thermal processing of pe/clay nanocomposites.* Journal of thermal analysis and calorimetry, 2007. **90**(3): p. 841-848.
117. Men, Y., et al., *Structural changes and chain radius of gyration in cold-drawn polyethylene after annealing: Small-and wide-angle X-ray scattering and small-angle neutron scattering studies.* J. Phys. Chem. B, 2005. **109**(35): p. 16650-16657.
118. *Softwares for Small-Angle Scattering.* http://www.small-angle.ac.uk/small-angle/Software/CORFUNC.html.
119. Hughes, D., et al., *A simultaneous SAXS/WAXS and stress-strain study of polyethylene deformation at high strain rates.* Polymer, 1997. **38**(26): p. 6427-6430.

120. Kiho, H., A. Peterlin, and P. Geil, *Polymer deformation. VI. Twinning and phase transformation of polyethylene single crystals as a function of stretching direction.* Journal of Applied Physics, 1964. **35**: p. 1599.
121. Takahashi, Y., T. Ishida, and M. Furusaka, *Monoclinic-to-orthorhombic transformation in polyethylene.* Journal of Polymer Science Part B: Polymer Physics, 1988. **26**(11): p. 2267-2277.
122. Tzavalas, S., K. Macchiarola, and V. Gregoriou, *High-density polyethylene layered silicate nanocomposites: Effect of mechanical stretching on the crystal-to-crystal transformations, morphology, and extent of exfoliation.* Journal of Polymer Science Part B: Polymer Physics, 2006. **44**(6): p. 914-924.
123. Kiho, H., A. Peterlin, and P. Geil, *Polymer deformation. IX. Deformation of polyethylene crystals at large strain.* Journal of Polymer Science Part B: Polymer Letters, 1965. **3**(4).
124. Seto, T., T. Hara, and K. Tanaka, *Phase transformation and deformation processes in oriented polyethylene.* Jap. J. Appl. Phys, 1968. **7**: p. 31.
125. Tanaka, K., T. Seto, and T. Hara, *Crystal Structure of A New Form of High-Density Polyethylene, Produced by Press.* Journal of the Physical Society of Japan, 1962. **17**(5): p. 873-874.
126. Bai, S., et al., *Polypropylene/polyamide 6/polyethylene-octene elastomer blends. Part 3. Mechanisms of volume dilatation during plastic deformation under uniaxial tension.* Polymer, 2005. **46**(17): p. 6437-6446.
127. G'Sell, C., S. Bai, and J. Hiver, *Polypropylene/polyamide 6/polyethylene-octene elastomer blends. Part 2: volume dilatation during plastic deformation under uniaxial tension.* Polymer, 2004. **45**(17): p. 5785-5792.
128. Yuan, Q. and R. Misra, *Impact fracture behavior of clay-reinforced polypropylene nanocomposites.* Polymer, 2006. **47**(12): p. 4421-4433.
129. Chen, L., et al., *Deformation mechanisms of nanoclay reinforced maleic anhydride modified polypropylene.* Journal of Polymer Science Part B: Polymer Physics, 2004. **42**(14): p. 2759-2768.
130. Kalaitzidou, K., H. Fukushima, and L. Drzal, *Mechanical properties and morphological characterization of exfoliated graphite-polypropylene nanocomposites.* Composites Part A: Applied Science and Manufacturing, 2007. **38**(7): p. 1675-1682.
131. Abu-Zurayk, R., et al., *Biaxial deformation behavior and mechanical properties of a polypropylene/clay nanocomposite.* Composites Science and Technology, 2009. **69**(10): p. 1644-1652.
132. Bhattacharyya, A., et al., *Crystallization and orientation studies in polypropylene/single wall carbon nanotube composite.* Polymer, 2003. **44**(8): p. 2373-2377.
133. Alexandre, M. and P. Dubois, *Polymer-layered silicate nanocomposites: preparation, properties and uses of a new class of materials.* Materials Science and Engineering: R: Reports, 2000. **28**(1-2): p. 1-63.
134. Dubnikova, I., et al., *Morphology, deformation behavior and thermomechanical properties of polypropylene/maleic anhydride grafted polypropylene/layered silicate nanocomposites.* Journal of Applied Polymer Science, 2007. **105**(6): p. 3836-3850.

135. Vleeshouwers, S., *Simultaneous in-situ WAXS/SAXS and dsc study of the recrystallization and melting behaviour of the [alpha] and [beta] form of iPP.* Polymer, 1997. **38**(13): p. 3213-3221.
136. Pawlak, A. and A. Galeski, *Cavitation during tensile deformation of polypropylene.* Macromolecules, 2008. **41**(8): p. 2839-2851.
137. Li, Y., G. Wei, and H. Sue, *Morphology and toughening mechanisms in clay-modified styrene-butadiene-styrene rubber-toughened polypropylene.* Journal of Materials Science, 2002. **37**(12): p. 2447-2459.
138. Gurun, B., et al., *Multiaxial deformation of polyethylene and polyethylene/clay nanocomposites: In-situ synchrotron small angle and wide angle X-ray scattering study.* submitted to "Composites Science and Technology", 2010.
139. Albrecht, T. and G. Strobl, *Temperature-Dependent Crystalline-Amorphous Structures in Isotactic Polypropylene: Small-Angle X-ray Scattering Analysis of Edge-Bounded Two-Phase Systems.* Macromolecules, 1995. **28**(15): p. 5267-5273.
140. Kumaraswamy, G., et al., *Shear-enhanced crystallization in isotactic polypropylene. in-situ synchrotron SAXS and WAXD.* Macromolecules, 2004. **37**(24): p. 9005-9017.
141. Liu, L., et al., *Structure Changes during Uniaxial Deformation of Ethylene-Based Semicrystalline Ethylene- Propylene Copolymer. 1. SAXS Study.* Macromolecules, 2003. **36**(6): p. 1920-1929.
142. Lezak, E., Z. Bartczak, and A. Galeski, *Plastic deformation behavior of [beta]-phase isotactic polypropylene in plane-strain compression at room temperature.* Polymer, 2006. **47**(26): p. 8562-8574.
143. Lezak, E., Z. Bartczak, and A. Galeski, *Plastic Deformation of the Phase in Isotactic Polypropylene in Plane-Strain Compression.* Macromolecules, 2006. **39**(14): p. 4811-4819.
144. Xu, B., et al., *Evolution of Clay Morphology in Polypropylene/Montmorillonite Nanocomposites upon Equibiaxial Stretching: A Solid-State NMR and TEM Approach.* Macromolecules, 2009. **42**(22): p. 8959-8968.
145. Bartczak, Z. and E. Martuscelli, *Orientation and properties of sequentially drawn films of an isotactic polypropylene/hydrogenated oligocyclopentadiene blend.* Polymer, 1997. **38**(16): p. 4139-4149.
146. Solomon, M., et al., *Rheology of polypropylene/clay hybrid materials.* Macromolecules, 2001. **34**(6): p. 1864-1872.
147. Mishra, J., K. Hwang, and C. Ha, *Preparation, mechanical and rheological properties of a thermoplastic polyolefin (TPO)/organoclay nanocomposite with reference to the effect of maleic anhydride modified polypropylene as a compatibilizer.* Polymer, 2005. **46**(6): p. 1995-2002.
148. Gu, S., J. Ren, and Q. Wang, *Rheology of poly (propylene)/clay nanocomposites.* Journal of Applied Polymer Science, 2004. **91**(4): p. 2427-2434.
149. Wagener, R. and T. Reisinger, *A rheological method to compare the degree of exfoliation of nanocomposites.* Polymer, 2003. **44**(24): p. 7513-7518.
150. Durmus, A., A. Kasgoz, and C. Macosko, *Linear low density polyethylene (LLDPE)/clay nanocomposites. Part I: Structural characterization and*

quantifying clay dispersion by melt rheology. Polymer, 2007. **48**(15): p. 4492-4502.
151. Chen, P., J. Zhang, and J. He, *Increased flow property of polycarbonate by adding hollow glass beads.* Polymer Engineering and Science, 2005. **45**(8): p. 1119-1131.
152. Treece, M. and J. Oberhauser, *Soft Glassy Dynamics in Polypropylene- Clay Nanocomposites.* Macromolecules, 2007. **40**(3): p. 571-582.
153. Ren, J., A. Silva, and R. Krishnamoorti, *Linear Viscoelasticity of Disordered Polystyrene- Polyisoprene Block Copolymer Based Layered-Silicate Nanocomposites.* Macromolecules, 2000. **33**(10): p. 3739-3746.
154. Krishnamoorti, R. and E. Giannelis, *Rheology of end-tethered polymer layered silicate nanocomposites.* Macromolecules, 1997. **30**(14): p. 4097-4102.
155. Sanchez-Solis, A., A. Garcia-Rejon, and O. Manero. *Production of nanocomposites of PET-montmorillonite clay by an extrusion process*. 2003: John Wiley & Sons.
156. McKinley, G. and G. Bettin, *Energy absorption of reticulated foams filled with shear-thickening silica suspensions.* 2005.
157. Schmidt, G., et al., *Shear Orientation of Viscoelastic Polymer- Clay Solutions Probed by Flow Birefringence and SANS.* Macromolecules, 2000. **33**(20): p. 7219-7222.